

The development of a directional gas injection  
system for the H-1NF heliac

A thesis submitted for the degree  
of Doctor of Philosophy of  
the Australian National University

Scott Matthew Collis

October 4, 2007



This thesis contains no material which has been accepted for the award of any other degree or diploma in any university. To the best of the author's knowledge and belief, it contains no material previously published or written by another person, except where due reference is made in the text.

A handwritten signature in black ink, appearing to read 'Collis', with a stylized, cursive script.

Scott Matthew Collis  
October 4, 2007



I dedicate this work to my daughter Isabelle

In the hope of clean, abundant and politically viable energy in your  
lifetime



# Acknowledgements

Throughout this thesis I have had the help and support of many people. First and foremost I would like to thank my supervisor A/Prof John Howard. John has done more than just advise and help me throughout my PhD; he has allowed me to develop as a scientist by allowing me the space to find the way rather than just being shown it. I would also like to thank A/Prof Boyd Blackwell, the head of the H-1 national facility. Boyd's encyclopedic knowledge of plasma physics and physics in general has proved indispensable over the years. I would like to thank Prof Jeff Harris, the former head of the department for his advice and support. I would also like to thank Dr Horst Punzmann who has acted as a sounding board for ideas and for being a true friend.

I would like to thank and acknowledge Dr Daniel Andruczyk and Prof Brian James who developed the diagnostic helium beam. For their tireless work and assistance I would like to thank all the members of the school electronics unit in particular David Anderson, David Kelly, Michael Blacksell, Steven Huynh (sorry about those amps!), Wasantha Ramasundara, Dennis Gibson and their fearless leader Tony Cullen. Thanks are due to all the staff of the mechanical workshop and in particular Miro Peric for his sensational work on the nozzle inserts. The technical staff of the plasma research lab have been essential to the work presented in this thesis so I would like to thank Con Costa, Ray Kimlin, Clint Davies, Peter Alexander, Herb Zeilinger, John Wach (who has had a hand in most of the CAD pictures presented here) and the newest member of the team Mark Gwenneth (I don't know what we did without you!).

To my fellow students I express my gratitude for your support, advice and friendship. I would like to thank David Oliver for allowing me to use the inversions from the ELSI device and for "chewing the fat" over PhD issues. I am very happy to see Ben Powell's expansion on the work submitted in this thesis as well as his unique and refreshing take on fusion research. I would like to thank Fenton Glass and Dave

Pretty for introducing me to Linux and for answering all my newbie questions on the world's greatest operating system. And I would like to thank Santhosh, Dave Byrne (too many Daves!), Clive, Hua, Andrew and Wayne for their friendship and support throughout the years.

I would like to acknowledge the support of my family. My siblings (and sibling in law) Ben, Kelly and Rob. And my parents John and Marilyn Collis who have been an endless source of support and inspiration. Last, but by no means least I thank my wife, Louise Collis. I may have just submitted a PhD thesis but I still think marrying you was the cleverest thing I have ever done.

# Publications

- Harris JH, Shats MG, Blackwell BD, Solomon WM, Pretty DG, Collis SM, Howard J, Xia H, Michael CA, Punzmann H. Fluctuations and stability of plasmas in the H-1NF heliac.,  
*Nuclear Fusion*, **44**(2), pages 279-86 (2004)
- Blackwell BD, Harris JH, Howard J, Shats MG, Charles C, Collis SM, Gardner HJ, Glass FJ, Hua X, Michael CA, Pretty DG, Punzmann H, Solomon WM, Borg GG. Overview and results from the H-1 National Facility.  
*American Institute of Physics Conference Proceedings*, (669), pages 151-61 (2003)
- Collis SM, Howard J, Warr GB, Michael CA, Harris JH, Blackwell BD, Pretty DG. Studies of resonantly produced plasmas in the H-1NF heliac using a far infrared scanning interferometer.  
*Review of Scientific Instruments*, **74**(3), pages 1629-32 (2003)
- Collis SM, Howard J, Blackwell BD, Powell B, Carlsson P, Abelson M. a Supersonic gas injection system for fuelling and probing fusion plasmas  
*Plasma sources sci. technol.*, **15**, pages 797-804 (2006)

# Statement of author's original work

I have had some level of involvement in all work that is reported in this thesis. As with any large experiment I have had a lot of assistance. Being new to the field of plasma physics on commencement of my PhD I have had extensive guidance from my supervisor A/Prof John Howard and the head of the H-1 national facility A/Prof Boyd Blackwell, all sections of this thesis have benefited in some way from their advice. I therefore draw attention to specific sections where the material presented was substantially or entirely my own original work:

- Section 2.4: Performing the study of the effect of magnetic configuration on plasma formation at 0.5 tesla.
- Section 2.5: Investigating the effect of the position of the ion cyclotron resonant layer on plasma formation.
- Section 2.6: Discussion of the fuelling issues associated with a resonantly heated plasma in a static fill.
- Section 3.2: The installation and calibration of the imaging system for the HLR  $T_e$  diagnostic.
- Section 3.3.1: The characterisation of the HBD for multi pulse use.
- Section 3.4: Development of the procedure to extract the helium emissivities from the raw data and calculate the  $T_e$  profile.
- Chapter 4: With the exception of the tomographic inversions of the ELSI data.
- Chapter 5 Directional gas injection system development.

# Abstract

This thesis discusses the development of a directional gas injection system for the H-1NF heliac. The H-1NF heliac [Hamberger et al., 1990] is a three period helical axis stellarator (major radius 1m, minor radius 0.15-0.2m) built with the majority of the magnetic coil set inside the ( $33\text{m}^3$ ) vacuum vessel. This contrasts with most other fusion research devices where the vacuum vessel conforms to the plasma surface, with the magnetic coil set outside. This design leads to a larger volume of the H-1NF vessel relative to the ( $1\text{m}^3$ ) plasma.

Interferometric studies of the evolution of the density profile under combined electron and ion resonant heating lead us to believe that the large gas reservoir surrounding the H-1NF plasma will lead to difficulties in achieving the density control required to maximise the plasma temperature. To remedy the situation a project to build a directional gas injection system that fuels the plasma region while minimising the flux to the background component was initiated.

Initially the electron temperature profile of the H-1NF plasma was not very well known. As part of a collaboration with the University of Sydney we installed a helium beam based line ratio electron temperature diagnostic. This diagnostic has obtained the first spatially and temporally resolved spectroscopic measurements of electron temperature on the H-1NF heliac.

Using the diagnostic and plasma density interferometry we were able to determine the plasma pressure, stored energy and estimate the electron energy confinement time for an electron cyclotron resonantly heated plasma. Using a time dependent collisional radiative model we calculated the density of the excited states of the diagnostic helium beam. A comparison between the calculated emissivities and the emissivities measured using the viewing optics for the helium line ratio diagnostic show good agreement, which gives us good confidence in the model.

With a knowledge of the electron temperature and density profile we designed and tested an alternative fuelling system which uses a double conical nozzle to gener-

ate a directed flow of particles into the plasma without adding to the gas inventory in the rest of the vacuum vessel. By using a closed plenum at a programmable pressure and a piezo-electric valve, the particle flux can be dynamically changed in a controlled and quantitative manner. Measurements of the gas jet using constant temperature hot wire anemometry show that, for plenum pressures between 500 and 1000 torr, the particle injection rate (helium) ranges between  $2 \times 10^{20}$  and  $4 \times 10^{20} \text{ s}^{-1}$  with half cone angles between 5 and 20 degrees. The system has been installed on the H-1NF device and first plasma results indicate localised gas injection consistent with test tank anemometry measurements.

Further simulations of the beam plasma interaction using the time dependent collisional radiative model shows that the majority of the neutrals in the beam will be ionised by the plasma. However, a calculation of the power lost from inelastic collisions between the beam and the plasma electrons (electron impact ionisation and excitation) shows that the beam will have a significant perturbation on the plasma stored energy and a nozzle designed for lower flux would provide more controlled fuelling.

# Contents

<b>Acknowledgements</b>	<b>i</b>
<b>Publications</b>	<b>iii</b>
<b>Abstract</b>	<b>v</b>
<b>1 Introduction</b>	<b>2</b>
1.1 Fusion as a source of energy . . . . .	2
1.2 The plasma state and plasma confinement . . . . .	4
1.2.1 Magnetic confinement configurations . . . . .	6
1.3 The H-1NF heliac . . . . .	7
1.3.1 Vessel and fuelling . . . . .	9
1.3.2 Plasma heating systems . . . . .	10
1.4 Plasma diagnostics and data storage . . . . .	10
1.5 ITER . . . . .	11
1.6 Thesis overview . . . . .	12
<b>2 Interferometric studies of hydrogen ion resonant plasma formation</b>	<b>15</b>
2.1 Density Interferometry . . . . .	16
2.1.1 The far infra-red scanning interferometer . . . . .	17
2.1.2 The electronically scanned interferometer . . . . .	21
2.2 Inverse techniques . . . . .	22
2.3 Experimental conditions at 0.5 Tesla . . . . .	24
2.3.1 Ion cyclotron resonant heating . . . . .	25
2.3.2 Electron cyclotron resonant heating . . . . .	26
2.4 The effect of magnetic configuration on plasma formation . . . . .	27
2.5 The effect of the position of the $\omega = \omega_{ci}$ layer on plasma formation .	28
2.6 Initial study of plasma formation under combined electron and ion resonant heating . . . . .	30

<b>3</b>	<b>Helium line ratios for electron temperature measurements</b>	<b>33</b>
3.1	The collisional radiative model . . . . .	34
3.2	Optical system . . . . .	36
3.2.1	Optical calibration . . . . .	39
3.3	Helium beam diagnostic . . . . .	43
3.3.1	Beam characterisation for multi-pulse use . . . . .	46
3.4	Calculation of $T_e$ . . . . .	51
3.4.1	Uncertainties . . . . .	52
3.4.2	A sample result: Electron resonantly heated He + H plasma . . . . .	55
<b>4</b>	<b>Studies of resonantly heated plasmas using the HLR diagnostic</b>	<b>57</b>
4.1	Experimental condition for ECH plasmas . . . . .	57
4.2	Plasma evolution of discharge 61031 . . . . .	58
4.3	Transformation to flux co-ordinates and symmetry . . . . .	62
4.4	Temperature profile as a function of helical ratio . . . . .	64
4.5	Ion electron temperature equilibration . . . . .	65
4.6	Beam propagation study using the time dependent collisional radiative model . . . . .	67
4.7	$T_e$ profile for a ion cyclotron heated plasma . . . . .	69
<b>5</b>	<b>The Directional Injection System for H-1NF</b>	<b>74</b>
5.1	Review of current fuelling systems . . . . .	74
5.2	Theory . . . . .	75
5.3	Test tank measurements . . . . .	79
5.3.1	Gas flux measurements . . . . .	79
5.3.2	Particle injection rate calibration . . . . .	82
5.3.3	Profile measurements . . . . .	83
5.3.4	Velocity measurements . . . . .	84
5.4	Interaction with the plasma . . . . .	86
5.5	Installation and operation on the H-1NF heliac . . . . .	88
5.6	Predicted fuelling using a time dependent CRM . . . . .	91
5.6.1	Slab model . . . . .	91
5.6.2	Model using experimentally determined $T_e$ and $n_e$ profiles . . . . .	94
<b>6</b>	<b>Conclusions</b>	<b>100</b>
6.1	Outcomes . . . . .	100
6.2	Future Work . . . . .	102
6.2.1	Helium metastable populations and LIF E-field measurements . . . . .	102

<b>A</b>	<b>Coherence imaging of helium ion temperatures</b>	<b>105</b>
A.1	Coherence imaging . . . . .	106
A.2	Doppler imaging diagnostic . . . . .	108
A.3	Calibration . . . . .	110
<b>B</b>	<b>Wave propagation through a homogeneous medium</b>	<b>112</b>
<b>C</b>	<b>Photographs of equipment and layouts</b>	<b>114</b>
<b>D</b>	<b>Table of acronyms</b>	<b>119</b>
<b>E</b>	<b>Table of symbols</b>	<b>120</b>
	List of figures	122
	Bibliography	130

# Introduction

Far away there in the distance are my highest aspirations. I may not reach them, but I can look up and see their beauty, believe in them, and try to follow where they lead

– *Louisa May Alcott*

This thesis describes the process that led to, as well as the development and testing of a directional gas injection system to provide a fuelling source for the H-1NF heliac. The fuelling of magnetically confined plasmas is an area of active research with many systems being considered for the large ITER experiment and future magnetic fusion power plants. Fuelling in the H-1NF heliac is complicated by two design considerations. The H-1NF plasma, which has a volume of  $1\text{m}^3$ , sits inside a vacuum vessel with a volume of over  $30\text{m}^3$ . As will be discussed at the end of chapter 2 this leads to problems controlling the plasma density. Also, as a direct consequence of the flexibility of the H-1NF device, the plasma has a variable shape so any fuelling device must be a certain minimum distance from plasma edge.

This chapter begins by placing the work presented in this thesis into the context of the search for a clean, economical and accessible source of energy: fusion power. The basic physics behind magnetically confined plasmas will then be presented as well as an overview of the facility where the experiments presented in this thesis were carried out: the H-1NF heliac. The chapter will then conclude with an outline of the thesis.

## 1.1 Fusion as a source of energy

Since the industrial revolution levels of carbon dioxide ( $\text{CO}_2$ ) in our atmosphere have been increasing. Figure 1.1 shows the concentration of atmospheric  $\text{CO}_2$  measured at the Mauna Loa atmospheric observatory [NOAA, 2006] in the Pacific. The figure shows a clear increase in levels over the time of the study (1950 to 2003).

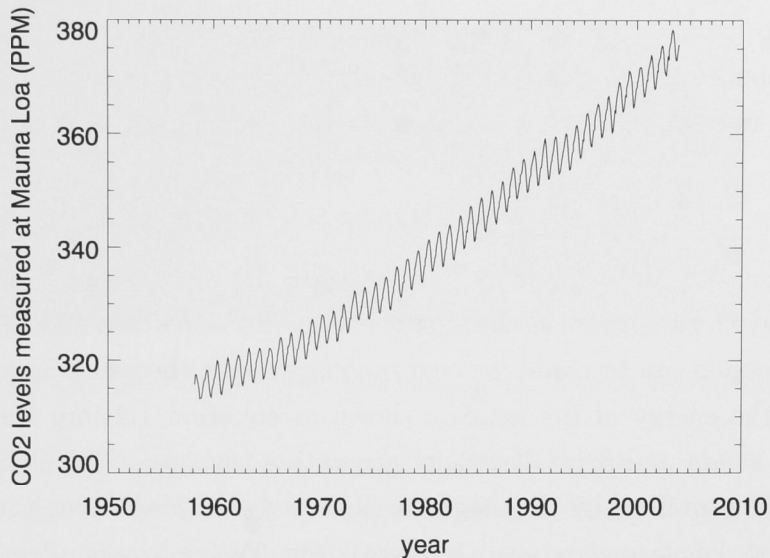


Figure 1.1: CO<sub>2</sub> Levels from the Mauna Loa clean air observatory in the pacific

This clear increase of CO<sub>2</sub> concentration can be linked to the process of burning fossil fuels. An example of hydrocarbon combustion is the (idealised) combustion of methane, shown in equation 1.1



and a very similar process occurs when coal is burnt to produce electricity. Carbon dioxide has the ability to reflect infra-red radiation back towards the earth's surface, in effect trapping energy under the atmosphere and increasing global temperatures (this is known as the greenhouse effect), so it is not environmentally sustainable to continue to rely on the combustion of fossil fuels for base load electricity generation. To slow (or halt) the increase of CO<sub>2</sub> levels in the atmosphere while maintaining quality of living and an expanding global economy, an effective non-CO<sub>2</sub> emitting source of electricity generation must be developed. While nuclear fission (harnessing the energy produced from a mass deficit when heavy atomic isotopes divide) can produce non-CO<sub>2</sub> emitting power, some of the products of the fission reaction are very long-lived strongly radioactive. If not properly stored this nuclear waste can have a devastating health impact upon biological systems, including humans. And, due to a small number of accidents (for example Chernobyl), fission-powered electricity generation has a very poor public image in many countries and popular media is not helping the situation.

An alternative is the opposite of fission: nuclear fusion. Fusion is the process whereby two light nuclei collide with enough energy to overcome the long ranged electrical repulsion, and come close enough to fuse by the short ranged nuclear attraction. An example of a fusion reaction is the deuterium tritium or D-T reaction:



where the 17.6 MeV of energy is due to the slight difference in mass between products and which appears as the kinetic energy of the neutron and alpha particles. Once the reaction can be made to occur on a large scale there is existing technology to convert the energy of the neutron shown in equation 1.2 into thermal energy to generate steam and drive electricity-generating turbines. The alpha particle in equation 1.2 is confined by the magnetic field so dwells long enough in the plasma region to heat the plasma and sustain the reaction. Fusion has significant advantages over fission: radioactivity in the waste products is very short lived, the deuterium can be extracted from abundant sea water and the tritium can be derived from neutronic collisions with a lithium blanket surrounding the reactor. And, since there are no heavy isotopes involved in the reaction, the political bugbear of deciding which states can have fissionable fuel based on fear of weapons proliferation is avoided.

## 1.2 The plasma state and plasma confinement

Since the kinetic energy of the deuterium and tritium reactants in equation 1.2 must be many orders of magnitude higher than their ionisation energies the reaction takes place in the plasma state. That is, the reactants are liberated of their orbiting electrons which remain present as a negative fluid of equal number density to the D and T ions. In this thesis the number density of electrons will be denoted  $n_e$  and the number density of ions  $n_i$ .

In the presence of a magnetic field the charged component particles of the plasma travel along an approximately helical path the centre of which is a field line. The radius (known as the gyro-radius  $\rho_c$ ) and temporal frequency (known as the cyclotron frequency  $\omega_c$ ) of this path are given by equation 1.3

$$\rho_c = \frac{mv_{\perp}}{|q|B} \quad \omega_c = \frac{|q|B}{m} \quad (1.3)$$

where  $m$  is the mass of the particle,  $q$  is the particle charge (which, for singly ionised atoms and electrons is  $e = \pm 1.602 \times 10^{-19}\text{C}$ ) and  $v_{\perp}$  is the component of the velocity

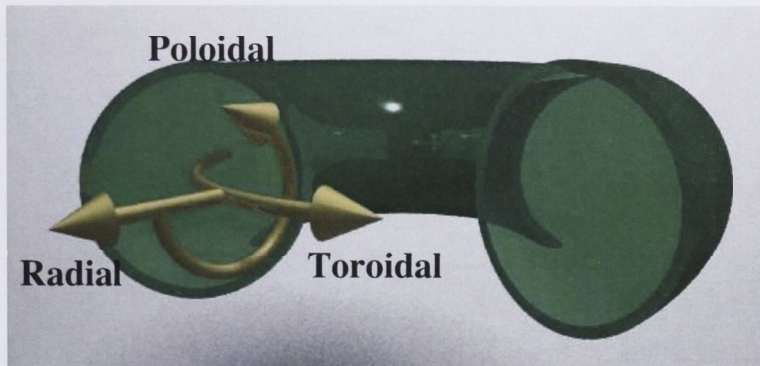


Figure 1.2: Co-ordinates used when describing toroidal geometries

of the particle perpendicular to the magnetic field of strength  $B$ .

As can be seen in equation 1.3 the gyro radius is inversely proportional to  $|B|$  so the stronger the magnetic field, the tighter the orbits. In a device that confines plasmas using magnetic fields, magnetic field lines are wrapped back on each other to form a toroid or “doughnut” shape to prevent losses from the ends. Figure 1.2 shows the direction of the radial ( $r$ ), poloidal ( $\theta$ ) and toroidal ( $\Phi$ ) co-ordinates which will be used in this thesis.

Consider a plane defining cross section of the torus and the points at which the magnetic field lines puncture the plane (puncture points). As the magnetic field line wraps around the torus the puncture points precess around this plane tracing out a cross section of what is known as a flux surface. Examples are shown in the panels of figure 1.5. As a charged particle gyrates around field lines in the torus, gradually covering a flux surface, it will experience a variation of both the direction and gradient in the magnetic field. This causes deviations of the orbit from the field line known as the curvature and gradient drifts which cause charge separation in the vertical direction. To combat this, a poloidal component must be added to the magnetic field to allow charge to flow and cancel out the charge separation. The only way to add this and retain closed flux surfaces is to add a helical component to the toroidal magnetic field. A measure of helicity or the poloidal twist per toroidal turn is known as the rotational transform ( $\iota$ ). The rotational transform and its associated rate of change, or shear ( $\hat{s}$ ), is given by

$$\iota = \frac{N_{pol}}{N_{tor}} \quad \hat{s} = \frac{\psi}{\iota} \frac{d\iota}{d\psi} \quad (1.4)$$

where  $N_{pol}$  is the number of poloidal transits per  $N_{tor}$  toroidal transits, and  $\psi$  is the magnetic flux contained in a flux surface which increases monotonically with the minor radius of the torus. A common co-ordinate space used in this thesis is

normalised flux given by  $s = \psi/\psi_{total}$ . When  $\iota$  has a rational value the magnetic field line precesses poloidally, ultimately connecting back to its starting point only puncturing the plane at a finite set  $N_{pol}$  of points after  $N_{tor}$  toroidal turns. In the presence of perturbations along the magnetic field lines these rational surfaces can form magnetic islands which are closed surfaces around the rational field lines. Islands are bad for confinement as they effectively connect field lines across flux surfaces. To achieve good confinement of charged particles it is necessary to have a set of nested flux surfaces with non-zero  $\iota$  which either avoids or minimises the effect of rational surfaces.

### 1.2.1 Magnetic confinement configurations

The two most common toroidal configurations are the stellarator and the tokamak. In a tokamak, which has a fairly simple magnetic structure, the poloidal component of the magnetic field is generated by the current flowing within the plasma. The disadvantage of having a confining magnetic field dependent on the plasma it is confining, is that a sudden change in the properties of the plasma can suddenly change the magnetic field. This can lead to a destructive feedback loop which can quickly spoil confinement and lead to the disruptive (hence the name of these events: disruptions) dissipation of the magnetic energy, often into kinetic energy of the magnetic coil set which can be damaging to the device.

A stellarator, first proposed by Spitzer [Spitzer, 1958], overcomes this problem by using only external field coils to generate flux surfaces. This means the confining magnetic field is independent of the plasma being confined, so that stellarators are not prone to disruptions. The disadvantage of stellarators over tokamaks is that, as a result of removing the plasma current the construction of the coil set is difficult and the shape of the resulting flux surfaces can be complex. However, recent advances in the computer aided design and manufacture of non-circular and non-planar coil shapes has removed some of the difficulties involved.

Early stellarator designs fall into two main classes, the heliotron/torsatron, such as the Large Helical Device (LHD) [Motojima et al., 1999], in which the transform is produced by helical coils, and those in which the transform is produced by a helical displacement of the plasma known as helical or spatial axis designs (such as the H-1NF heliac). A more recent class is the modular coil stellarator, for example the Wendelstein 7-X (W7-X) [Feist, 2003] device, whose coils are shaped in a complex way to produce transform, yet are easily separated for maintenance, unlike the linked coils of both earlier classes.

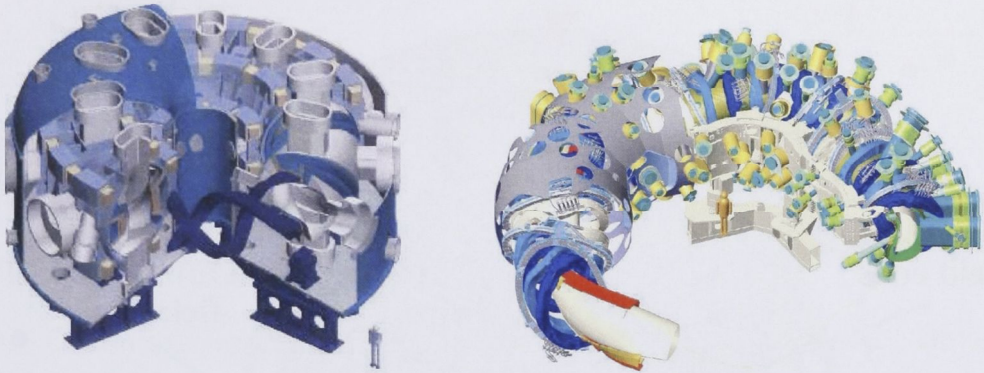


Figure 1.3: The Large Helical Device (LHD) in Japan, which uses helical windings to introduce twist, and the Wendelstein 7-X (W7-X) device in Germany which uses warped modular coils (both shown in dark blue). The red helical structure on W7-X device is a divertor plate.

### 1.3 The H-1NF heliac

The H-1NF heliac [Hamberger et al., 1990] is a three period flexible heliac. A heliac is a stellarator with circular toroidal field coils (TFC) positioned such that the centre of the coils traces a helix winding around a central ring coil known as the poloidal field coil (PFC). A flexible heliac [Harris et al., 1985] is a heliac with a helical field coil (HFC) wrapped around the PFC in phase with the helical plasma axis. The key physical property of a flexible heliac is that varying the ratio of the current in the HFC to the current in the TFCs gives direct control over the magnetic configuration and associated rotational transform and shear.

Figure 1.5 shows Poincaré plots <sup>†</sup> of magnetic flux surfaces (at  $\Phi=0^\circ$ ) and plots of the rotational transform profile for a variety of values of  $\kappa_h$  where  $\kappa_h$  is the ratio of the current in the HFC to the current in the TFC.

The magnetic field coils are energised using an ABB-Technicon power supply, which is capable of delivering up to 14000 Amps at 800 Volts. The power supply features two current outputs (which will be denoted as the main and secondary supplies) which can be independently controlled. Normally, the secondary supply is connected to the HFC with the main connected to the rest of the coil-set in series. The resolution of current control is better than 1 amp which allows control of the on-axis rotational transform to 1 part in 1000.

Basic operational parameters of the H-1NF device compared with major fusion

---

<sup>†</sup>A Poincaré plot is a plot showing where magnetic lines of force (trajectories of a massless particle intersect a plane. In the context of this thesis the plane will always be in the  $(r,\theta)$  plane

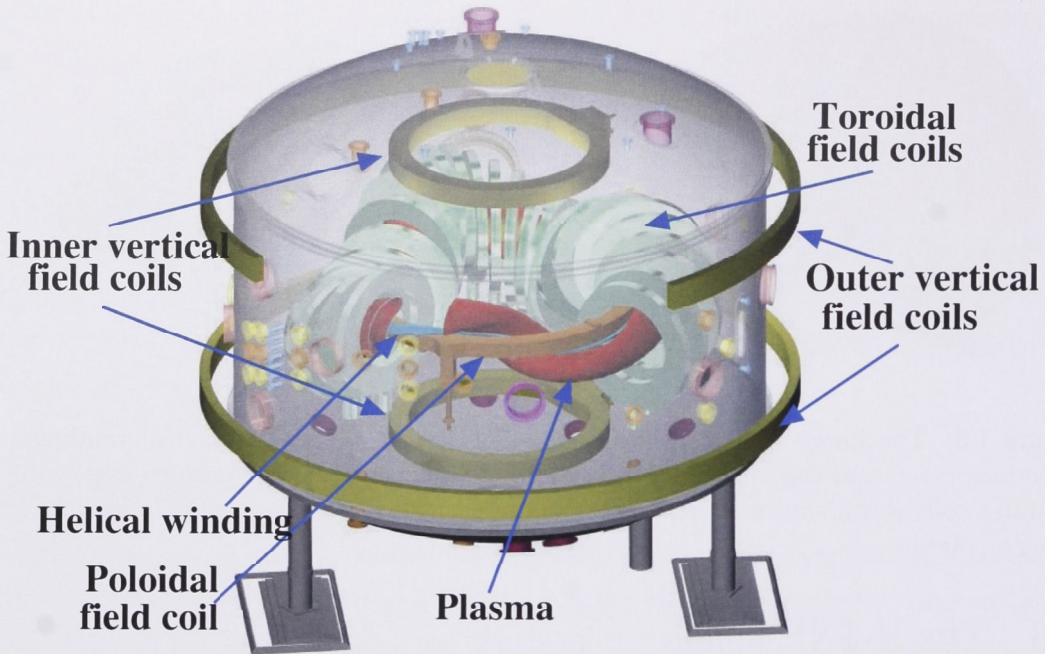


Figure 1.4: The H-1NF flexible heliac

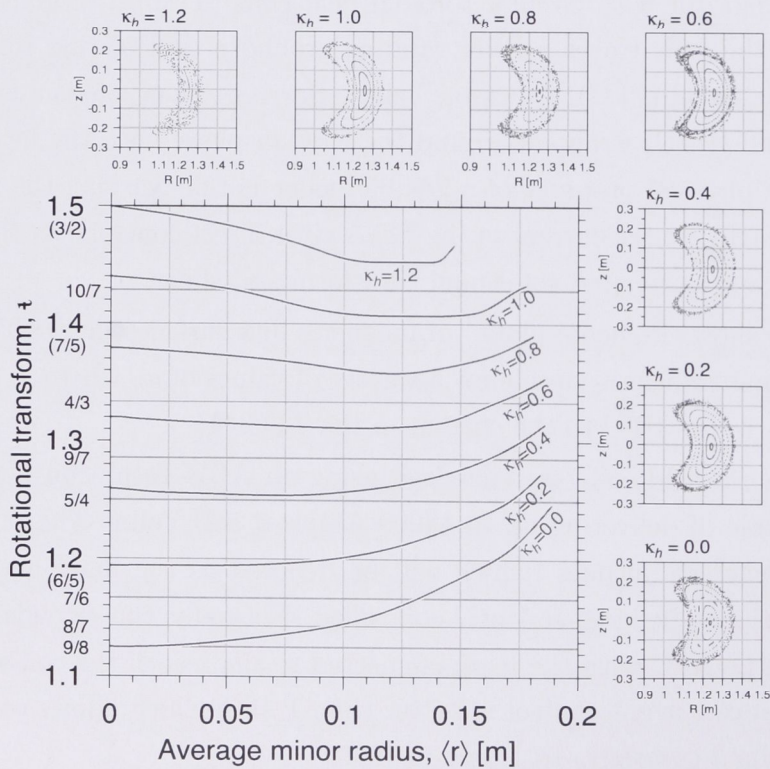


Figure 1.5: Magnetic configuration as a function of the helical coil current ratio,  $\kappa_h$ . Panels show Poincaré plots of the flux surfaces at  $\Phi=0$  degrees. Image courtesy of David Pretty.

Device	H-1NF	LHD	W7-X
$B_0$ (T)	0.5	4	3.0
Major radius (m)	1.0	8	5.5
Minor radius (m)	0.1 - 0.2	1.0-1.2	0.53
Axis transform $\iota$	0.6 - 1.9	0.5 <sup>†</sup>	0.83 - 1.25
(ECH:RF:NBI) (MW)	0.2:0.1:0	2.1:2.7:13	10:3:18 (on completion)
Location	Australia	Japan	Germany (under construction)

Table 1.1: Parameters of the H-1NF heliac compared to LHD and W7-X. †: Affected by Shafranov Shift.

devices in Germany and Japan are shown in table 1.3. As shown in the table the H-1NF is a smaller device which is aimed at fundamental plasma research that is scaleable to larger, fusion relevant, devices.

### 1.3.1 Vessel and fuelling

The H-1NF device uses a coil-in-tank design. That is, the 36 TFCs, two inner vertical field coils, PFC, HFC and associated connectors and cooling hardware sit inside the 33 cubic metre vacuum vessel. While this causes problems with plasma density control (as will be shown in chapter 2) it greatly improves diagnostic access to the plasma, with respect to coil outside tank machines.

The vacuum vessel is pumped out by two 2200 l/s turbo molecular pumps, which are backed by rotary pumps, which produce a combined pumping speed 3000l/s for  $N_2$ . In addition there is a cryogenic pump which helps reduce water vapor pressure. The calculated pumping speed for the cryo pump is 64,000 l/s for water vapor only. Pressure inside the tank is measured using an ion gauge which is calibrated using a Baratron at higher pressures. The ultimate vacuum reached before the addition of fuelling gasses is  $1 \times 10^{-7}$  Torr.

The standard method of fuelling the plasma is by flow filling the vacuum vessel to a set pressure with the fuelling gas. The gas (usually ultra-pure, 99.9999% pure) is let into the vacuum vessel through mass flow controllers. Since the pump rate (in particles per second) of the turbo pumps is dependent on the local gas density, an equilibrium is reached between the rate of flow from the controllers and pump out from the turbo pumps. This means that the mass flow controllers can be used to control the neutral particle density in the H-1NF vessel.

As will be discussed in section 2.3 this method of fuelling, known as “static fill”, provides a constant source of particles which thermally diffuse into the plasma

region. In chapter 5 we introduce a new fuelling method which uses a directed supersonic molecular beam.

### 1.3.2 Plasma heating systems

This section provides an overview of the heating systems on H-1NF; a brief discussion of the physics of resonant heating is presented in section 2.3. There are two heating sources for the H-1NF heliac: ion cyclotron resonant heating (ICH) and electron cyclotron resonant heating (ECH). The ICH system involves four phased 30kW (120kW total) class AB 7MHz AWA radio transmitters connected to a double loop antenna shown in figure 1.6. The forward and reverse powers are measured using couplers and recorded for further analysis.

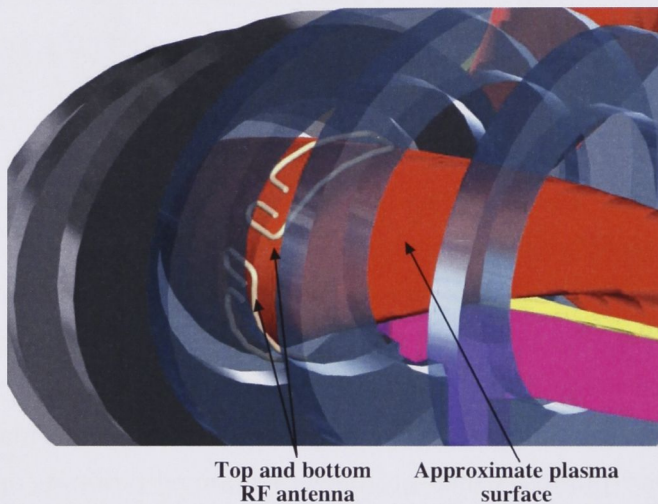


Figure 1.6: Location of RF (7MHz) antenna

The ECH system [Punzmann, 2000] uses a 28GHz gyrotron to generate up to 200kW of TE02 microwave power. This mode is then converted to the HE11 mode for efficient transmission along a corrugated wave guide. As shown in figure 2.8 of section 2.3.1 the wave is directly launched across the plasma.

## 1.4 Plasma diagnostics and data storage

Due to the tenuous and typically inhospitable nature of the plasmas studied on the H-1NF heliac we use non-contact measurement techniques whenever possible to limit the perturbation on the plasma and damage to the instrument. There are three main diagnostic systems used in this thesis: interferometric systems for measuring the electron density  $n_e$  (section 2.1), a helium beam diagnostic (HBD)

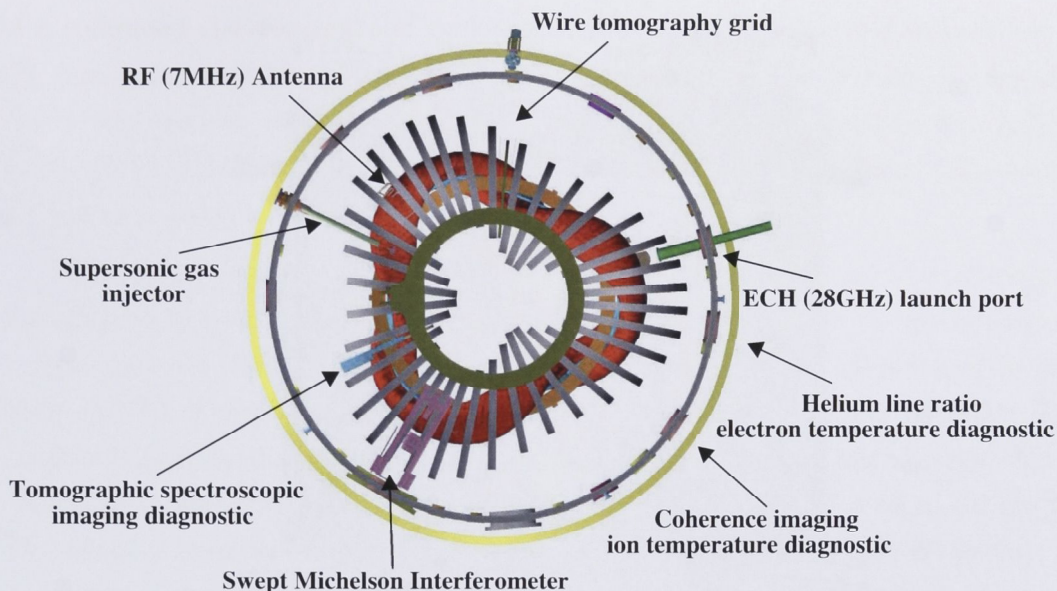


Figure 1.7: A top view of the H-1NF heliac showing the location of major diagnostics

for the measuring the electron temperature  $T_e$  (chapter 3) and a coherence imaging camera for measuring the ion temperature  $T_i$  (section A.1). It should be noted that the HBD  $T_e$  diagnostic was not available when the studies presented in chapter 2 were carried out. Figure 1.7 shows a top view of the H-1NF device with the position of the major diagnostics marked.

Data from these diagnostics is digitised using transient recorders based on an international standard interface known as CAMAC. Data stored in the digitisers is read out over an Ethernet network and stored in an MDSPlus [J.A.Stillerman, 1997] database for long term storage and post-shot analysis.

## 1.5 ITER

H-1NF and the other devices mentioned in the previous sections are research machines for investigating the plasma physics of magnetically confined plasma. ITER (International Thermonuclear Experimental Reactor) is the penultimate step in the chain of research towards a fusion reactor. ITER is an international project involving the European Union, the Russian Federation, the United States, South Korea, India, Japan and China and will investigate the physics of a burning plasma. A burning plasma is a plasma where the energy deposited into the plasma via the energetic alpha particle in equation 1.2 provides most of the power necessary to heat and maintain the plasma. It will be important to consider this work in the context

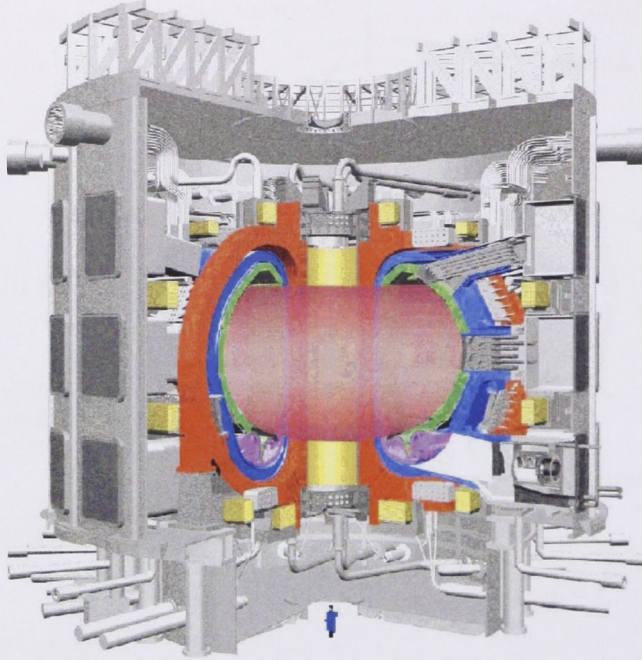


Figure 1.8: A diagram of ITER showing a human as scale. One of the reasons for the massive size of the ITER plasma is to ensure that energetic alpha particles (from the reaction shown in equation 1.2) have enough time to collisionally transfer energy to the bulk plasma.

of ITER as the diagnosis of the ITER plasma will be of paramount importance on the path to understanding the plasma environment in a fusion power plant.

## 1.6 Thesis overview

The remainder of the thesis is structured as follows:

Chapter two discusses studies of plasma formation at 0.5 tesla in the H-1NF heliac using density interferometry. The chapter begins by introducing the two density interferometers that were used to obtain the results presented throughout this thesis: the far infra-red scanning interferometer and the electronically scanned interferometer. The chapter then presents a brief discussion on the techniques used to convert the line integrated data returned by the interferometers to spatially localised data. We present a candidate mechanism for the resonant heating of ions in the plasma: ion minority heating. This is followed by a brief discussion of the physics of electron cyclotron resonant heating. The chapter then presents a study of the effect of magnetic configuration on plasma formation followed by a study of the effect of the position of the resonant layer. The chapter concludes with a discussion

of a combined electron and ion cyclotron heated plasma. This discussion leads to the conclusion that the plasma is being uncontrollably fuelled by the background gas in the vacuum vessel, highlighting the requirement for a fuel delivery system which preferentially fuels just the plasma volume while limiting flow to the rest of the vacuum vessel.

To facilitate the design and analysis of a fuelling system we required knowledge of the electron temperature ( $T_e$ ) profile of the target plasma. Chapter three presents a helium line ratio (HLR) diagnostic that is based on a diagnostic supersonic molecular beam (SMB). The system is referred to as the helium beam diagnostic (HBD). The chapter begins by discussing the HLR technique including an introduction of the collisional radiative model (CRM) used to model helium emissivities and the optics. The chapter then introduces the HBD, which was installed on H-1NF as part of a collaboration with the University of Sydney plasma physics group. We then present a study of the localisation of the beam and its suitability for multi-pulse injection. The chapter concludes with a discussion of the procedure used to derive the temperature profiles and presents a sample result.

Following the verification of the performance of the HBD, chapter four presents a study of plasmas formed using electron cyclotron heating. The chapter begins with a discussion of the plasma preparation method and then presents some typical  $T_e$  and  $n_e$  profiles. The energetics of a typical ECH plasma is discussed and calculations of the electron energy confinement time and plasma electron beta are presented. The chapter concludes by simulating the propagation of the HBD into the plasma and comparing the simulated helium brightness with experimental data.

Using knowledge of the target plasma gained in chapter four, chapter five discusses the theory, design, testing and simulation of a directional gas injection system for the H-1NF heliac. The chapter begins by providing an overview of the techniques used to fuel magnetically confined plasmas and then introduces the theory for compressible flow through a nozzle. The chapter presents the system design and introduces the key diagnostic technique used to characterise the flow: constant temperature hot wire anemometry (CTA). Results from the characterisation are presented and compared to the theoretical results from earlier in the chapter. Using a simple collision theory the penetration of the beam into the plasma is modeled. Following the good agreement between the simulations performed using the TD CRM and measured emissivities reported in chapter four we conclude the chapter by presenting a study of beam plasma interaction using the TD CRM including a calculation of the perturbative effect of the beam on the stored electron energy.

Chapter six concludes the thesis by summarising work in the preceding chapters and discusses ideas for future studies based on the results presented in this thesis.

At the end of the thesis there are several appendices as well as tables of figures, acronyms and symbols used in this thesis for quick reference.

# Interferometric studies of hydrogen ion resonant plasma formation

A common mistake that people make when trying to design something completely foolproof is to underestimate the ingenuity of complete fools

– *Douglas Adams*

The initial aim of this thesis was to study particle transport in the H-1NF heliac at magnetic fields around 0.5 Tesla using particle source modulation. As stated in chapter 1 initial studies of plasma formation indicated that H-1NF plasmas were being un-controllably fuelled by the background static fill making particle transport studies difficult. This chapter details the first interferometric studies of plasma formation at 0.5 Tesla.

This chapter begins by introducing the interferometry systems on the H-1NF heliac. An overview of the plasma preparation at 0.5T in the H-1NF heliac is then presented. This includes a discussion of a proposed mechanism for the resonant heating of ions in the H-1NF heliac: ion minority heating. We present a survey of plasma formation using RF heating in the ion cyclotron range of frequencies as a function of magnetic configuration and magnetic field (which changes the position of the region where the ion-cyclotron orbit is resonant with the heating wave). A study of a discharge using both ion and electron resonant heating is presented which shows a ramp in the electron density when extra heating power is applied. It should be noted that there was no reliable diagnostic for electron temperature during this study. The system detailed in chapter 3 was developed after the completion of these studies.

## 2.1 Density Interferometry

A key physical property of plasmas is the electron density,  $n_e$ . Due to high electron temperatures it is difficult to perform direct local measurements (e.g. Langmuir probe) of  $n_e$ . Instead, we use millimetre radiation (in the range of 2mm to 743 $\mu$ m or 150 to 403GHz) to measure the refractive index of the plasma using plasma density interferometry.

When a beam of radiation, with an angular frequency  $\omega$ , propagates along a path  $\ell$  through a plasma with electron density  $n_e$  it undergoes a phase shift (compared to the phase shift of a beam that propagates along the same path in vacuum) of [Hutchinson, 1987],

$$\Delta\phi = \frac{-\omega}{2cn_c} \int_{\ell} n_e dl \quad (2.1)$$

where  $n_c$  is the cut off density for propagation of the beam and is given by

$$n_c = \omega^2 m \epsilon_0 / e^2 \quad (2.2)$$

where  $m$  and  $e$  are the mass and charge of the electron and  $\epsilon_0$  is the permittivity of free space.

By shifting the frequency of the probe beam (the beam affected by the plasma) and mixing it with a local oscillator beam (a beam unaffected by the plasma and which has a different path length to the probe) a beat signal is produced at the detector proportional to  $\cos(\Delta\omega t + \Delta\phi)$  where  $\Delta\omega$  is the difference in frequencies between the two beams and  $\Delta\phi$  is the difference in phase (of which the plasma induced phase difference in equation 2.1 is a component). This is known as heterodyne phase detection. Therefore, by monitoring the phase change in the beat signal the line integrated electron density can be deduced. There are three different interferometry systems in use on the H-1NF Helic. Routine chord averaged density information is obtained using a simple Michelson interferometer. The viewing geometry of the system is shown in figure 2.1). A swept IMPATT diode with a centre frequency of 141GHz ( $\lambda \sim 2$ mm) is the source. The system has a frequency response of up to 85kHz and a density resolution of  $\leq 5 \times 10^{16} \text{m}^{-3}$  compared to a typical H-1NF line-averaged density of  $2 \times 10^{18} \text{m}^{-3}$ .

As can be seen in figure 1.4 the H-1NF plasma has a complex shape. Therefore, to obtain information about the local plasma density (as against the line integrated plasma density) we need multiple measurements of the line average electron density along different chords and viewing directions. This will allow a reconstruction of the density profile using simple inverse methods (as discussed in section 2.2) to

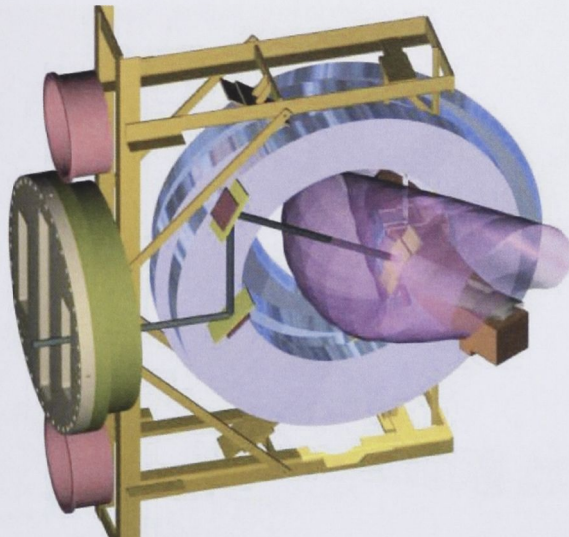


Figure 2.1: Launch geometry for the 2mm Michelson heterodyne density interferometer used to routinely measure the line-averaged electron density in H-1NF. The internal support structure for the scanning interferometers, which is toroidally displaced by one field coil, is also shown.

be performed. Two multi channel interferometers were used to obtain the density profiles presented in this thesis: the far infra-red (FIR) scanning interferometer [Howard, 1990] (section 2.1.1) and the electronically scanned microwave interferometer (ELSI) [Howard & Oliver, 2006] (section 2.1.2). To obtain an improved signal to noise ratio and to reduce the amount of hardware required both these devices sweep a beam across the plasma (effectively multiplexing the spatial information into the time domain) with the key difference between the measurements being the method of effecting the sweep.

### 2.1.1 The far infra-red scanning interferometer

The key component of the FIR Interferometer is a wheel with a grating that has a grating constant (or groove spacing),  $d$ , that varies periodically and continuously around the wheel circumference. Radiation incident upon the grating at an angle  $\alpha$  will be diffracted off at an angle  $\beta$  as shown in equation 2.3 (where  $\lambda$  is the wavelength of radiation,  $d$  is the groove separation and  $m$  is the order of the diffraction).

$$\sin \alpha + \sin \beta = \frac{m\lambda}{d} \quad (2.3)$$

When this wheel is rotating it provides (via the Doppler effect) a frequency offset for heterodyne detection and, because of the changing grating constant, effects a smooth

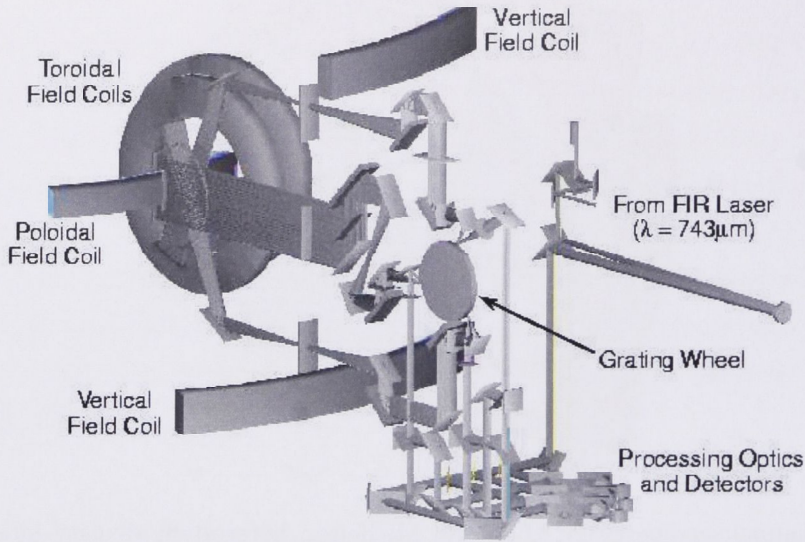


Figure 2.2: A Gaussian ray trace of the swept FIR interferometer showing the static optics and the rotating grating wheel at the centre of the device which is used to both provide a frequency shift for heterodyne detection and effect a spatial sweep of the plasma. The figure is effectively a long time exposure, at any one instant in time only a single chord in each of the views is active

spatial scan of the plasma. This wheel replaces a stepped design used previously [Warr, 1998]. The use of a continuously varying groove constant increases the duty cycle by reducing the number of transitions in the grating constant, which can cause loss of signal.

Figure 2.2 shows a Gaussian ray trace of the multi view system [Warr & Howard, 2001] with three plasma views installed. The support structure (figure 2.1) for the mirrors on the vacuum side of the H-1 vessel is connected to an external vibrationally-isolated optical table via rods passing through flexible vacuum bellows. The  $743\mu\text{m}$  wavelength probe radiation is produced using an optically pumped far infra-red laser mounted on the optical table. With the grating wheel rotating at 6000RPM (the wheel drive was upgraded from the air turbine reported in the early literature to an electric motor) and using a wheel with six identical partitions (the grating constant changes in a sawtooth manner six times per revolution) a single scan of the plasma can be performed in 2ms. The fan of diffracted beams is collected by monolithic parabolic and cylindrical reflectors and launched into the plasma where it has a full width at half maximum of 2cm at the plasma centre.

To maximise the signal to noise ratio it was necessary to restrict (temporarily)

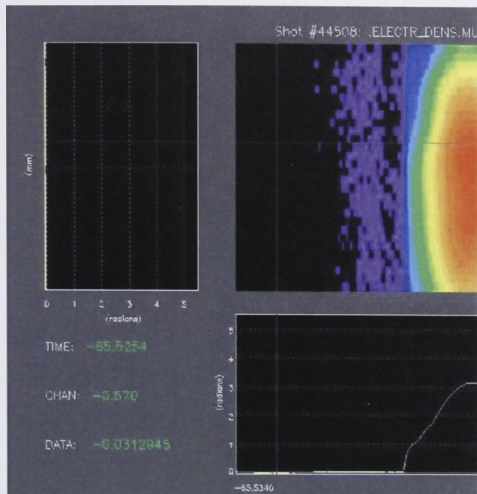


Figure 2.3: Sample data (projections) measured during a combined ion/electron resonantly heated discharge.

the interferometer operation to the top-launched diagonal view of the plasma only. This achieves RMS phase noise levels of around 0.01 radians compared to a plasma-induced phase shift of up to 3.5 radians.

Signals are detected using corner-cube Schottky diode detectors. The signals are amplified and digitised directly, and the phase demodulation is performed numerically post-shot. The continuously sampled phase projection  $\phi(p)$ , where  $p$  is the impact parameter, is binned into a preset number of spatial channels  $\phi_i(t)$ ,  $i = 1 \dots N$ , chosen to obtain a satisfactory trade-off between spatial resolution and signal to noise ratio. We typically choose  $N=30$ . A Fourier shifting algorithm is used to correct for the non-simultaneous spatial sampling due to the scanning nature of the interferometer. The discretised projections are stored in the MDSPlus data base and can be used to study the dynamics of a particular shot by either examining moments of the projection, as shown in section 2.5, or performing an Abel inversion to obtain the electron density profile as shown in section 2.4. Figure 2.4 shows Poincaré plots of the magnetic surfaces for on-axis rotational transforms of 1.22, 1.32 and 1.45 and illustrates the interferometer spatial coverage with changing magnetic configuration. Also shown are representative snapshots of the density projections (crosses), their functional best fit and the inverted density profile as a function of major radius.

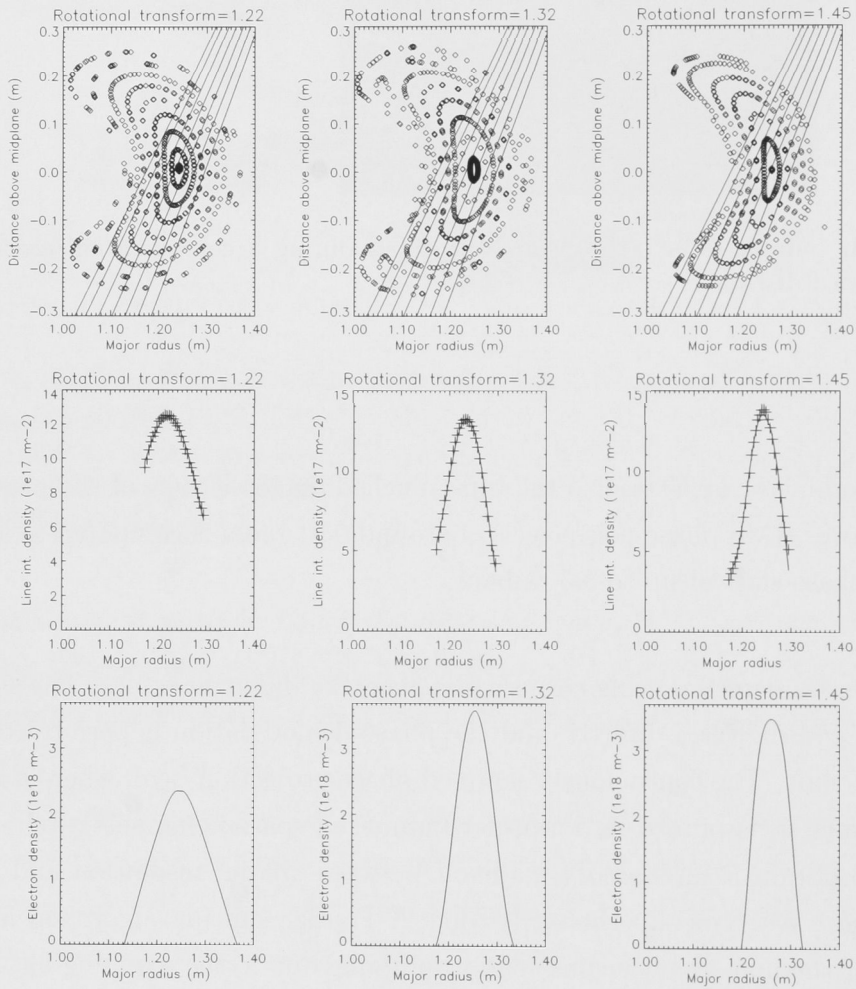


Figure 2.4: Variation with the magnetic configuration (left to right) of the plasma coverage of the top diagonal view (top), projections shown as crosses and the best fit as a solid line (centre), and reconstructions of the density profile (bottom).

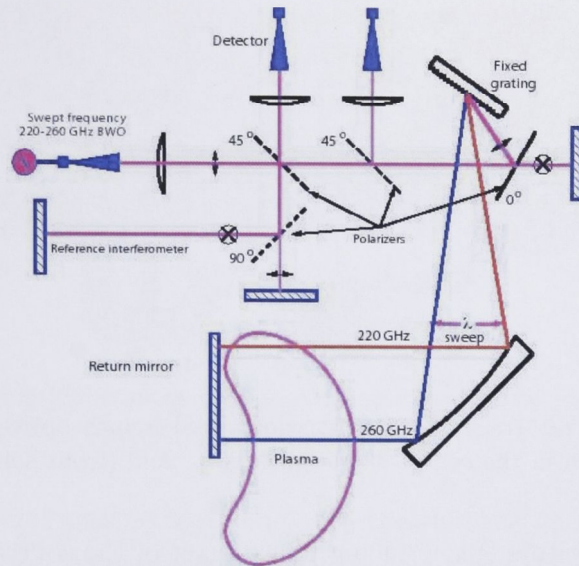


Figure 2.5: Layout of the electronically scanned interferometer. The blue path is the path taken by the radiation at the high frequency side of the scan while the red path is the path taken at the low frequency side of the scan. (from [Howard & Oliver, 2006])

### 2.1.2 The electronically scanned interferometer

While the FIR interferometer uses a fixed frequency source and a rotating grating wheel to achieve a scanning heterodyne Michelson interferometer the ELSI uses a high power (100mW) voltage-tuneable (180-280GHz) microwave source known as a backward wave oscillator or BWO and a fixed grating. So instead of varying  $d$  (in equation 2.3) to vary  $\beta$  ELSI uses a varying  $\lambda$  to obtain the same result. The operating frequency of the BWO is set by an input low-voltage control signal.

A basic diagram of the optical layout of the ELSI device is shown in figure 2.5 and a Gaussian ray trace of the launch optics is shown in figure 2.6. ELSI uses the same optical table and internal support structure and vacuum side mirrors as the swept FIR system. The system uses a blazed static grating ( $m=1$ ,  $d=0.91\text{mm}$ ,  $\alpha=60^\circ$ ) and a sweep from 220GHz to 280GHz which gives the scan shown in figure 2.6. Again the beam width in the plasma is approximately 2cm.

Because of the rapid frequency sweep the difference in path length between the probe and local oscillator ( $\Delta L$ ) gives a convenient intermediate (beat) frequency proportional to the sweep rate ( $df/dt$ ) and  $\Delta L$ . The maximum sweep rate of the source is limited by the bandwidth of the internal high voltage amplifier that amplifies the control signal and provides the cathode bias. The BWO drive electronics

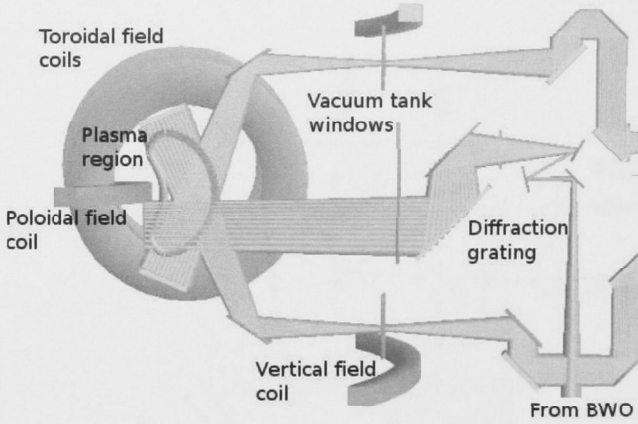


Figure 2.6: A Gaussian ray trace of the three view ELSI launch optics and paths in the plasma. The beam width in the centre of the plasma is 2cm (from [Oliver et al., 2006])

uses output filter capacitors (for reducing phase jitter of the source) which sets the bandwidth to 10kHz. A sweep time of 2ms was chosen as a trade off between scan speed intermediate frequency and duty cycle (due to the reset time of the device between sweeps).

One advantage of ELSI over the FIR system is the removal of moving components (notably the wheel) which greatly reduces instrument vibrations and associated spurious phase shift. This allows a phase noise level of order 0.04 radians to be achieved (compared to a plasma phase shift of order  $2\pi$ ). Another advantage of ELSI is that by varying the range of the control sweep voltage, the range of frequencies emitted from the device can be varied and hence the range of diffraction angles off the fixed grating. This allows the operator to construct a tailored spatial sweep depending on the type of plasma phenomena being studied. As with the FIR system the interferograms from the ELSI system are digitised and stored to the MDSPplus database and the phase is numerically demodulated post shot.

## 2.2 Inverse techniques

Both the density interferometers and ion coherence imaging diagnostic (which will be introduced in appendix A) return a line integrated measure of plasma parameters. This is useful as a quick check on the plasma conditions. However, to perform any in-depth physical study of plasma phenomena the local information (for example  $n_e(\mathbf{r})$ ) must be unfolded. Both the FIR interferometer and the coherence imaging diagnostic were restricted to a single fan of line integrals with a similar impact angle. This restricts our options for inverting the profile and forces

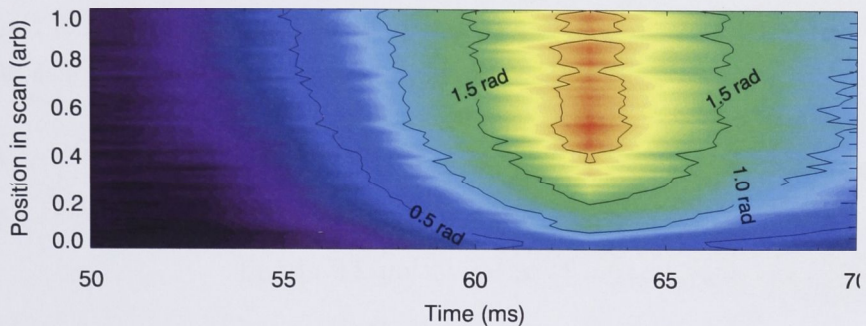


Figure 2.7: Plasma induced phase shift as a function of time and scan position (0=plasma edge 1=plasma centre) measured using ELSI

us to rely on a-priori assumptions about the shape of the plasma.

The array of  $i$  line integrated measurements along the diagnostic viewing chords,  $\ell_i$  at a given viewing angle, is known as the projection or  $\{P_i\}$  of the object  $I(\mathbf{r})$

$$P_i = \int_{\ell_i} I(\mathbf{r}) d\ell. \quad (2.4)$$

$I(\mathbf{r})$  can be expressed as a linear combination of orthogonal basis functions,  $f_k(\mathbf{r})$ , given by

$$I(\mathbf{r}) = \sum w_k f_k(\mathbf{r}) \quad (2.5)$$

where  $w_k$  is the weighting of the  $k$ th function. This technique is analogous to an Abel inversion. The choice of basis function is influenced by the expected form of  $I(\mathbf{r})$ . One basis set which was used in the reconstruction of the FIR density data was Fourier-Bessel functions mapped onto the flux surfaces shown in figure 2.4. The basis set used in the reconstruction of the ELSI data was a set of flux surface shaped pixels, i.e. rings of constant minor radius.

The  $j$ th element of the projection of  $I(\mathbf{r})$  is given by

$$P_j = \int_{\ell_j} \sum_k w_k f_k(\mathbf{r}) d\ell \quad (2.6)$$

$$= \sum_k w_k R_{kj} \quad (2.7)$$

where

$$R_{kj} = \int_{\ell_j} f_k(\mathbf{r}) d\ell \quad (2.8)$$

Defining  $\mathbf{P}$  to be the array of  $j$  projections,  $\mathbf{w}$  to be the array of  $k$  weights for the basis functions which form the object and  $\mathbf{R}$  to be the  $k \times j$  matrix of the integrals of the basis functions over the viewing chords (often called the response matrix) we can express equation 2.7 as

$$\mathbf{P} = \mathbf{R}\mathbf{w}. \quad (2.9)$$

Knowledge of the array or weights  $\mathbf{w}$  allows us to (using equation 2.5) reconstruct the object. Therefore we re-arrange equation 2.9 giving

$$\mathbf{w} = \mathbf{R}^{-1}\mathbf{P} \quad (2.10)$$

where  $\mathbf{R}^{-1}$  is the inverse matrix of the response matrix  $\mathbf{R}$ . Often  $\mathbf{R}$  is non-square so singular value decomposition is used. For details of this treatment see pages 33-4 of [Warr, 1998].

For the results presented in this chapter (using the FIR system) we used the three lowest order  $J_0$  Bessel functions which are mapped onto the magnetic flux surfaces using an interpolation of the puncture points calculated by the Gourdon code [Gourdon et al., 1971] (see appendix A of [Michael, 2003]). The response matrix,  $\mathbf{R}$ , is then pre-computed for a range of magnetic configurations. The matrix  $\mathbf{R}^{-1}$  is applied to the measured projections to obtain the object  $I(\mathbf{r})$ .

To test the ‘‘goodness of fit’’, the re-constructed object is re-projected using the response matrix, back onto the viewing chords and compared with the original data. An example of the re-projections is shown in figure 2.4. To obtain a numerical indication of the fidelity of the fit we calculate the normalised residual,  $\epsilon$ ,

$$\epsilon = \sum_j \sqrt{\left( \frac{P_i}{\sum_k P_k} - \frac{(\mathbf{R}\mathbf{w})_j}{\sum_k (\mathbf{R}\mathbf{w})_k} \right)^2} \quad (2.11)$$

and where  $\mathbf{R}\mathbf{w}$  is the array of re-projections of the reconstructed image using equation 2.9. While  $\epsilon$  can give an indication of the goodness of fit of the re-projection to the projection an  $\epsilon \rightarrow 0$  does not always mean that the re-constructed object will be an accurate representation of the real object. For example, the use of Fourier Bessel functions can generate negative density artefacts. Also, we are limited by our assumptions of constant values on a flux surface and, as shown in [Warr, 1998], for some oscillating plasmas this may not be the case.

## 2.3 Experimental conditions at 0.5 Tesla

Fuelling to the plasmas studied in this section is provided using a method known as ‘‘static fill’’ as defined in section 1.3.1. For the experiments presented here we used

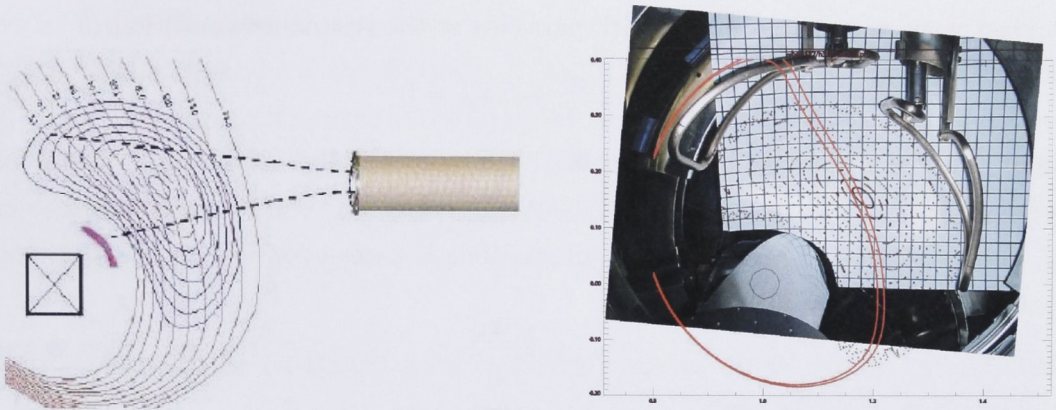


Figure 2.8: The left panel shows the end of the ECH waveguide with the approximate beam width of the directly launched 28GHz X-mode radiation while the right panel shows a photograph of the double saddle antenna used to launch the 7MHz ICH wave into the plasma. Both images are overlaid with a Poincaré plot for flux surfaces in standard configuration ( $\kappa_H = 0$ ).

a density of  $0.17 \times 10^{18} \text{m}^{-3}$  helium and  $0.28 \times 10^{18} \text{m}^{-3}$  hydrogen (atoms). As shown in section 2.6 the obtained plasma density is many times higher than the combined neutral fill densities, indicating, after an initial ionisation of neutral particles within the LCFS, fuelling is provided by a thermal flux of particles across the LCFS. For these conditions, the combined flux (helium plus hydrogen) across the LCFS is  $1.3 \times 10^{21}$  atoms per second.

### 2.3.1 Ion cyclotron resonant heating

A double loop antenna (also known as a Boswell antenna [Charles et al., 2003]) shown in figure 2.8 launches 7MHz radiation towards the plasma. The wavelength of the radiation in vacuum is large compared to the width of the plasma so “propagation” is evanescent between the antenna and the layer in the plasma with sufficient refractive index (or electron density) to allow a propagating mode. We assume that during the initial stages of the discharge the local E-field is sufficient to initiate breakdown. To ensure good coupling between the evanescent wave and the fast magneto-sonic wave (FW) the antenna should be within  $1/k_{\parallel}$  of the fast wave cut off in the plasma [Goniche et al., 2003] (where  $k_{\parallel}$  is the wave number parallel to the magnetic field). Increasing the distance between the plasma (cut off layer) and the antenna also filters out higher  $k_{\parallel}$  modes however a detailed study of the k-spectrum of the antenna has not been performed as it was not the main focus of this thesis.

The fast wave strongly interacts with particles at the resonance condition:

$$\omega + n\omega_{res} + k_{\parallel}v_{\parallel i} = 0 \quad (2.12)$$

where  $n$  is the order (or harmonic) of the interaction (for example  $n=1$  implies fundamental),  $\omega$  is the frequency of the FW,  $v_{\parallel i}$  is the ion velocity parallel to  $\mathbf{B}$  and  $\omega_{res}$  is the frequency of the resonant interaction. For example for the ion cyclotron resonance,  $\omega_{res} = \omega_{ci}$ , where

$$\omega_{ci} = \frac{q_i |\mathbf{B}|}{m_i} \quad (2.13)$$

where  $q_i$ , and  $m_i$  are the charge and mass of the ions.

As discussed in [Becoulet, 1996] and shown in detail on pages 32-35 of [Stix, 1992] the FW shows elliptical polarisation and as  $\omega$  approaches  $\omega_{ci}$  the wave polarisation becomes purely right handed circularly polarised. As ions gyrate in a left handed orbit around magnetic field lines the fast wave is unaffected by the presence of an ion cyclotron resonance in the plasma as the wave polarisation at  $\omega = \omega_{ci}$  is in the opposite sense to freely moving ions.

However, coupling of the FW to plasma ions around  $\omega \sim \omega_{ci}$  can be achieved with the addition of a second species through the ion-ion hybrid interaction which has a resonance located between the resonances of the individual ions:

$$\omega_{ii}^2 = \omega_{c1}\omega_{c2} \frac{n_1\omega_{c2} + n_2\omega_{c1}}{n_1\omega_{c1} + n_2\omega_{c2}} \quad (2.14)$$

where  $\omega_{cj}$  and  $n_j$  are the ion cyclotron and densities of the  $j$  th (where  $j=1,2$ ) species of ion. By lowering  $n_1/n_2$  the  $\omega_{ii}$  resonance, and associated increase in amplitude in the wave electric field, moves closer to the  $\omega_{c1}$  resonance. Therefore by introducing a small minority a non-zero wave electric field can be generated in the vicinity of the  $\omega_{c1}$  resonance which will give rise to energy coupling from the FW to the ion population, this method of heating is known as ion minority heating and has been proposed as a possible mechanism for ion heating in the H-1NF Heliac [Blackwell et al., 2002].

### 2.3.2 Electron cyclotron resonant heating

As part of a collaboration between the ANU and Kyoto university a 28GHz gyrotron capable of 200kW has been installed on the H-1NF Heliac for electron cyclotron heating (ECH). The gyrotron is coupled to a mode converter and waveguides (see [Punzmann, 2000] for technical details) to launch a wave into the vacuum vessel with a geometry as shown in figure 2.8. As the wave is launched near perpendicular to the magnetic field the wave propagates primarily in X-Mode (extraordinary

mode) in the plasma and is absorbed at the second harmonic resonance of the electron cyclotron frequency at 0.5 Tesla. Absorption of the X-mode radiation at the 2nd harmonic electron cyclotron frequency is complicated by, as well as being due to, finite Larmor radius (FLR) effects and relativistic corrections. A full treatment of the calculation of the absorption coefficients is given in [Bornatici et al., 1983] and applied to H-1NF along with ray tracing in [Nagasaki et al., 2001].

## 2.4 The effect of magnetic configuration on plasma formation

To understand how magnetic configuration (see section 1.2.1) affects the formation of an ICH heated plasma we used the H-1NF far infra-red scanning interferometer to measure the projection of the plasma density profile for a range of  $\kappa_H$  values (which directly correspond to a range of on axis rotational transforms, see section 1.3). Figure 2.9 shows the raw demodulated data (proportional to the

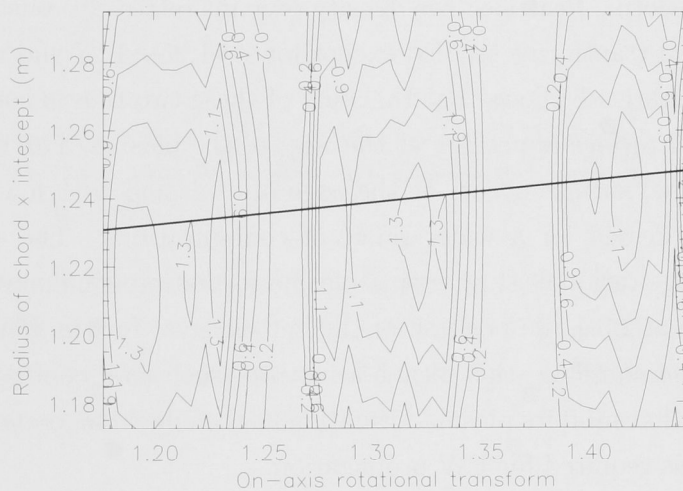


Figure 2.9: Raw demodulated data from the H-1NF scanning interferometer showing the projection of the electron density profile as a function of the on-axis rotational transform

line-averaged electron density) from the interferometer (at the time the maximum density is reached) as a function of impact parameter (where the viewing chord of the interferometer crosses the mid-plane of the plasma) and on-axis rotational transform. The location of the magnetic axis (determined from magnetic field line tracing computation) has been overlaid on figure 2.9 and it can be seen that the peak in the projected profile follows but does not exactly conform to the position of the magnetic axis. To remove line integral affects and to gain a quantitative

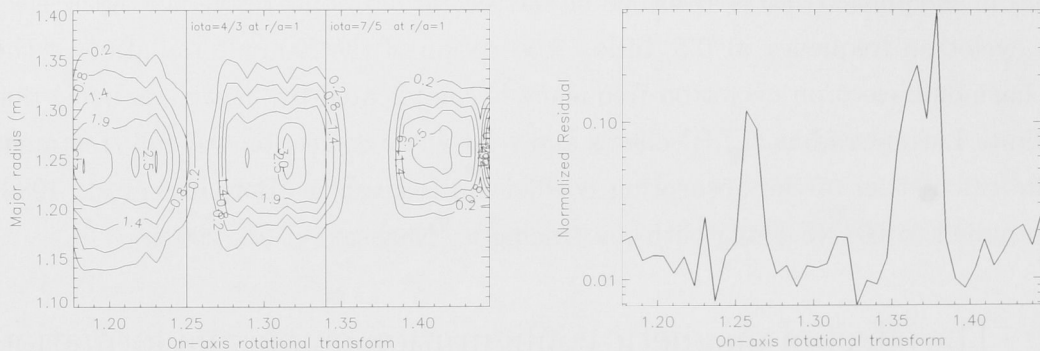


Figure 2.10: Reconstructed density profile as a function of rotational transform and associated errors in the reconstruction

measure of local electron density we tomographically inverted (see section 2.2) the data. Figure 2.10 shows the reconstructed local electron density across the mid-plane in the toroidal position of the interferometer ( $\Phi = 240$  Degrees) as a function of rotational transform. Peak electron density remains relatively constant across the range of rotational transforms studied except for  $\iota = 1.25 \rightarrow 1.27$  and  $\iota = 1.34 \rightarrow 1.38$ . Examination of figure 1.5 shows that the start of these two ranges corresponds to a low order rational surface appearing at the edge of the plasma. Furthermore, when a low order rational surface occurs at the edge of a plasma with low shear plasma formation is suppressed for a wider range of configurations. The exact physical mechanism for edge rationals suppressing plasma formation is unknown however, as discussed in section 2.3.1 the position of the cut off layer for the FW mode effects antenna to plasma coupling, this means a feature (such as a confinement spoiling rational surface) that inhibits plasma formation at the edge may prevent the density reaching the levels required for FW propagation.

## 2.5 The effect of the position of the $\omega = \omega_{ci}$ layer on plasma formation

To understand the effect of the position of the layer where  $\omega = \omega_{ci}$  on plasma formation we again used the scanning interferometer. By taking moments (equation 2.17) of the measured projection of the electron density profile we can extract information about the mean, position and width of the profile.

$$\mu^{(0)} = \sum_i P_i \quad (2.15)$$

$$\mu^{(1)} = \frac{1}{\mu^{(0)}} \sum_i P_i x_i \quad (2.16)$$

$$\mu^{(2)} = \frac{1}{\mu^{(0)}} \sum_i P_i (x_i - \mu^{(1)})^2 \quad (2.17)$$

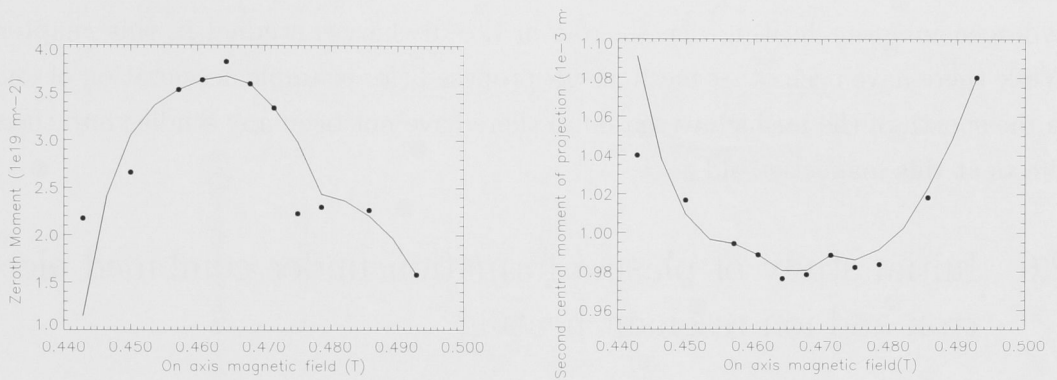


Figure 2.11: The zeroth moment ( $\mu^{(0)}$ ) of the projection of the density profile, which gives a measure of the average electron density, and the second central moment ( $\mu^{(2)}$ ), which gives a measure of the profile width

Figure 2.11 shows the zeroth and second central moment as a function of on-axis magnetic field. The zeroth moment gives a measure of the average electron density in the plane at the toroidal position of the interferometer while the second central moment gives a measure of the profile width.

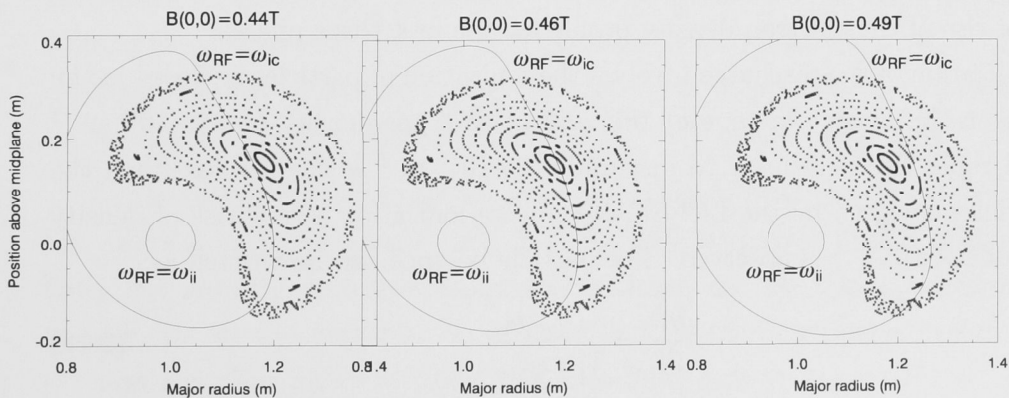


Figure 2.12: Poincaré plots of flux surfaces of the standard configuration ( $\iota_{ax} = 1.12$ ) with contour lines where  $\omega_{ic} = \omega$  and  $\omega_{ii} = \omega$ .

To understand figure 2.11 we need to examine the position of the ion cyclotron layer at different on axis magnetic field strengths. Figure 2.12 shows the position of the ion cyclotron layer and the helium hydrogen ion-ion hybrid layer (assuming that the ratio of ion densities is the same as the ratio of neutral densities). The first feature to note is that the hydrogen helium hybrid resonance is well outside the LCFS so we can assume that it plays no role in plasma formation and heating. The second feature to note from both figures is that the maximum density ( $\mu^{(0)}$ ) and minimum profile width ( $\mu^{(2)}$ ) occurs as the ion cyclotron surface crosses the magnetic axis. This data leads to the conclusion that it is unlikely that simple hydrogen minority heating plays a role in the discharges studied in this chapter. While there have been other mechanisms proposed (for example acceleration of ions in the sheath of the unshielded antenna) there have not been any studies into these effects at this magnetic field.

## 2.6 Initial study of plasma formation under combined electron and ion resonant heating

In an initial study of an electron cyclotron (ECH) heated plasma we injected approximately 100kW of 28 GHz power into an existing ion resonant plasma. We studied the evolution of the electron density profile which was obtained by tomographically reconstructing profiles measured using the scanning interferometer.

Figure 2.13 shows the temporal evolution of the volume integrated electron density (i.e. total number of electrons) through the four phases of the discharge: Initiation of the discharge, the slow ramp up of the electron density during ion resonant heating until an equilibrium is reached, the rapid rise once electron resonant heating is initiated and the decay once heating power is terminated. Figure 2.13 also shows the rate of rise of the electron density profile for the first three phases.

The initiation of the discharge involves the ionisation of particles enclosed in the LCFS. Given the plasma volume of  $1\text{m}^3$  and neutral gas density of  $4.5 \times 10^{17} \text{ m}^{-3}$  the initial rapid rise in density to just under  $2 \times 10^{17} \text{ m}^{-3}$  is slightly less than the total particles enclosed by the LCFS. After initial ionisation a slow rise of density at a rate of  $2 \times 10^{19} \text{ s}^{-1}$  is observed. The particle balance can be written as:

$$\frac{dn_e}{dt} = \frac{G}{V_p} - \frac{n_e}{\tau_{ec}} \quad (2.18)$$

where  $G$  is the ionisation rate which initially we assume is equal to the gas flux across the last closed flux surface ( $A_p/4nv$ ), which has volume  $V_p$  and area  $A_p$ ,

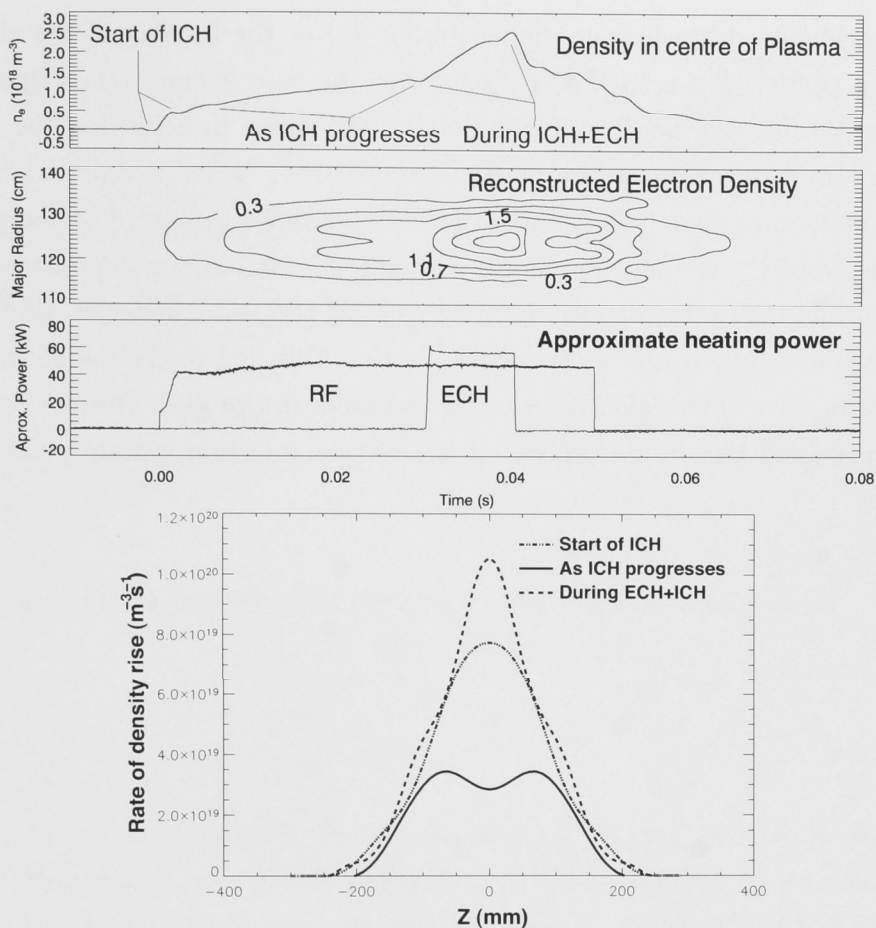


Figure 2.13: The top panel shows a line and contour plot of the evolution of the local electron density as well as the approximate heating power applied during discharge 44508. The bottom panel shows profiles, taken through the centre of the plasma, of the rate of rise of the electron density.

and where  $\tau_{ec}$  is the electron particle confinement time. Using the observed  $dn_e/dt$  (during the slow density rise during ICH) and equation 2.18 we calculate the particle confinement time to be 0.3ms which is close to the 0.4ms L-mode confinement time for H-1NF reported in [Shats et al., 1996] at lower magnetic fields.

At the end of the ion cyclotron phase equation 2.18 reaches an equilibrium until the electron cyclotron phase (which is the dashed narrow profile in figure 2.13). Once the electron cyclotron heating is initiated the plasma experiences a rapid density rise for the duration of the phase. Using the new rate of rise of  $3.3 \times 10^{19} \text{ s}^{-1}$  and equation 2.18 we obtain a new confinement time of 0.45ms. There are two possible explanations for the change in  $\tau_{ec}$ : Our assumption of 100% ionisation is incorrect (the helium line ratio diagnostic was not yet installed at the time of

these experiments so we had no diagnostic for  $T_e$ ) or the heating of the electrons suppressed particle losses in H-1NF. Whatever the case it can be concluded that using a static fill, thermal fluxes will lead to difficulties in achieving the density control required to maximise the plasma temperature. What is required is a fuel delivery mechanism that delivers a controlled dose of fuel directly to the plasma. As the electron density and temperature profile determines the deposition profile of injected fuel the design of such a device can not proceed without measurements of the electron temperature of the target plasma. This led to the installation of a diagnostic beam to determine the electron temperature profile. Results from this diagnostic guided the design process of a direction injection system presented in chapter 5.

# Helium line ratios for electron temperature measurements

A man with a new idea is a crank until the idea succeeds

– *Mark Twain*

To calculate the fuelling profile for any proposed gas injection system a knowledge of electron density and temperature profile is required. In section 2.1.2 we introduced a system for measuring the density profile which is in use on the H-1NF heliac. However, at the time the experiments in chapter 2 were carried out, we did not have a system for measuring the electron temperature profile,  $T_e(r, t)$ . This chapter discusses the theory and installation of helium line ratio diagnostic which is based on a diagnostic helium molecular beam.

Methods for measuring  $T_e$  include probes, spectroscopy (both visible and x-ray), electron cyclotron emission (ECE) and Thompson scattering. When deciding on a  $T_e$  diagnostic we had to consider the expected range of  $T_e$  in H-1NF as well as the diagnostic access to the plasma and other practicalities. The high heat flux makes probe measurements difficult for all but the edge region of the plasma. The H-1NF plasma is not optically thick enough for ECE, and the electron density is too low for Thompson scattering, leaving spectroscopic techniques as an option. One spectroscopic technique is to monitor two spectral lines of neutral helium, one involving a triplet and one involving a singlet upper state. While the emissivity of the individual transitions has a dependence on both electron temperature and density the ratio of the two emissivities responds pre-dominantly to temperature variations.

$$\frac{dn(i)}{dt} = - \left[ \sum_{j \neq i} C(i, j) n_e + \sum_{j < i} A(i, j) + S(i) n_e \right] n(i) - \sum_{j \neq i} \left[ \{C(j, i) n_e + A(j, i)\} n(j) + \{\alpha(i) n_e + \beta(i) + \beta_d(i)\} n_i n_e \right]$$

*Decreasing level population*

- Collisional de-excitation*
- Spontaneous emission*
- Ionisation*

*Increasing level population*

- Collisional excitation*
- Spontaneous emission*
- Recombination*

Figure 3.1: The rate equation for the population (number density) of a state  $i$

### 3.1 The collisional radiative model

The rate of increase of the density of helium atoms in a particular excited state,  $i$ , can be calculated by using the equation shown in figure 3.1 [Fujimoto, 1979, Goto, 2003] where  $n(i)$  is the density of helium atoms in the quantum state  $i$ ,  $C(i, j)$  is the rate coefficient for collisional excitation from state  $i$  to  $j$ ,  $A(i, j)$  is the probability of spontaneous transition from state  $i$  to  $j$ ,  $S(i)$  the rate coefficient for ionisation from state  $i$  and  $\alpha(i), \beta(i), \beta_d(i)$  are the rate coefficients for three body, radiative and dielectric recombination, respectively. For a plasma in quasi steady-state we can take the left hand side of the equation to be zero yielding a set of simultaneous equations describing the population density of each state.

The collisional radiative model (CRM) solves the equations shown in figure 3.1 for the population densities up to a principal quantum number (left hand side of figure 3.2, denoted as  $n$ ) of 7. Between  $n=8$  and  $n=10$  triplet and singlet states are grouped separately and  $n=11$  to  $n=26$  all states are grouped into a state representing all states within that quantum number.

Using the calculated populations and the state to state transition probabilities,  $A(j, i)$ , the rate of transition, which is directly proportional to the line emissivity, can be calculated. The effect of wave function mixing (mixing of wave functions from adjacent triplet and singlet states due to Zeeman splitting) at H-1NF magnetic fields is small [Goto, 2003] and can be neglected. We also neglect radiation trapping as, according to [Sasaki et al., 1996] this can be ignored when the column density of helium atoms,  $n_{He}L$ , is below  $10^{19} \text{cm}^{-2}$ .

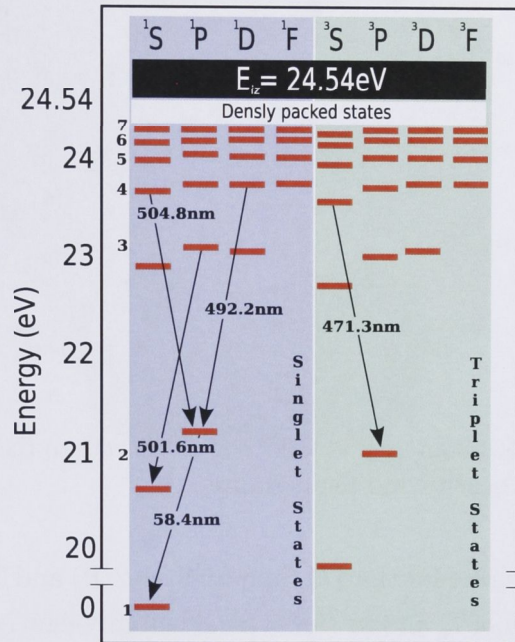


Figure 3.2: Energy levels for the neutral helium atom. Principal quantum number is shown on the left. Energy values where the collisional radiative model groups states are shown in white

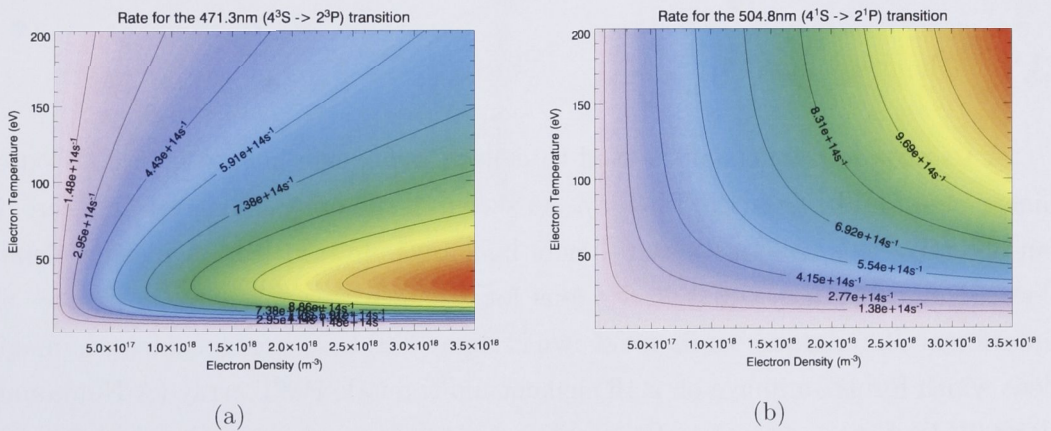


Figure 3.3: The CRM calculated rate of the 471.3nm ( $4^3S \rightarrow 2^3P$ ) and 504.8nm ( $4^1S \rightarrow 2^1P$ ) transitions as a function of electron temperature and density

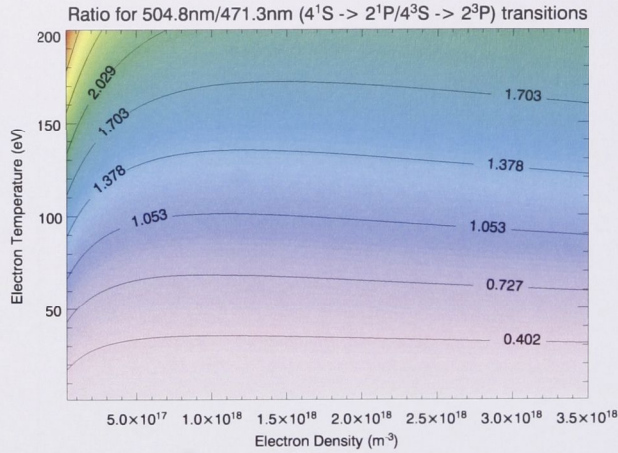


Figure 3.4: Ratio of the 504.8nm ( $4^1S \rightarrow 2^1P$ ) transition rate to the 471.3nm ( $4^3S \rightarrow 2^3P$ ) as a function of electron density and temperature

Figure 3.3 shows the rate for the 471.3nm ( $4^3S \rightarrow 2^3P$ ) and 504.8nm ( $4^1S \rightarrow 2^1P$ ) transitions as a function of  $T_e$  and  $n_e$  (for typical helium beam conditions, see section 3.3). While the 504.8nm emission rate scales with  $n_e T_e$ , due to the complexities of the excitation route required to populate the  $4^3S$  state, the 471.3nm emission rate falls with increasing temperature after 20eV. This results in the ratio of the 504.8nm to 471.3nm emissivities (as shown in figure 3.4) varying monotonically with temperature and being largely independent of  $n_e$ . Therefore the measurement of the emission intensities of the transitions at 504.8nm and 471.3nm can be used to infer the electron temperature.

## 3.2 Optical system

A telescope arrangement is used to collect and image helium emissions onto a linear photo multiplier (PMT) array. As shown in the optical diagram in figure 3.6, an objective lens collimates and directs light rays emitted from a plasma element located at a distance equal to the lens focal length through a beam splitter and interference filters (passbands are shown in figure 3.9) to a short focal length imaging lens which forms an image on a 16 element multi anode PMT array (A Hamamatsu R5900U-04-L16). The size of the object (at the focal plane of the objective lens) that can be imaged,  $S_{Obj}$ , by a detector of size  $S_{Det}$  given by

$$S_{Obj} = M S_{Det} = \frac{f_O}{f_I} S_{Det} \quad (3.1)$$



Figure 3.5: Collection optics for the helium line ratio diagnostic.

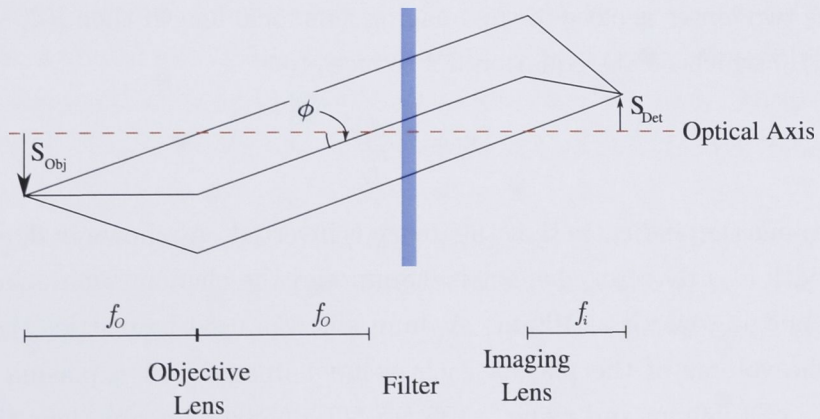


Figure 3.6: An optical diagram for a telescope imaging an object located at the objective focal length.

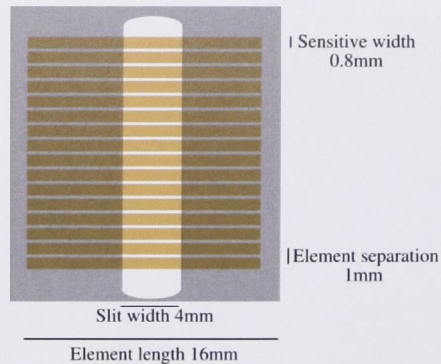


Figure 3.7: Schematic of the 16 channel PMT array

where  $f_O$  and  $f_I$  are the focal lengths of the objective and imaging lenses and  $M$  is the magnification of the system.

However, in the system implemented on the H-1NF Heliac (shown in figure 3.5), the mid-plane of the plasma is 1650mm from the 1400mm focal length objective lens. A system comprising an objective and imaging lens separated by a distance  $d_s$  with an object (in our case the plasma mid-plane) to objective lens distance of  $d_p$  will have a magnification given by

$$M = \frac{(d_s - f_I)(d_p - f_O) - d_p f_O}{f_O f_I} \quad (3.2)$$

which in the case  $d_p = f_O$  reduces to the form in equation 3.1. If the objective to object distance is close to the focal length of the objective and the separation between the two lenses is close to the imaging lens focal length then  $|(d_s - f_I)(d_p - f_O)| \ll |d_p f_O|$  which means equation 3.2 reduces to

$$M \approx -\frac{d_p}{f_I} \quad (3.3)$$

where the minus sign indicates that the image is inverted. As shown in figure 3.7 the sensitive width of a detector element is 0.8mm and the element separation is 1mm for a total imaging width of 16mm. A 4mm slit was used to restrict the toroidal extent of the volume of the plasma each element images. At a plasma objective distance,  $d_p$ , of 1650mm and using a 105mm f/2.5 Nikkor imaging lens the system has a magnification of 15.7. This means that our detector array images a strip 25cm long (radially across the plasma) and 6cm wide and has a (calculated) spatial resolution of 1.6cm.

It is imperative that both detector arrays view the same location in the plasma. To confirm this is the case and to verify our calculated magnification we measured

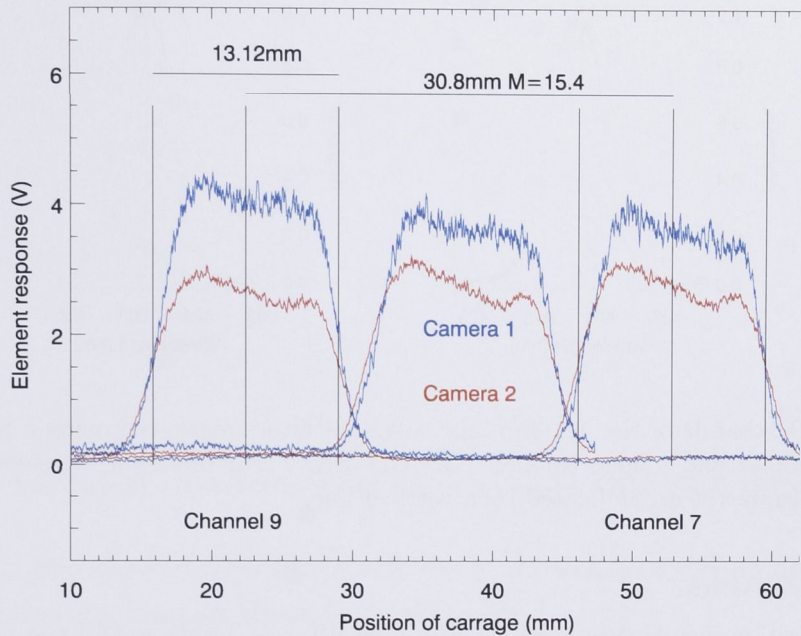


Figure 3.8: Spatial calibration of the HLR optics showing good registration and focus.

the spatial response of the imaging system. We used a tungsten quartz-halogen lamp with a 1mm slit as a localised light source and scanned this across the field of view of the optics using a motorised translation stage at a distance equivalent to the location of the plasma midplane. Figure 3.8 shows the response of channels 7 and 9 for both cameras as a function of carriage position and, as can be seen, the registration is very good. The distance between the channels (two channels apart) represents a magnification of 15.4 which agrees very well with our calculated magnification of 15.7. The full width at half maximum (fwhm) for the individual channels is 13.12mm, which gives a back-projected channel width of 0.83mm (without deconvolving the slit width) which is slightly wider but close to the 0.8mm published sensitive width of the channel. These results show that the system is well focused and registered and that our approximations in deriving equation 3.3 were valid.

### 3.2.1 Optical calibration

To obtain a reliable measurement of the emissivity ratio it is necessary to relatively calibrate the sensitivities of the corresponding channels in the two cameras. There are three factors which affect relative sensitivities: the dependence of the interference filter transmission on angle, optical throughput and differences in the

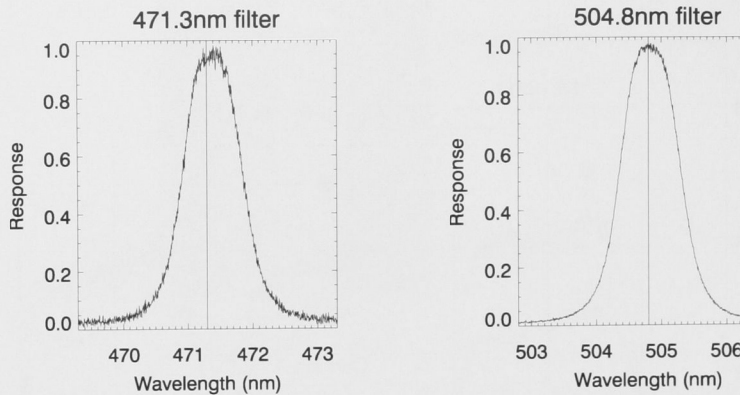


Figure 3.9: Passbands of the 471.3nm and 504.8nm filters measured using a high resolution spectrometer and a 2048 channel 1D CCD array. The emission wavelengths of the transitions of interest are indicated by a vertical line.

detector sensitivities.

A ray that passes through an interference filter at angle  $\phi$  will see a passband shifted according to

$$\lambda = \lambda_0 \sqrt{1 - (n_0/n_{eff})^2 \sin^2(\phi)} \quad (3.4)$$

where  $n_0$  is the refractive index of the background medium (air),  $\lambda_0$  is the centre wavelength at normal incidence and  $n_{eff}$  is the effective refractive index of the filter.

Taking the approximation that the object is at the objective focal length the central ray angles,  $\phi(i)$ , as a function of channel number  $i$ , (numbered from the bottom 1-16) are given by

$$\phi(i) = \arctan\left(\frac{|(i-1)-7.5|M}{f_O}\right) \quad (3.5)$$

$$= \arctan\left(\frac{|(i-1)-7.5|}{f_I}\right) \quad (3.6)$$

where the focal lengths ( $f_O$  and  $f_I$ ) are in millimetres.

There was no documented  $n_{eff}$  for our filters so to measure it (as well as confirming our filter obeyed equation 3.4) we measured the centre of mass (which is a good approximation to the peak position) of the passband at various angles of incidence using a rotation stage, collimated white light source and grating spectrometer.

Figure 3.10 shows the centre of mass of the passband of the 471.3nm filter (passband shown in figure 3.9) as a function of the angle of incidence of the light on the filter. The fitted curve has the form of equation 3.4 with a  $n_{eff}$  of 1.7. Assuming that the refractive indices of the two filters (504.1nm and 471.3nm) are the same

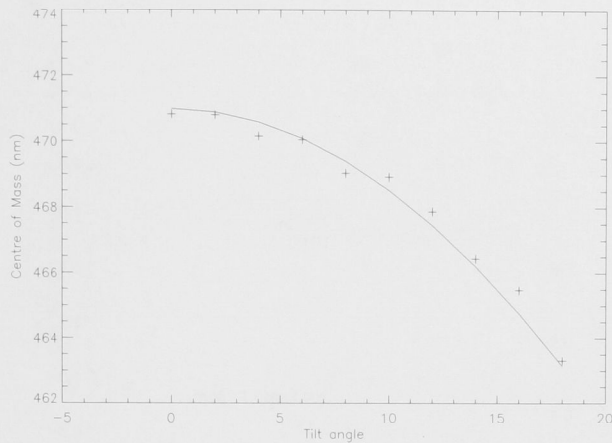


Figure 3.10: Angular response of the 471.3nm interference filter

we can calculate the variation of the relative transmission of the atomic line as a function of detector channel which is shown in figure 3.11.

To verify the validity of our assumptions in deriving figure 3.11 we took a direct measurement of the transmission of the 504.8nm filter for a range of angles. These values are over-plotted and agree well with the calculated transmissions. Because of higher angles of incidence, transmissions at  $\lambda_0$  for outer channels is slightly reduced. However, as shown in figure 3.11 the ratio (from which the measurement of  $T_e$  is derived) remains relatively constant across all 16 channels of the detector.

To calibrate for both optical throughput and differing detector sensitivities we illuminate the system using a white card illuminated by a tungsten quartz-halogen lamp to approximate a spatially uniform source. The spectrum of the light reflected off the white card (figure 3.12) was measured using a grating spectrometer (SM-232) which was calibrated (to quantify sensitivity as a function of wavelength) using a blackbody oven of known temperature. The calibration of the two cameras was performed in situ on H-1NF with the magnetic coil-set energised.

Figure 3.13 shows the response of the system to the white light source (calibrated for spectral sensitivity using a black body oven). Even though both cameras use nominally identical detector arrays camera 1 is more sensitive than camera 2 by a factor of 2. This is due to the magnetic shielding being less effective for camera 2 (which is closer to the top outer vertical field coil).

By applying the calibrations shown in figure 3.13 and figure 3.11 (which is only a minor correction) the true emissivity of the 471.3nm ( $4^3S \rightarrow 2^3P$ ) and 504.8nm ( $4^1S \rightarrow 2^1P$ ) transitions can be obtained to within a constant common to both units. The ratio of the two emissivities can then deliver the electron temperature.

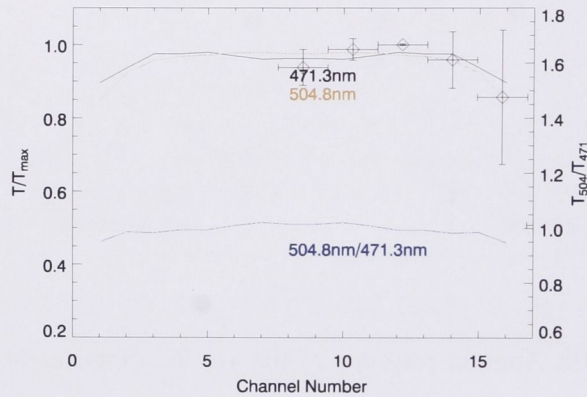


Figure 3.11: transmission through the 504 and 471nm filters as a function of channel number and the ratio of the two transmissions. A direct measurement of the transmission through the 504nm filter is over-plotted (diamonds).

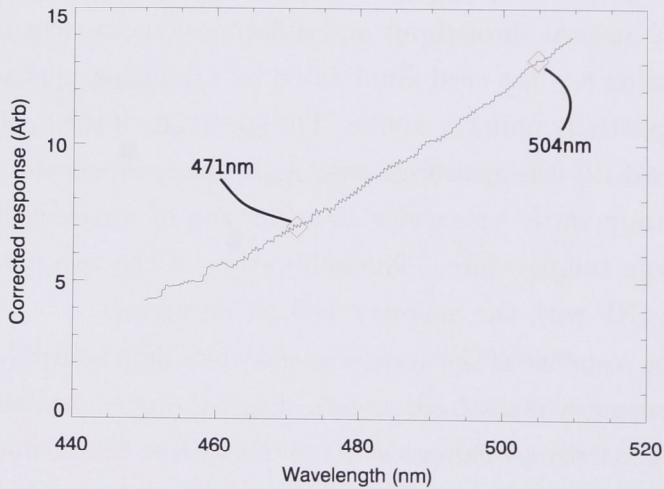


Figure 3.12: The spectrum of the light emitted by the calibration lamp (reflected off the white card) as recorded by the SM-232 spectrometer, and corrected for the spectrometer response. The centre wavelengths of the passbands of the filters used have been highlighted.

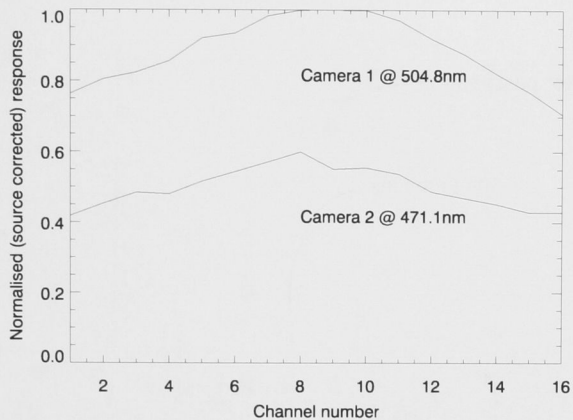


Figure 3.13: Response of the two cameras to uniform illumination, corrected for the spectrum of the source. Even though the same model of detector was used in both the cameras, camera 2 is less sensitive than camera 1. This is because camera 2 is closer to the vertical field coil of the H-1NF device and is strongly affected by the magnetic field (despite attempts to shield it).

### 3.3 Helium beam diagnostic

Measurement of  $T_e$  using helium line ratios on H-1NF is complicated by the presence of radiation emitted by impurity atoms and ions in the spectral passband of the filters that admit the helium transitions. Figure 3.14 presents emission spectra from the H-1NF plasma in the region of the 504.8nm helium line showing significant impurity lines in the passband.

This problem can be overcome by injecting a prompt pulse of helium gas into the plasma. Assuming that the gas does not significantly perturb the plasma conditions ( $n_e, T_e$ ) any change in light through the filter passbands (each of which encompasses only one helium spectral line) can be associated with the helium pulse.

By using a gas pulse which is spatially limited we can also perform a localised measurement of emissivity, removing line integral effects and negating the need for numerical inversions to obtain the  $T_e$  profile.

The helium beam diagnostic (HBD) installed on the H-1NF heliac was designed and characterised as part of Daniel Andruczyk's PhD Thesis [Andruczyk, 2005]. Some details are reproduced here for completeness. The HBD uses a nozzle skimmer arrangement similar to that used in the helium beam in use on the TJ-II heliac [Diez-Rojo et al., 1997]. The nozzle used in the HDB uses a Parker solenoid valve which seals against an orifice of a diameter of 1mm. The nozzle is then mounted on guide posts which allows the nozzle skimmer separation to be varied. We did

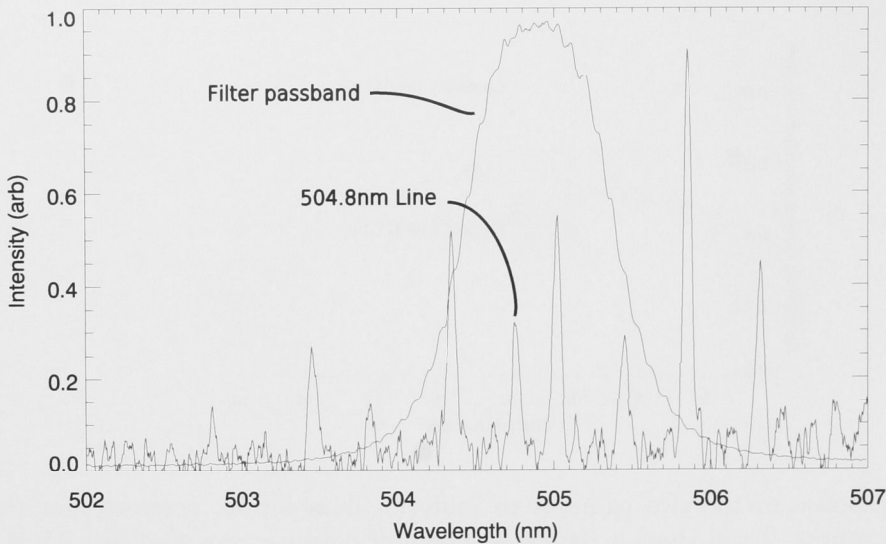


Figure 3.14: Emission spectra from the H-1NF plasma in the region of the 504.8nm He line showing various impurity lines falling within the interference filter passband

not do an in-depth study of the affect of varying the nozzle skimmer distance. We decided to use a value commonly used in [Andruczyk, 2005] of 31mm. The skimmer, which was purchased from Beam Dynamics, has a 1mm diameter entrance orifice. The nozzle skimmer area ratio is not ideal for minimising the gas shielding affects discussed in [Beijerinck & Verster, 1981] but was chosen to optimise the beam width in the plasma. Helium particles within the beam are reported to have a velocity of 1750m/s. According to [Fowler et al., 1964] the lifetimes for the  $4^3S$  and  $4^1S$  states (upper states of the 471 and 504nm transitions) are 63.8ns and 90ns respectively. In this time beam neutrals travel 0.15mm which is much less than the channel spacing (as described in section 3.2 of 16mm). So we can assume that emissivities measured at a spatial position are due to local gas and plasma conditions only.

Figure 3.15 shows the HBD in relation to the collection optics. The nozzle is enclosed in a re-entrant stainless steel tube that is mounted to a port on the vacuum vessel. The skimmer is mounted on the end of the tube and is aligned to the nozzle using a helium neon laser. The approximate distance from the skimmer to the centre of the plasma is 23cm. At this distance the density of helium in the centre of the beam for a (typical) source pressure of 600kPa is reported to be  $\sim 1 \times 10^{19} \text{m}^{-3}$  with a beam width of  $\sim 15\text{mm}$ . This gives a particle injection rate of  $\sim 3.1 \times 10^{18} \text{s}^{-1}$  which means during typical  $180\mu\text{s}$  pulse  $\sim 5.6 \times 10^{14}$  particles are injected. The energy required to ionise this number of particles is 2mJ which is very small compared to a typical stored electron energy ( $\bar{n}_e = 1 \times 10^{18} \text{m}^{-3}$ ,  $\bar{T}_e = 100\text{eV}$ )

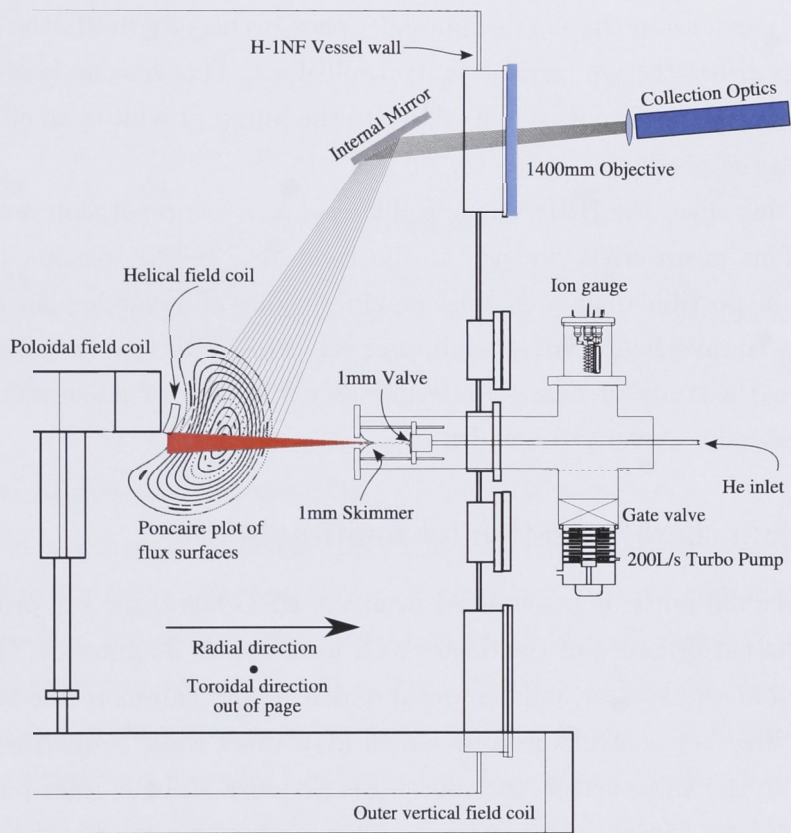


Figure 3.15: A diagram of the HLR  $T_e$  diagnostic system showing a Poincaré plot (at standard configuration) of the H-1NF flux surfaces with the viewing geometry of the optical system and launch geometry of the helium beam

of  $\sim 24\text{J}$  therefore we can assume that the global perturbation on the plasma is small. And since (see section 5.4) the mean free path for electrons passing through the beam is expected to be greater than  $1\text{m}$  we can assume that the beam is ionised uniformly and there is no toroidally localised cooling of the plasma.

To limit particles initially rejected by the skimmer from later diffusing through the orifice of the skimmer into the H-1NF vessel the volume of the re-entrant tube is pumped using a turbo molecular pump ( $200\text{L/s}$ ) and the pressure inside the volume is monitored by an ion gauge. However, as shown in [D. Andruczyk et al., 2006] the build up of particles in the nozzle skimmer space eventually limits the flow through the skimmer orifice through neutral-neutral collisions. This gas can leak out through the skimmer orifice before it is able to diffuse to the pump providing an effusive source of helium to the plasma.

Due to this effect the HBD was initially used as a low repetition rate diagnostic ( $\sim 1\text{Hz}$ ). This means that during the life time of a H-1NF plasma ( $>100\text{ms}$ ) it would only be possible to fire one pulse making studies of dynamic plasma behaviour impossible. To investigate the possibility of rapid ( $\sim 500\text{Hz}$ ) multi-pulse operations we performed a study of beam properties as a function of pulse number, source pressure and valve driver pulse width.

### 3.3.1 Beam characterisation for multi-pulse use

An individual pulse of gas emitted from the HBD has three key properties pertinent to the performance of the device as a localised  $T_e$  diagnostic. These are the brightness and the spatial and temporal width of the emission due to the pulse. There are three key control variables which may affect these properties: The pulse width sent to the valve driver, the source gas pressure and the inter-pulse timing.

To investigate the possibility of using the gas injector to obtain time resolved  $T_e$  profiles we performed a number of experiments aimed at characterising the HBD performance as a function of the control parameters. The data was taken by injecting the beam into a ECH initiated and heated hydrogen plasma. An ECH plasma was chosen as electron temperatures are high enough that even low injection rates (particles per second exiting the device) give rise to detectable signal levels above the background (impurity) radiation.

To allow a measurement of the spatial extent of the beam emission in the toroidal direction the standard optical system described in section 3.2 was modified by rotating camera 1 by  $90$  degrees and exchanging the  $105\text{mm}$  imaging lens for a  $200\text{mm}$   $f/4$  lens. Using equation 3.3 this gives a magnification of  $8.25$  which means the

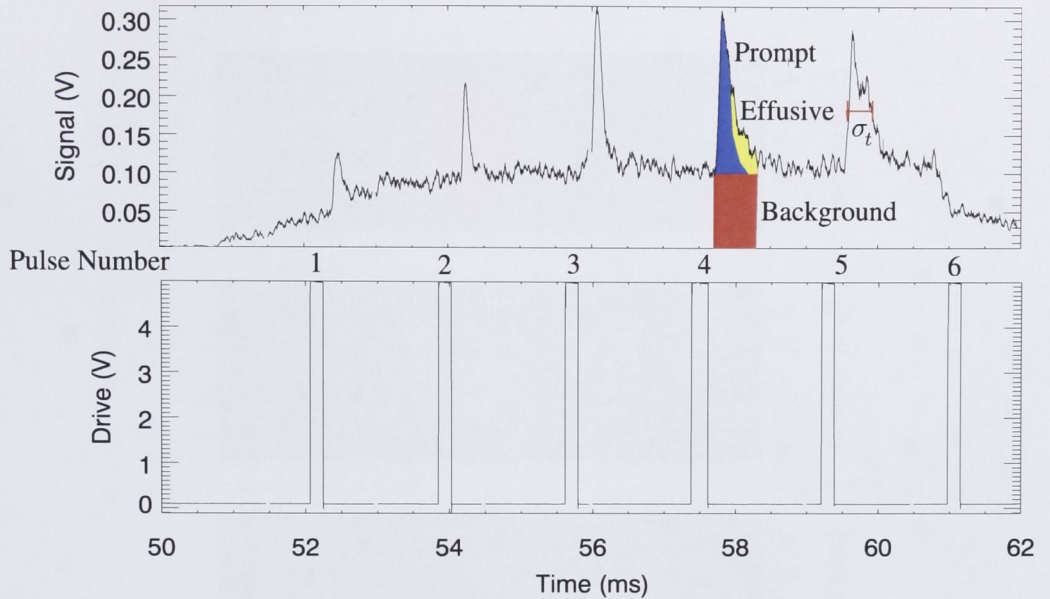


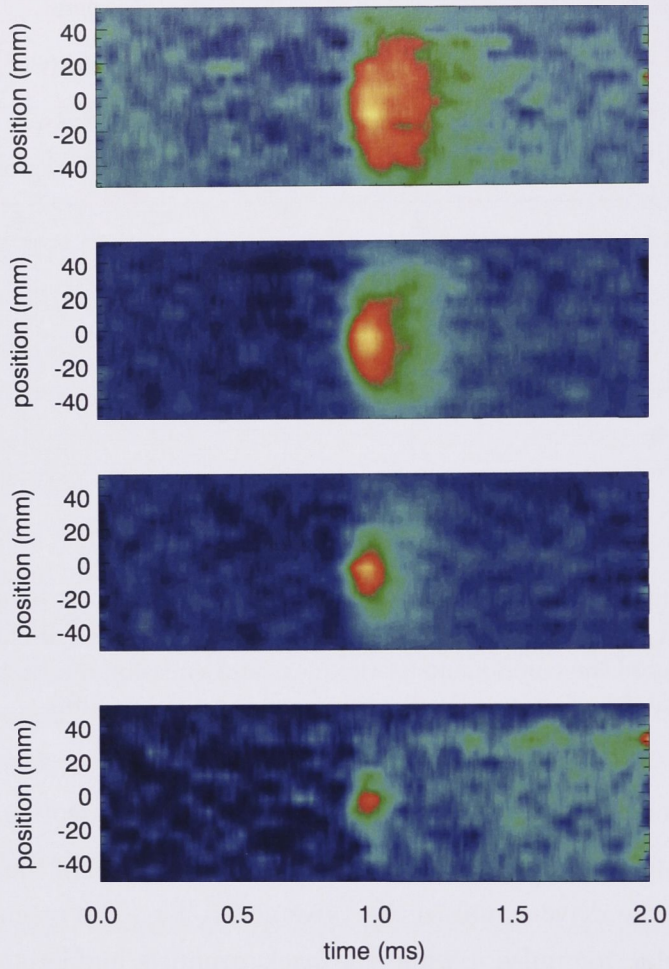
Figure 3.16: Light signals for the central channel of the toroidal imaging array during multi-pulse helium beam injection into an ECH heated plasma (discharge 61031). The time series highlights the components of the measured emission due to the prompt (blue), effusive (yellow) and background (red) components of the injection.

detector array images a strip 13.2cm long in the toroidal direction.

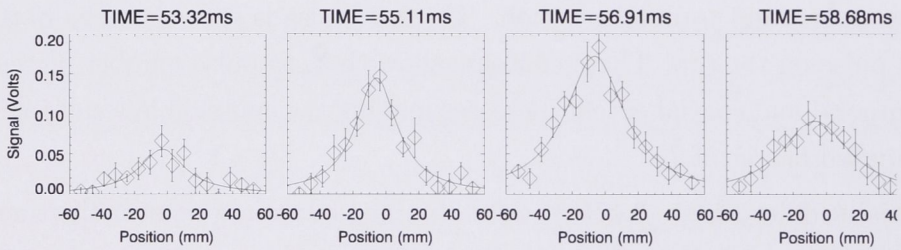
Figure 3.16 shows typical signals from the central channel of the toroidal imaging array as well as the drive signal to the valve controller. The prompt component is highlighted in blue for pulse 4 while the background is highlighted in red and an estimate of the effusive component in yellow. Figure 3.17 shows contour plots of the 471nm emission (background subtracted) as a function of time (relative to the beam trigger pulse) and toroidal position. The 2nd pulse is shown on the bottom and the 5th pulse on the top. These contours show that, as pulse number increases both the temporal and spatial extent increases making the emission less suitable for a localised measurement of  $T_e$ .

The spatial profiles (figure 3.17(b)) were obtained by averaging over the time of the pulse for each spatial channel. A Lorentzian curve was then fitted to the profile (chosen for the simple reason that it presented the best fit) to obtain the intensity ( $I$ ), position ( $x_0$ ) and full width at half maximum ( $\sigma_s$ ) of the profile.

Figure 3.18 shows the key properties of the background subtracted emission as a function of the control parameters of pulse number, source pressure and driver pulse width. The inter-pulse spacing was 1.8ms (556Hz). Scans where the driver pulse length was varied were carried out at a constant source pressure of 500kPa

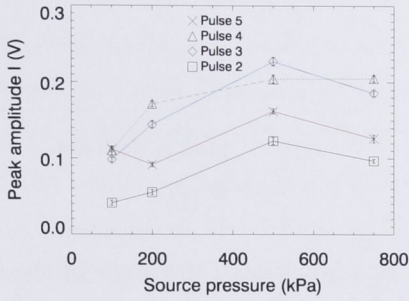


(a)

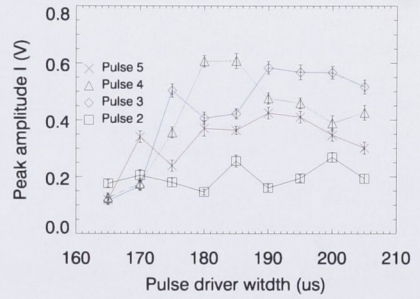


(b)

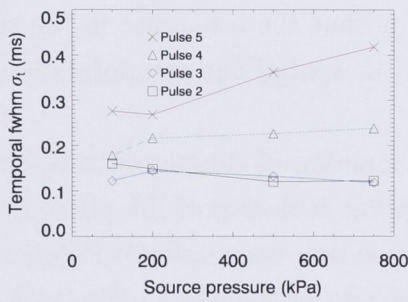
Figure 3.17: (a) Contour plots of the light collected by the toroidal imaging array as a function of time (relative to the pulse trigger) and position. (b) Profile data with fitted Lorentzians



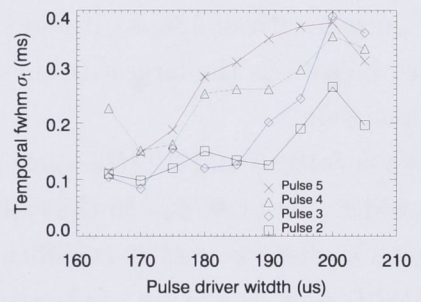
(a)



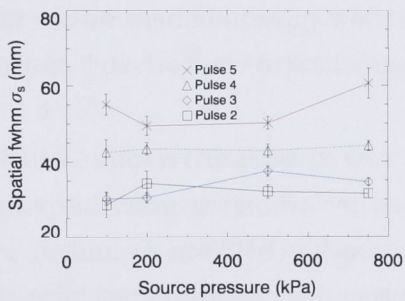
(b)



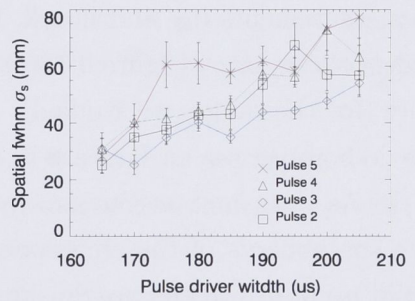
(c)



(d)



(e)



(f)

Figure 3.18: Intensity, spatial and temporal width of the light pulses produced using the HDB as a function of source pressure, pulse length and pulse number

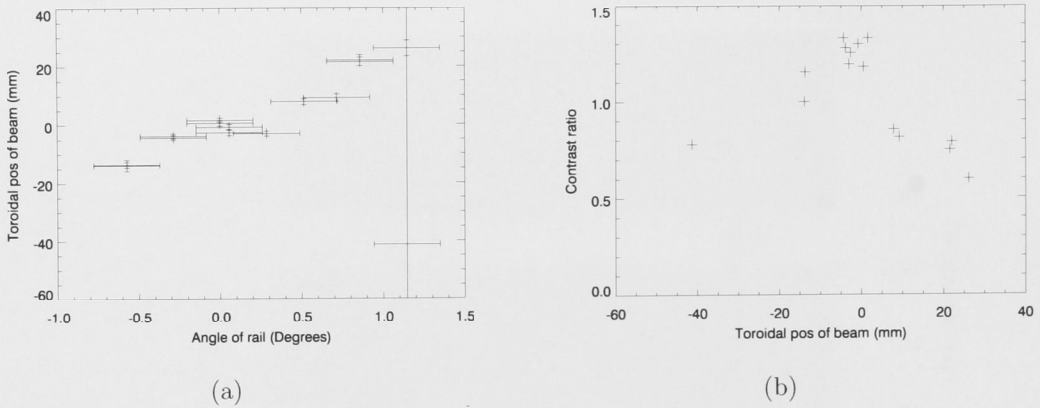


Figure 3.19: (a) Position of the fitted Lorentzian as a function of the angle of the rail. (b) Ratio between the pulse amplitude (minus the background) and the background level.

while scans where the source pressure was varied were carried out with a constant driver pulse length of  $180\mu\text{s}$ . It can be seen is that the last pulse in the sequence (the 5th pulse) has the largest fwhm of both the spatial and temporal distribution of the emission.

Figures 3.18(a) and 3.18(b) show  $I$  as a function of source pressure and pulse driver width, however, due to the rapid temporal evolution of the plasmas used as a target for these studies it is difficult to draw any conclusions. Figures 3.18(c) and 3.18(d) show the fwhm of the temporal extent of the beam emission ( $\sigma_t$ , illustrated on pulse 5 in figure 3.16), and show a clear increase with source pressure for the higher pulse numbers. Also, in agreement with the spatially resolved fast ion gauge measurements in [Andruczyk, 2005], at low pulse numbers we see no strong dependence of  $\sigma_t$  or  $\sigma_s$  (figure 3.18(c) and figure 3.18(e) respectively) on the source pressure (for the ranges we studied).

We do however see an increase in both  $\sigma_t$  and  $\sigma_s$  with driver pulse width (figure 3.18(f)). As both measurements are obtained by averaging over the prompt and effusive components of the emission the relationship between  $\sigma_t$  and  $\sigma_s$  is due to the build up of gas in the nozzle skimmer space. Our measurement of  $\sigma_s$  (using a early pulse, pulse 2 which is very similar to a single pulse result) was 30mm and was broader than the fast ion gauge measurement (from [Andruczyk, 2005] at the same distance from the skimmer) of 15mm. Again, this may be due to emission from the effusive component of the beam. After obtaining these results it was decided to use a pulse driver width of  $185\mu\text{s}$  and a source pressure of 600kPa which would allow at least 5 pulses until  $\sigma_s$  approaches the projected toroidal size of the PMT array slits onto the plasma of 63mm.

To ensure that the optics were correctly viewing the beam emission we varied the angle between the optical rail (shown in figure 3.5) and the vertical optical table upon which it was mounted. Figure 3.19(a) shows the variation of  $x_0$  in the toroidal direction as a function of rail angle. This figure shows that when the rail is parallel to the table the profile is in the centre of the field of view of the camera. Figure 3.19(b) shows the contrast ratio ( $R_c$ ) between the background emission and pulse emissions (with the background subtracted). This measurement was taken from the central channel of the radial viewing array (camera 2). As the angle is changed the beam path falls out of the projected area of the slits and only the dull effusive component of the beam is detected, reducing  $R_c$ . Therefore when  $R_c$  is maximised the beam is being fully imaged by the slit. Figure 3.19(b) shows that  $R_c$  is maximum when the rail is normal (or near to normal) to the table, showing that the imaging optics are well aligned to the HBD.

### 3.4 Calculation of $T_e$

Raw signals from the HLR system were digitised using CAMAC transient recorders and saved to the MDS data base for post shot analysis. Figure 3.20 shows a contour plot of the raw data collected by one of the cameras as a function of time and major radius. The pulses in the light signal are due to HBD injection while the background signal is due to emission from the helium component of the static fill and impurity emitters. One interesting feature of Figure 3.20 is that, towards the end of the discharge, the peak in background light is on the inboard side of the plasma. This may be due to impurities liberated from the helical winding surface (see figure 3.15).

Figure 3.22 shows the process for calibration of the data and extraction of the emissivities plus calculation of electron temperatures. Once the raw data has been calibrated (see section 3.2.1) and any instrumental DC offset removed the signals are partitioned into time segments that contain only one pulse (figure 3.21). The background is then calculated from an average of the pre and post pulse levels ( $S_{pre}$  and  $S_{post}$ ) and subtracted. The emissivity of the pulse is then determined by taking a windowed average (of width  $t_w$ , typically  $300\mu s$ ) over the peak of the pulse. As shown on figure 3.21 the position of the window is varied as a function of major radius ( $r_M$ ) to take into account the propagation of the beam at an implied velocity of  $1600\text{m/s}$  (close to the value reported in [Andruczyk, 2005] of  $1750\text{m/s}$ ). Mathematically the emissivity as a function of time (or pulse number),  $t_0$ , and  $r_M$

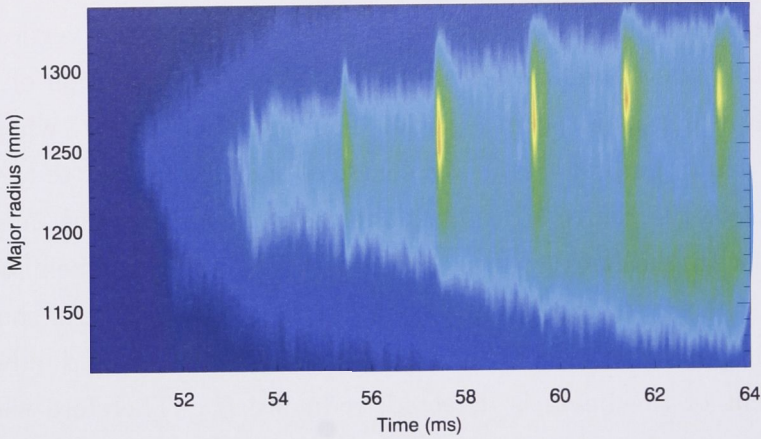


Figure 3.20: Raw light signals collected through the 504nm filter during HBD injection into an ECH heated plasma (discharge 61031).

is given by

$$I_{\lambda}(r_M, t_0) = \langle S(r_M, t) - (S_{pre} + S_{post})/2.0 \rangle. \quad (3.7)$$

The angled brackets denote a time average between the upper and lower bounds of the time window,  $U$  and  $L$ , given by

$$U = (t_0 + t_s(r_M)) + t_w/2 \quad (3.8)$$

$$L = (t_0 + t_s(r_M)) - t_w/2 \quad (3.9)$$

where  $t_0$  is the time the gas pulse was fired,  $t_s(r_M)$  is the offset between  $t_0$  and the time of the maximum in light signal due to the pulse. We have found that, for most plasma and beam conditions  $t_s(r_M)$  remains constant from shot to shot and pulse to pulse.

Using the CRM the ratios for a range of electron temperatures and densities ( $R_c(n_e, t_e)$ , figure 3.4) are pre-computed and stored. The observed ratio is then used, along with a  $n_e$  profile (either from the scanning interferometer or a parabolic profile scaled to the average density as measured using the 2mm system) in the lookup of the electron temperature from  $R_c(n_e, t_e)$ .

### 3.4.1 Uncertainties

As can be seen in figure 3.21 at some positions in the plasma the signal levels are very low. This, in addition to systematic errors (such as errors in the calibration), will affect the accuracy of the  $T_e$  measurement.

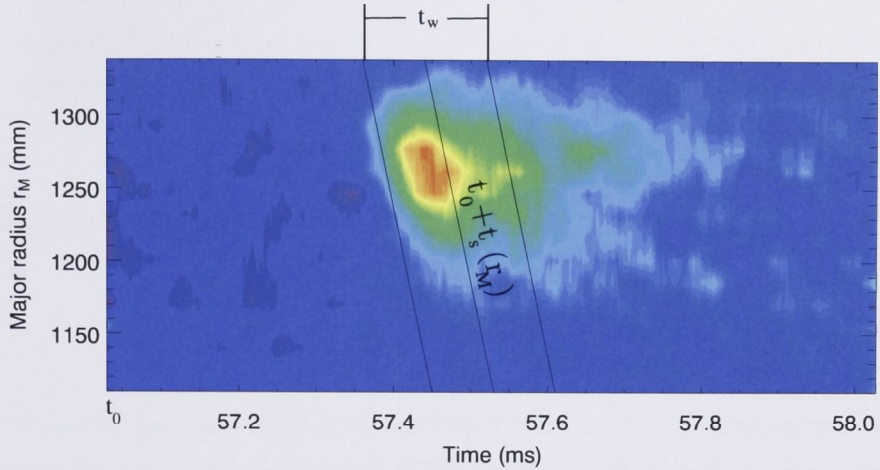


Figure 3.21: An isolated HBD pulse showing the averaging window

Signals recorded using a PMT can be described by Poisson noise statistics. From the standard deviation of the Poisson distribution the signal-to-noise ratio of the signal,  $s/\sigma$ , is given by

$$s/\sigma = \sqrt{N} \quad (3.10)$$

$$(3.11)$$

where  $\sigma$  is the standard deviation over the averaging window,  $N$  is the number of photons (or events) and  $s$  is the mean signal which is given by  $s = kN$ . Assuming that the pre-pulse background signal,  $b$ , is relatively constant we can determine the signal-to-noise ratio and hence the constant of proportionality,  $k$ , between the background signal and the number of photons received during the background period, as

$$k = \frac{\sigma_b^2}{b} \quad (3.12)$$

and since this proportionality constant is the same for the background and pulse signals we can calculate the signal-to-noise ratio over the pulse ( $p/\sigma_p$ ) as

$$p/\sigma_p = \sqrt{p/k} \quad (3.13)$$

$$= \frac{\sqrt{b}}{\sigma_b} \sqrt{p} \quad (3.14)$$

where  $p$  is the average signal over the pulse and  $\sigma_b$  is the standard deviation of the background signal ( $b = \langle (S_{pre} + S_{post})/2 \rangle$ ). The background signal was boxcar

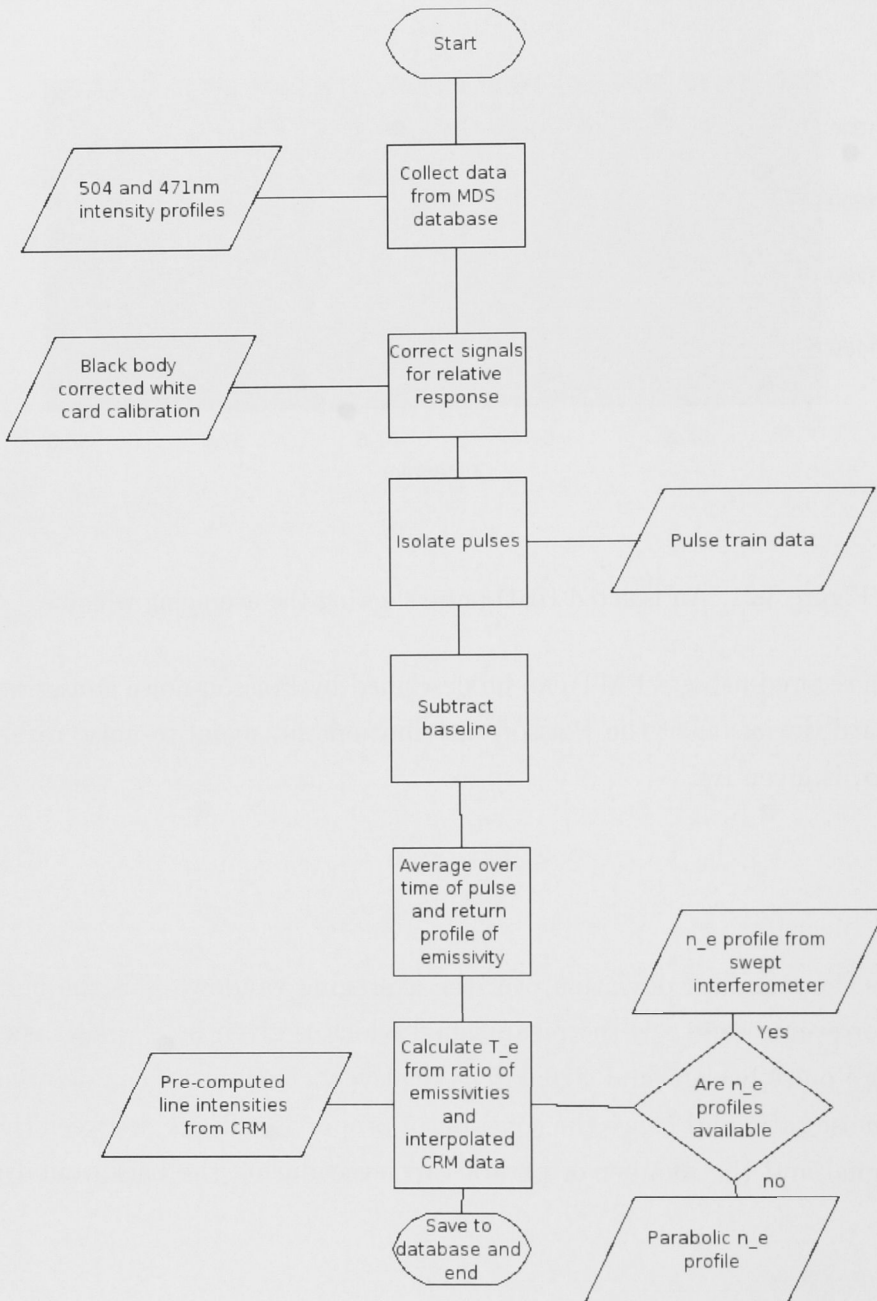


Figure 3.22: A flowchart showing the procedure for the extraction of helium emissivities and the calculation of  $T_e$  using helium line ratios

filtered with a width  $w_t$  to take into account the affect of averaging over the pulse on the uncertainty. The uncertainty in the returned emissivity at a wavelength  $\lambda$  (see section 3.7) is given by the geometric sum of the uncertainty in the background measurement and pulse measurement (derived from the signal to noise ratios)

$$(\Delta I_\lambda)^2 = (\Delta p_\lambda)^2 + (\Delta b_\lambda)^2 \quad (3.15)$$

and the uncertainty in the ratio,  $R$ , is given by

$$\left(\frac{\Delta R}{R}\right)^2 = \left(\frac{\Delta I_{504}}{I_{504}}\right)^2 + \left(\frac{\Delta I_{471}}{I_{471}}\right)^2 \quad (3.16)$$

$$(3.17)$$

where  $I_{504}$  and  $I_{471}$  and the extracted emissivities. The calculation of the signal-to-noise ratio for the measured base line and pulse signals combined with equation 3.15 and equation 3.17 will give a measure of the uncertainty in the ratio of emissivities. As can be seen in figure 3.4 the relationship between ratio and  $T_e$  is nearly linear, therefore we assume that relative error is conserved in the transformation from  $R$  to  $T_e$ .

### 3.4.2 A sample result: Electron resonantly heated He + H plasma

The helium beam was injected into a 0.5T ECH heated He + Hy plasma. A short burst of RF power at the fundamental ion cyclotron resonance was used to provide some seed electrons for the ECH breakdown. Figure 3.23 shows the measured emissivity and associated  $T_e$  as a function of major radius 11ms into the discharge. The emissivity reaches a peak value in the edge of the plasma and quickly falls away. Figure 3.23(b) shows the inferred peaked symmetric  $T_e$  profile with an on axis temperature of  $150 \pm 20$  eV. The outboard side of the profile shows low uncertainties due to the brighter light signals received. The drop in signal levels across the plasma is due, in part, to the ionisation of the beam across the plasma. This is confirmed using a time dependent CRM as part of a self-consistency check in section 4.6. This means, while the HBD is useful as a core  $T_e$  diagnostic at H-1NF temperatures, in larger, more powerful devices the technique lends itself more to edge temperature diagnosis (for example on the RFX reversed pinch [Carraro et al., 2000]). This result, as well as others that will be presented in proceeding chapters, highlights the ability of the HBD to attain temporally and spatially resolved  $T_e$  profiles. These profiles will be used in section 5.6.1 to provide an estimate of the fuelling profile of a directional injection system. The HBD system will also be used to investigate the formation of He + H electron resonantly heated plasmas at 0.5T in the next chapter.

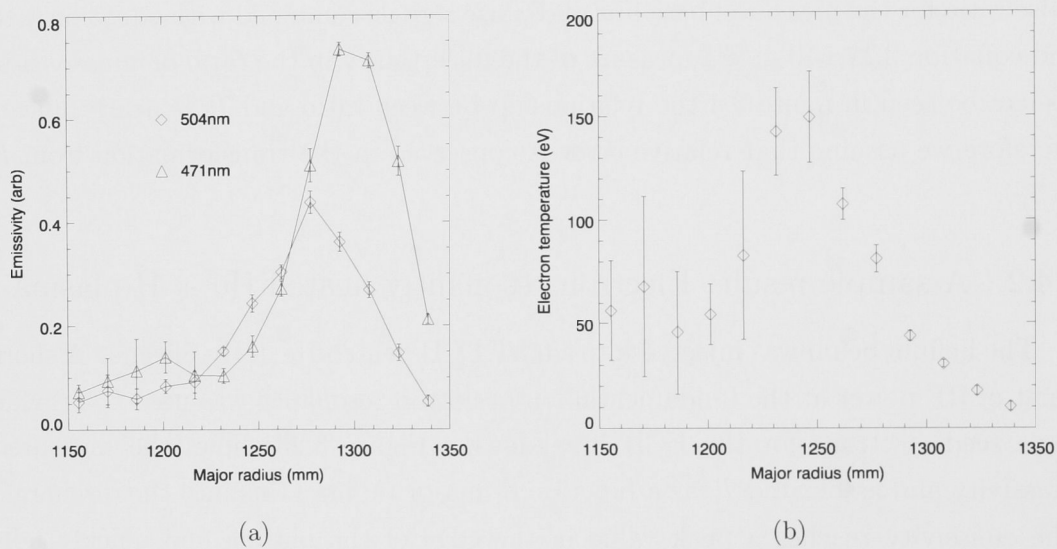


Figure 3.23: (a) Extracted emissivity profiles, note the attenuation due to ionisation. (b) The calculated temperature profile. This data is for discharge 61031.

# Studies of resonantly heated plasmas using the HLR diagnostic

The most exciting phrase to hear in science, the one that heralds new discoveries, is not “Eureka!” (I found it!) but “That’s funny ...”

– *Isaac Asimov*

In chapter 2 it was concluded that a directional gas injection system was required to meet the fuelling needs of the H-1NF heliac. Chapter 3 detailed the installation and testing of a helium beam based line ratio  $T_e$  diagnostic, a basic measurement required to predict the interaction between the plasma and a fuelling beam. In this chapter we present the results of a number of studies carried out with the diagnostic beam as well as the ELSI  $n_e$  diagnostic (section 2.1.2) and, as will be introduced in this chapter, the coherence imaging camera (section A). These results highlight the performance of the HLR diagnostic as well as providing  $T_e$  information for the design of the fuelling system presented in chapter 5.

## 4.1 Experimental condition for ECH plasmas

Plasmas studied in this chapter were primarily generated and heated using the ECH system described in section 1.3.2. Figure 4.1 shows a time sequence for discharge 61031 on H-1NF. This discharge used a plasma preparation sequence which is typical for H-1NF ECH plasmas. The helical ratio ( $\kappa_h = I_{sec}/I_{main}$ ) was 0.8 and a static fill of density  $0.9 \times 10^{17} \text{m}^{-3}$  of helium was used. Once the power supply has energised the magnetic coil set a 5ms pulse from the 7MHz transmitters generates a low density ( $n_e < 1 \times 10^{17} \text{m}^{-3}$ ) target plasma. All timings presented in this chapter are relative to the commencement of the RF pulse. The pre-pulse plasma is allowed to decay until, 50ms later, the ECH is initiated. A soft breakdown at the end of the waveguide has been observed for longer ECH pulse widths, possibly

due to reflections from the plasma. To avoid this phenomena the width of the ECH pulse was limited to 15ms.

A pulse train generator was used to send a sequence of pulses to the helium beam diagnostic (HBD) while a gate signal from the H-1NF control system was active. Following the findings of chapter 3 the inter-pulse time was set to 1.8ms. The pulses are clearly visible in figure 4.1 above the background (impurity + non-localised He) light.

## 4.2 Plasma evolution of discharge 61031

To highlight the performance of the HLR system we studied the evolution of discharge 61031 (typical of the ECH studies in this chapter). We obtained the density profiles by inverting projections measured using the ELSI device (section 2.1.2). Using the techniques discussed in section 2.2 the inversions were carried out using 8 flux surfaces (i.e. 8 concentric annuli of constant radius in flux co-ordinates). Figure 4.2 shows the evolution of the  $T_e$ ,  $n_e$  and electron pressure ( $P_e = n_e k_B T_e$ ) profiles in cartesian co-ordinates at the helium line ratio (HLR) viewing port. To calculate the  $P_e$  profile the  $n_e$  data shown in figure 4.2 needed to be interpolated onto the time base of the HLR system.

Figure 4.2 shows the electron density ramping up throughout the discharge and reaching a peak density of  $2 \times 10^{18} \text{m}^{-3}$ . This is approximately 20 times greater than the static helium fill of  $n_s = 0.8 \times 10^{17} \text{m}^{-3}$ . Since the volume of the plasma is approximately  $1 \text{m}^3$  this is roughly equal to the plasma electron inventory  $N_e$ . The plasma electron inventory is the total number of liberated electrons contained within the plasma volume. This fuelling condition was used for all ECH discharges presented in this chapter. Figure 4.3 shows the rate of rise of the electron inventory,  $V_p d\bar{n}_e/dt$ , where  $V_p$  is the magnetic volume (conveniently  $1 \text{m}^3$ ). The rate of rise increases over the duration of the plasma and appears to reach an equilibrium towards the end of the discharge.

The rate of particles crossing the last closed flux surface from the static fill (or particle injection rate  $N_s$ ) is given by

$$N_s = A_p \Gamma_s \quad (4.1)$$

$$= A_p n_s v_{th} / 4 \quad (4.2)$$

where  $\Gamma_s$  is the thermal flux across the plasma boundary,  $v_{th}$  is the average thermal velocity of helium neutral particles and  $A_p$  is the surface area of the plasma which

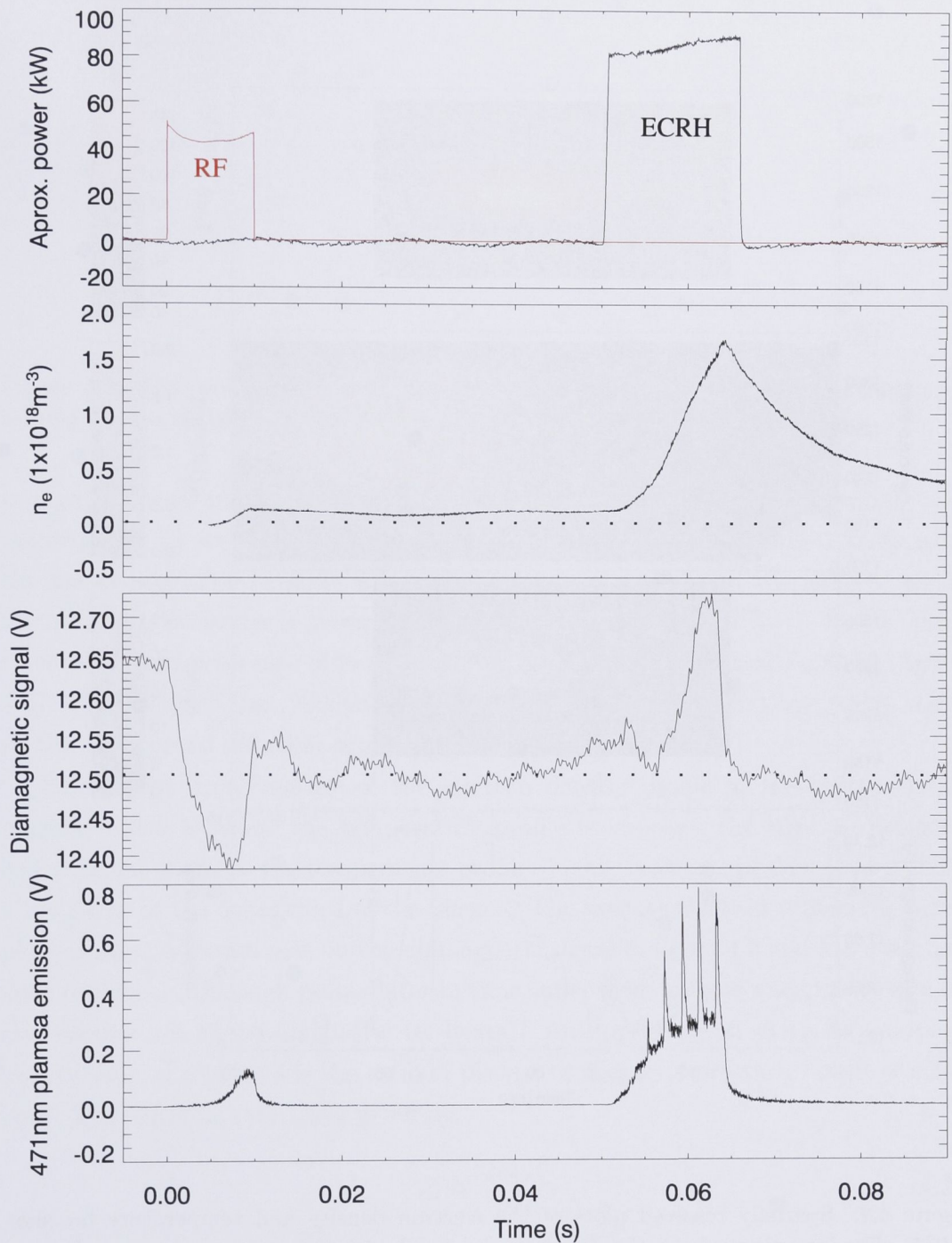


Figure 4.1: Time series for H-1NF discharge 61031 showing the evolution of the line-averaged electron density (as measured by the 2mm interferometer), diamagnetic signal and emission as viewed through the 471nm spectral filter.

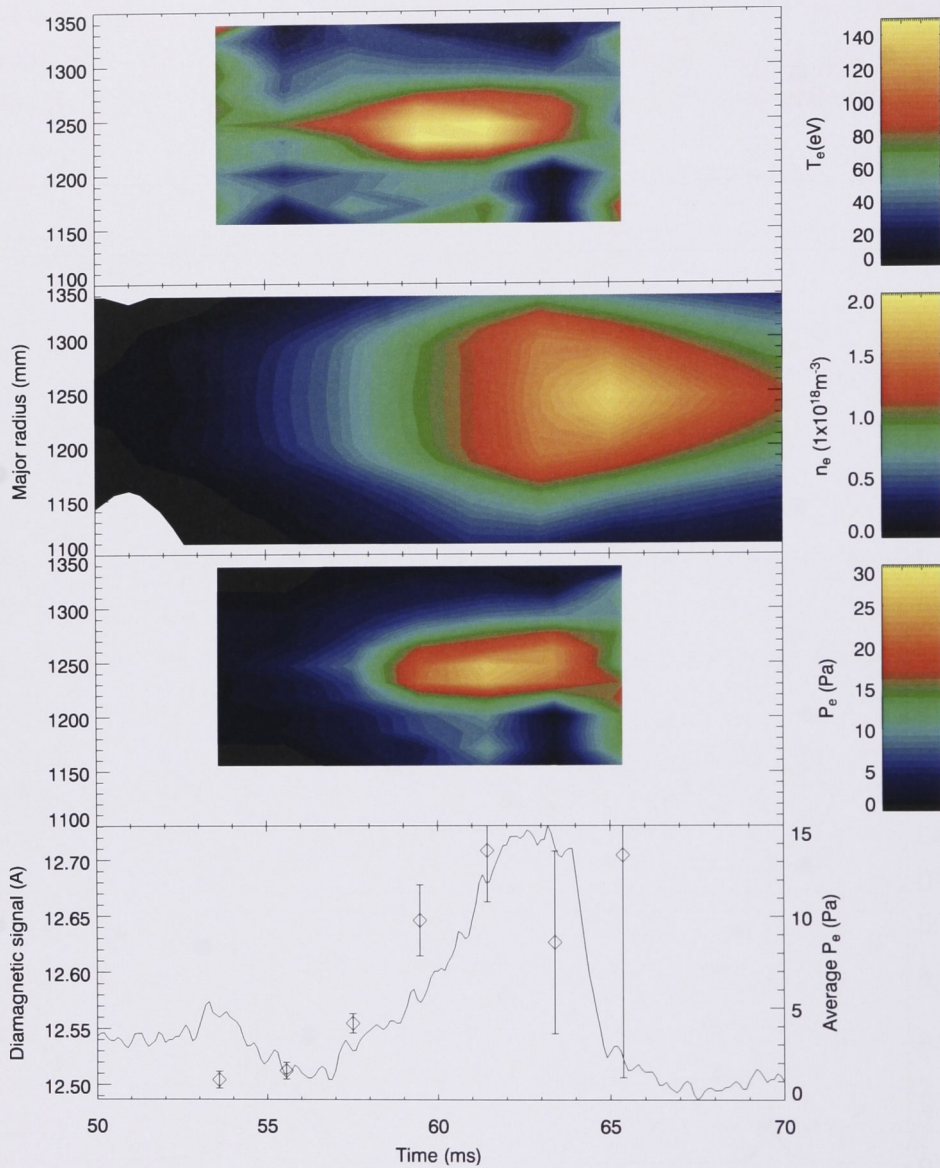


Figure 4.2: Spatially resolved plots of the electron density and temperature for shot 61031. The last panel shows the diamagnetic signal with the volume averaged electron pressure overplotted using an independent axis. It should be noted that although the use of contour plot presents the illusion of continuous data the plot of electron density consists of only 13 sweeps of the ELSI device and the electron temperature plot only consists of 7 profiles. The electron density profile was remapped to the electron temperature timebase to calculate the average  $P_e$  in the bottom panel.

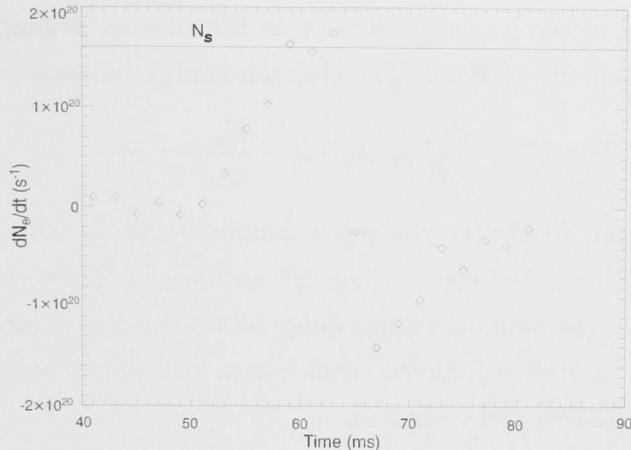


Figure 4.3: The rate of rise of the plasma electron inventory and the approximate (assuming a torus shaped plasma) particle injection rate from the static fill, ( $N_s$ )

is approximated as the surface area of a torus with the same average minor and major radius as the H-1NF plasma. The gas fill used in discharge 61031 (assuming the gas is in thermal equilibrium with the vacuum vessel and therefore at room temperature) generates a thermal particle rate,  $N_s$ , of  $1.6 \times 10^{20} \text{s}^{-1}$ . This is close to the observed peak rate of rise of the density profile as measured by ELSI (figure 4.3). This suggests that, like the plasmas presented in chapter 2, these plasmas are fuelled by thermal diffusion across the plasma boundary.

Due to the broad nature of the electron density profile in the centre of the plasma, which is where the temperature profile is steepest, the electron pressure has a similar shape to the temperature profile: highly centrally-peaked falling off to a low value in the outer third of the plasma. The average electron pressure is over-plotted using a second axis on the diamagnetic signal in figure 4.2 and has a similar time evolution (although points later in time suffer from greater uncertainty due to the attenuation of the diagnostic He beam). An important quantity for studying the stability of a plasma is the ratio of plasma to magnetic pressure, or the plasma beta. The electron beta,  $\beta_e$  is given by

$$\beta_e = \frac{2\mu_0 P_e}{B^2} \quad (4.3)$$

where  $B$  is the magnitude of the magnetic field and  $\mu_0$  is the permeability of free space. The maximum average plasma pressure was 12Pa while the magnetic pressure,  $B^2/2\mu_0$ , at 0.5 tesla was  $9.9 \times 10^4 \text{Pa}$  giving a  $\beta_e$  of 0.01%. This value is well within the limits for plasma stability (using the Mercier criterion) according to [Gardner & Blackwell, 1992].

The peak stored electron energy density in the plasma is simply  $3/2P_e$  which gives a peak stored energy of 17.9J. The electron energy balance is given by

$$\frac{dE_{st}}{dt} = k_c P_{ech} - \frac{E_{st}}{\tau_{Ee}} \quad (4.4)$$

where  $P_{ech}$  is the input ECH power which is coupled to the plasma with a coupling constant  $k_c$ ,  $E_{st}$  is the stored electron energy and  $\tau_{Ee}$  is the electron energy confinement time which represents electron energy losses through a variety of processes including (but not limited to) direct orbit losses, collisional heating of the ions, electron impact excitation and ionisation.

Examination of the pressure profile temporal evolution in figure 4.2 shows the pressure is stationary between 62-65ms. Setting the derivative in equation 4.4 to zero yields an expression for the electron energy confinement time

$$\tau_{Ee} = \frac{E_{st}}{k_c P_{ech}}. \quad (4.5)$$

According to [Nagasaki et al., 2001] the average value of  $k_c$  over the profile is approximately 0.5. Taking the approximate heating power (from figure 4.1) as being 80kW gives an electron energy confinement time of  $0.4 \pm 0.15$  ms.

### 4.3 Transformation to flux co-ordinates and symmetry

To compare results obtained at different toroidal locations the measurements must be mapped onto a common co-ordinate system. We assume that the measurement quantity is constant on a magnetic flux surface. Using a mapping of the output of the Gourdon code (see Appendix A of [Michael, 2003]), points in cartesian co-ordinates (major radius and distance above the mid plane) can be transformed into normalised flux co-ordinates (see section 1.2). The left panel of figure 4.4 shows a Poincaré plot of the magnetic flux surfaces calculated using the HELIAC code [Blackwell et al., 2001] at the toroidal location of the HLR diagnostic with flux surfaces calculated using the mapping procedure overlaid in orange. Figure 4.4 shows close correspondence between the puncture plot and surfaces computed using the Gourdon interpolation code. The right panel of figure 4.4 shows the transformation of a series of points into a co-ordinate system where flux surfaces are circular. Figure 4.5(a) shows two temperature profiles, as measured using the HLR system, in both cartesian and flux co-ordinates. The profiles are from two different magnetic configurations with a helical ratio ( $I_{main}/I_{sec} = \kappa_h$ ) of 0.22 (black) and 1.02 (red). As shown in figure 1.5 increasing  $\kappa_h$  shifts the plasma outwards. Figure 4.5(b)

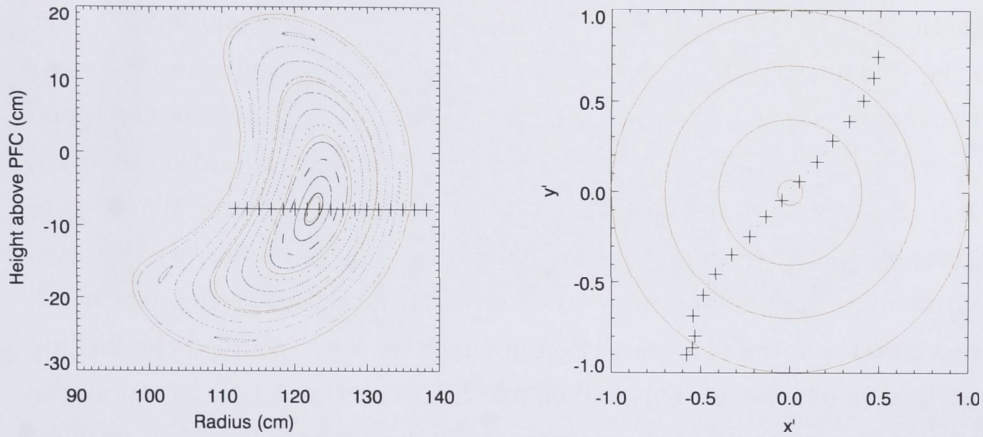


Figure 4.4: Transformation between cartesian co-ordinates and flux co-ordinates. The image on the left shows flux surfaces calculated using the HELIAC code and, overlaid in orange, surfaces of constant  $r$  calculated by interpolating the Gourdon code output. The image on the right shows the transformation of the points (crosses) in the left hand figure to a co-ordinate system where flux surfaces are circular.

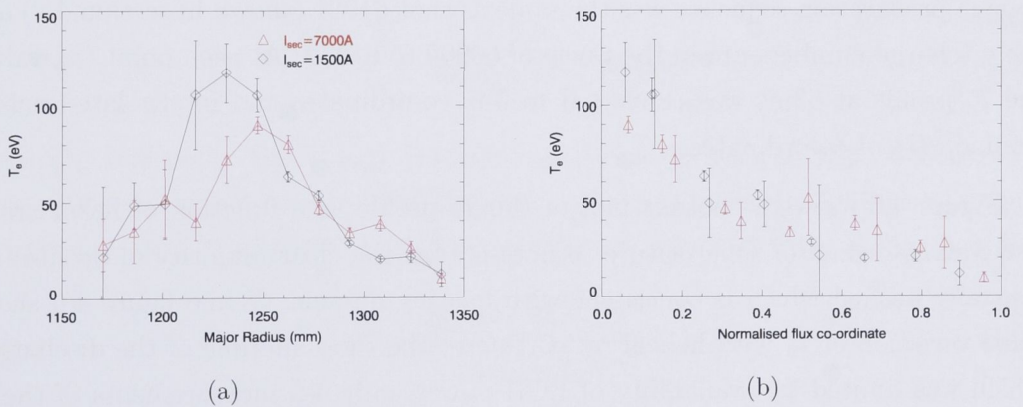


Figure 4.5: Profiles of electron temperature at two different magnetic configurations. (a) In cartesian co-ordinates. (b) Mapped onto normalised flux co-ordinates ( $r$ )

shows the same data mapped onto flux co-ordinates, in this case the radial flux co-ordinate. Mapping to flux co-ordinates effectively folds the two sides of the profile on top of each other, so a data point in figure 4.5(b) will either inboard or outboard of the magnetic axis ( $r = 0$ ). In general, due to the decreasing signal levels as the beam from the HBD propagates into the plasma, the inboard points are the points with the greater uncertainty. The profiles shown in figure 4.5(b) display very good symmetry, which confirms the accuracy of the registration and calibration reported in section 3.2. Furthermore, the degeneracy in the radial co-ordinate allows us to effectively increase the resolution of the measurement. These profiles will be used to obtain a functional approximation to the electron temperature profile, which will be re-mapped onto the toroidal cross section in which we have installed the fuelling injector described in chapter 5. This will enable us (in section 5.6.2) to model the fuelling profile of the device using an experimentally determined  $T_e$  and  $n_e$  profiles.

#### 4.4 Temperature profile as a function of helical ratio

To investigate the effect of  $\kappa_h$  on the plasma temperature profile we performed a scan of the helical ratio. A simulation using the HELIAC code shows that the effect of changing the helical ratio on the magnetic field at the magnetic axis is small (<1%) so there should be no change in the ECH resonance condition. The plasma preparation sequence was the same as shot 61031 (shown in section 4.2) and the discharge numbers are in the range of 60909 to 61039. At each point ( $\kappa_h$  value) the  $T_e$  profile at 63ms was converted to flux co-ordinates and interpolated onto a common set of co-ordinates.

Figure 4.6 shows a contour plot of the  $T_e$  profile as a function of helical ratio and flux co-ordinate. One feature to note is that the clear majority of profiles are centrally peaked which is consistent with heating on-axis. While figure 4.6 shows some variation of  $T_e$  with helical ratio. Due to the short lifetime of the discharges, which was limited by availability of ECH power, only 4-5 measurements of the  $T_e$  profile were possible. Another consequence of the short discharge length is that the plasma was not in equilibrium for some of the profiles which make up figure 4.6. Due to the shot-to-shot reproducibility issues, it is difficult to draw conclusions from this scan and a finer, more controlled scan is needed to investigate issues of plasma formation and energy confinement under ECH heating scenarios.

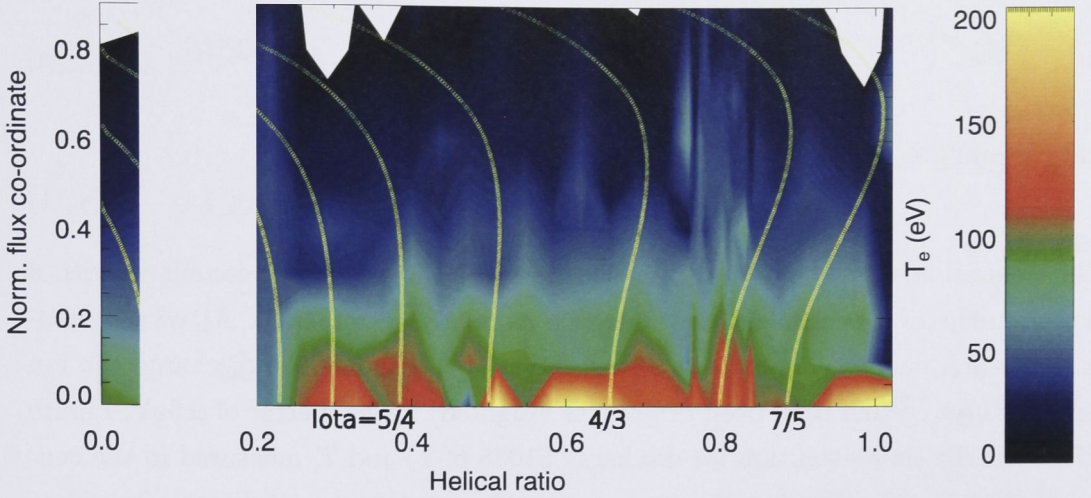


Figure 4.6:  $T_e$  profile in flux co-ordinates as a function of helical ratio. There was no data taken between  $\kappa_h = 0.0$  and 0.2. The radius of high order rational surfaces is overplotted.

## 4.5 Ion electron temperature equilibration

Ion cyclotron heating not only heats ions. Through interaction with the plasma sheath region electrons can be accelerated to high energies and re-thermalise in effect heating the electron population. Electron cyclotron heating almost exclusively heats the electron component of the plasma. The primary mechanism for the heating of ions in a exclusively electron heated plasma is through the collisional exchange of energy. The ion power balance is given by

$$n_i \frac{dT_i}{dt} = Q_{ei} - P_i \quad (4.6)$$

$$= \frac{3/2n_e(T_e - T_i)}{\tau_\epsilon^{ie}} - \frac{3/2n_i T_i}{\tau_{Ei}} \quad (4.7)$$

where  $Q_{ei}$  represents the energy transfer rate from the ions to the electrons,  $P_i$  represents the energy loss rate from the ions,  $\tau_{Ei}$  is the ion energy confinement time (at ion temperate  $T_i$ ) and  $\tau_\epsilon^{ie}$  is the electron ion equilibration time and is given by

$$\tau_\epsilon^{ie} = \frac{3(2\pi)^{3/2} \epsilon_0^2 m_i T_e^{3/2}}{2n_i m_e^{3/2} q_e^4 \ln \Lambda} \quad (4.8)$$

where  $m_e$  and  $m_i$  are the masses of the electron and ion,  $\epsilon_0$  is the permittivity of free space,  $q_e$  is the charge of the electron and  $\ln \Lambda$  is the Coulomb logarithm. Assuming steady state we can calculate the heat flux and hence the power balance as

$$Q_{ei} - P_i = \frac{3/2n_e(T_e - T_i)}{\tau_\epsilon^{ie}} - \frac{3/2n_i T_i}{\tau_{Ei}} = 0 \quad (4.9)$$

where  $\tau_{Ei}$  is the energy confinement time. Solving for  $T_i$  yields

$$T_i = \frac{\tau_{Ei} n_e T_e}{\tau_{\epsilon}^{ie} n_i + \tau_{Ei} n_e} \quad (4.10)$$

and assuming  $n_e \approx n_i$ ,

$$T_i = T_e \frac{\tau_{Ei}}{\tau_{Ei} + \tau_{\epsilon}^{ie}}. \quad (4.11)$$

Using equation 4.11 and  $T_e$  measured using the HLR diagnostic combined with a measurement of  $T_i$  using an ion coherence camera (see appendix A) we can estimate the ion energy confinement time. Towards the end of the discharge the ion temperatures (which have been brightness weighted) have an error of  $\pm 5\text{eV}$ . Figure 4.7 shows the time evolution for discharge 61038 of  $T_e$  and  $T_i$  measured in the centre of the plasma. The temperatures approach a stationary condition after 64ms with a  $T_e = (110 \pm 20)\text{eV}$  and a  $T_i$  of  $(15 \pm 5)\text{eV}$ . The  $n_i$  on axis was approximately  $3 \times 10^{18}\text{m}^{-3}$  yielding an  $\tau_{\epsilon}^{ie}$  of 43ms. The electrons and ions are not strictly in equilibrium so this will add some uncertainty to the measurement. Using equation 4.11 this yields an on axis ion energy confinement time of  $(6 \pm 2)\text{ms}$ . This confinement time is a factor of 10 greater than the electron energy confinement time. This is due to the ions being cold and having fewer energy loss channels (for example the lack of a radiative loss channel).

Using the ion coherence camera we observed ion flows in the plasma of order 5km/s which reverse about the centre consistent with rigid rotation. Assuming the electrons are in Boltzmann equilibrium the order of the radial electric field generated by the  $T_e$  gradient is

$$E \sim k_B T_e(0)/a \quad (4.12)$$

where  $T_e(0)$  is the on axis electron temperature and  $a \approx 4\text{cm}$  is the electron temperature scale length. This yields an electric field of order 2800V/m. The force balance for the ions is given by

$$\nabla P_i / (en_i) = \mathbf{E} + \mathbf{v}_i \times \mathbf{B} \quad (4.13)$$

where  $\mathbf{E}$  is the electric field,  $\nabla P_i$  is the pressure gradient and  $\mathbf{v}_i$  is the ion flow velocity. Since the ions are cold in the centre of the plasma,  $|\nabla P_i| \ll en_i |E|$  which gives

$$v_\theta \sim E_r / B_\Phi \quad (4.14)$$

where  $E_r$  is the electric field in the radial direction,  $B_\Phi$  is the magnetic field in the toroidal direction and  $v_\theta$  is the poloidal flow velocity. This gives a  $v_\theta$  of  $\sim 5.6\text{km/s}$  which is close to ion flow velocities observed by the ion coherence camera.

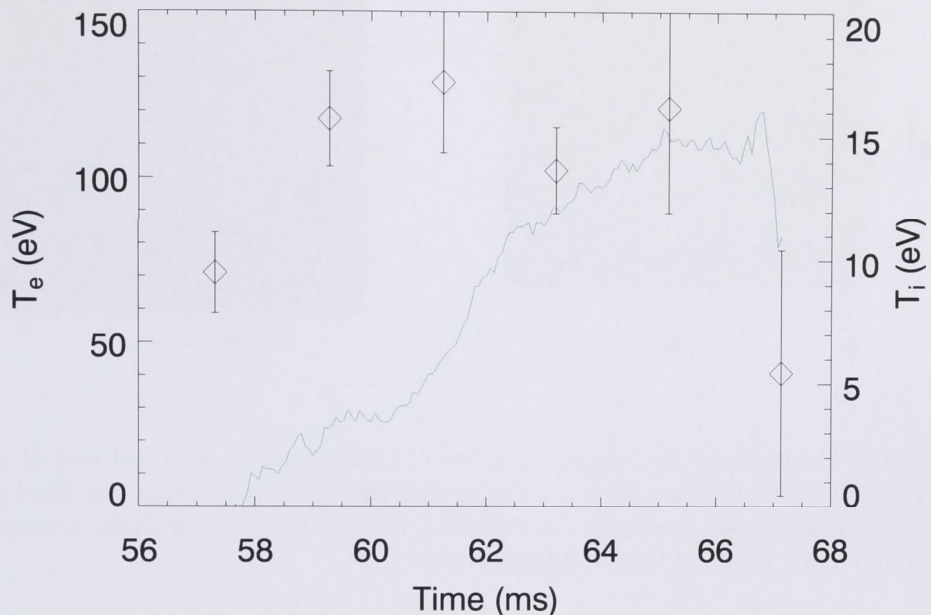


Figure 4.7: Time evolution of  $T_e$  (points) and  $T_i$  (curve) as measured by the central channels of the HLR and ion coherence diagnostics.

## 4.6 Beam propagation study using the time dependent collisional radiative model

The collisional radiative model presented in section 3.1 removes any time dependence by assuming that all states are in equilibrium. Using a modelled or experimentally determined  $T_e$  and  $n_e$  profile and, using the same rate coefficients as used in the steady state CRM, the populations of helium states at a particular position in the plasma can be calculated. Then, using the propagation velocity of the beam, the population of helium is propagated to the next position and used as an initial condition to calculate a new set of populations.

The time dependent CRM (TD-CRM) code was written by Robert Dall and uses the rate coefficients from the CRM code by [Goto, 2003]. The code accepts a plasma density and temperature profile and can take into account wave mixing and resonant absorption. However, as discussed in section 3.1, these corrections are unimportant for H-1NF plasma and were neglected to decrease computing time. We used a step size of 1ns which means for the propagation time of our beam of  $110\mu\text{s}$  110,000 steps need to be calculated. The code solves the set of simultaneous

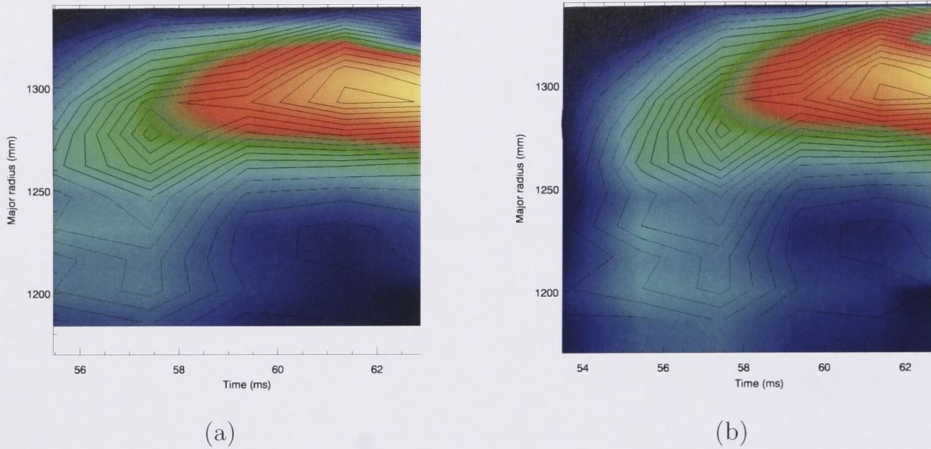


Figure 4.8: Contours of the emissivity of the 471nm transition as a function of time and major radius. The contour lines are the measured emissivities while the filled contours show the emissivity as calculated for the TD CRM.(a) Using a parabolic density profile. (b) Using reconstructions from the ELSI device.

differential equations at each point using the LSODE (Livermore Solver for Ordinary Differential Equations) library [Hindmarsh, 2006] and saves the populations of each state and rate of each transition as a function of position and time (via the velocity of the beam). To understand the emissivity profiles shown in figure 3.23 we used the TD CRM to propagate a beam with the same properties as the HBD through the H-1NF plasma. We used the  $T_e$  profile (time dependent) measured for discharge 61031.

Figure 4.8(a) shows the transition rate for the  $4^3S \rightarrow 2^3P$  (471nm) line as a function of time and major radius. The background image is the output from the TD CRM model while the contour lines show measured emissivities from the HLR viewing optics. A parabolic density profile scaled to the time dependent average electron density (as measured by the 2mm interferometer) was used as the  $n_e$  input to the model. Figure 4.8(b) is similar to figure 4.8(a) however the TD CRM output was calculated using a reconstructed density profile from the ELSI (see section 2.1.2) interferometer. Both figures show a good agreement in the evolution of the emissivity profile with the centre of mass of the emission moving from the centre of the plasma to the edge as the discharge progresses and the mean free path (to ionisation) of the beam neutrals decreases. A slice at 60ms is shown in figure 4.9. Given uncertainties involved in both the raw data and model (for example errors in the cross sections used), a very good agreement exists between the model and scaled (to a constant common to both cameras) data. The dashed lines represent

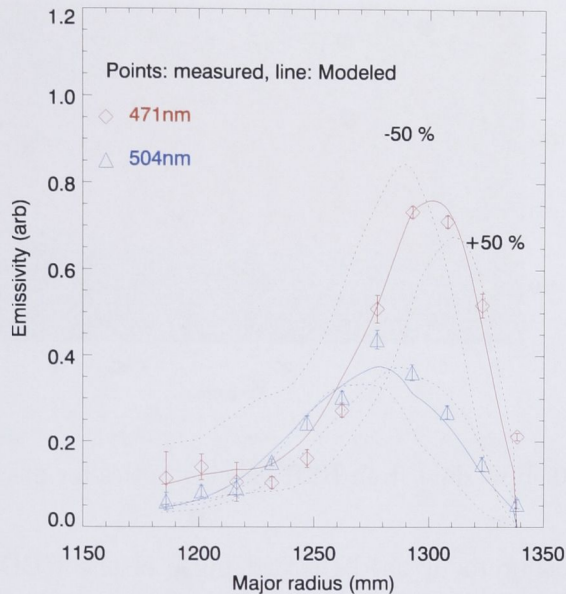


Figure 4.9: Measured emissivity profiles (both scaled by a common constant) and the TD-CRM output.

modeled emissivities for a plasma with a 50% lower and higher  $T_e$  profile. This sensitivity test shows that, due to ionisation of the beam, the peak in emissivity moves towards the centre of the plasma with decreasing  $T_e$  and the agreement of our modeled emissivity to the measured emissivity validates the  $T_e$  measurement.

These results not only gives us confidence in the  $T_e$  profiles returned from the HLR measurement, it also gives us confidence in the TD CRM required to use it to calculate the fuelling properties of the injection system discussed in the next chapter (see section 5.6).

## 4.7 $T_e$ profile for a ion cyclotron heated plasma

To investigate the performance of the HLR diagnostic on a lower temperature plasma we measured the  $T_e$  profile for an ion cyclotron heated (ICH) plasma. The plasma preparation sequence for the discharge studied (discharge 62274) was similar to that used in the scans presented in section 2.4. We used a helical ratio ( $\kappa_h$ ) of 0.8. Instead of firing multiple short pulses we used long pulses of  $285\mu\text{s}$  trading off pulse quality for increased brightness. The source pressure was 600kPa and the raw data is shown in figure 4.10.

Figure 4.11 shows the measured emissivities and  $T_e$  profiles at 24ms into the

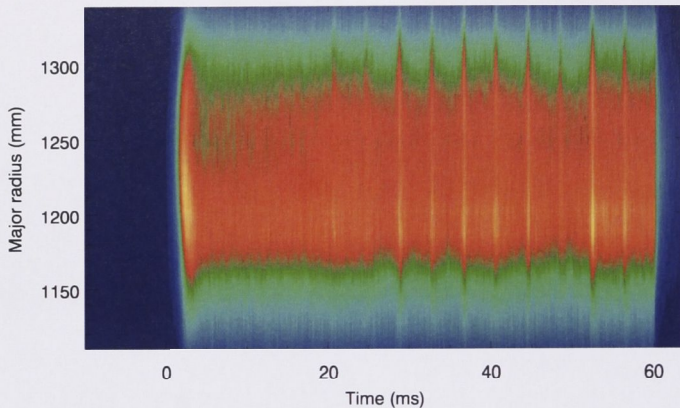


Figure 4.10: Raw data from HLR viewing optics for discharge 62274.

discharge. This measurement used the 3rd pulse of the HBD which, according to the results presented in section 3.3.1, will have a full width at half maximum in the plasma of order 50mm. The result, which is clearly different to the ECH case, shows a hollow profile for both emissivity and  $T_e$ . The emissivity curve shows little sign of attenuation across the plasma, consistent with the inferred lower electron temperatures. To confirm the validity of this result we performed the same TD CRM propagation calculation discussed in the previous section using a parabolic profile for  $n_e$ . The  $T_e$  point in figure 4.11 near 1250mm minor radius was ignored due to high uncertainty and was replaced with an interpolated data point. Figure 4.12(a) shows the emissivity data with the scaled TD CRM generated emissivities over-plotted. The model shows very good agreement to the data except in the centre of the plasma where the very low ( $T_e < 2\text{eV}$ ) electron temperature point at 1275mm major radius causes the model to return an emissivity which is much lower than the measured value. Given that the measured emissivities are the primitive measurement we modified the  $T_e$  profile used by the TD CRM to improve the agreement between the model output and measured emissivities.

Figure 4.12(b) shows the scaled TD CRM generated emissivities resulting from a modified  $T_e$  profile. The modification was to increase the temperature at 1230mm minor radius from  $\sim 2\text{eV}$  to  $9\text{eV}$ . The figure shows much better agreement between the model and the measurements for both the 471nm and 504nm transitions. Figure 4.13 shows the model results using a  $n_e$  profile reconstructed from ELSI data taken during a discharge similar to 62247 (61203). The reconstructed density profile (shown in figure 4.14(a)) is narrower than the parabolic profile used in the previous calculations leading to lower modeled emissivities in the edge.

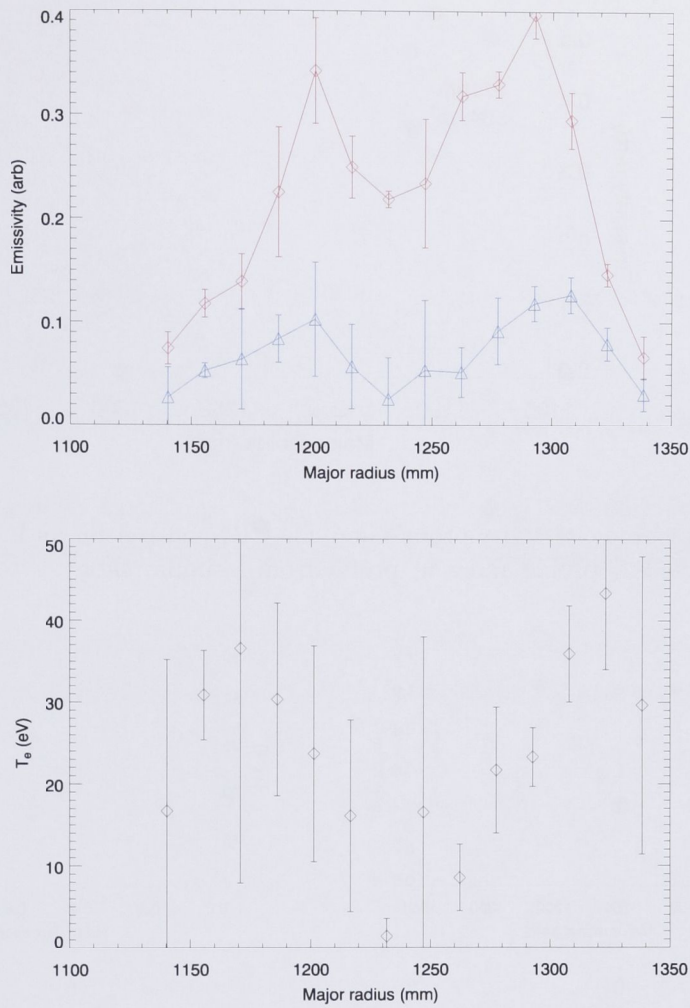


Figure 4.11: Emissivity and temperature profiles measured using the HLR diagnostic during an ICH plasma.

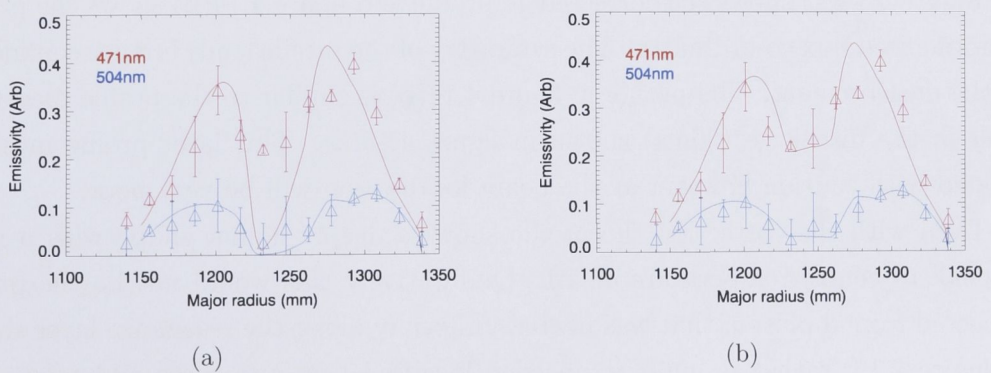


Figure 4.12: Measured emissivity profiles and TD-CRM output for an ICH heated plasma using the (a) original and (b) corrected  $T_e$  profiles.

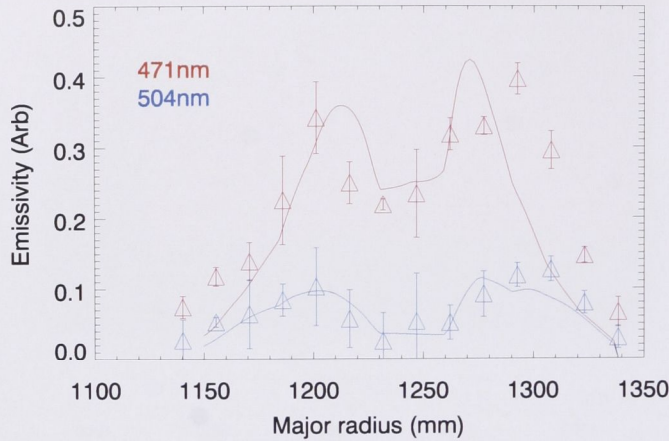


Figure 4.13: Measured emissivity profiles and TD-CRM output for an ICH heated plasma using the corrected  $T_e$  profile and a  $n_e$  profile from a similar shot.

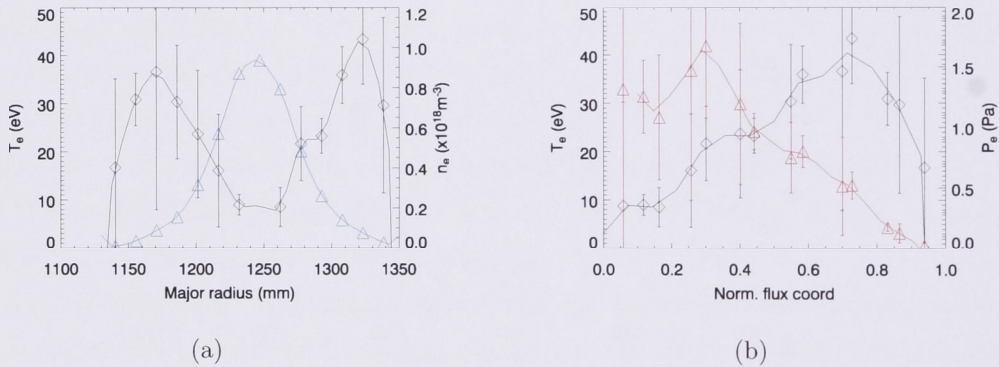


Figure 4.14: Corrected  $T_e$  profile in cartesian and flux co-ordinates. The density profile is shown in blue in figure (a) and the pressure profile is shown in red in figure (b).

Figure 4.14(a) shows the corrected  $T_e$  profile and figure 4.14(b) shows the profile in normalised flux co-ordinates. The symmetry of the profile lends further confidence to the measurement. The profile in figure 4.14(b) is similar to the profile measured later in the discharge (56ms) shown in figure 4.15(a). This later profile must be treated with caution however as the beam localisation will be very poor.

Even with the correction the profile shows a deeply hollow shape with a ratio of peak to centre temperature of 4:1. Qualitatively this would not be the profile expected from a plasma that was heated uniformly along the resonance layer shown in figure 2.12, rather it hints at an edge localised heating source and may point towards antenna sheath effects playing a role. Even though the temperature profile is hollow, as shown in figure 4.14(b) the electron pressure profile is flat in the centre

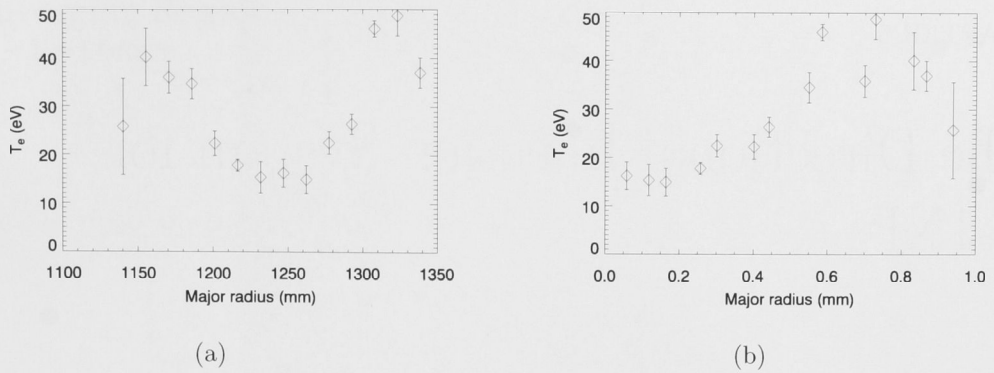


Figure 4.15:  $T_e$  profile measured late (56ms) in discharge 62247.

and decreases towards the edge. This is required as a pressure gradient driven flux would otherwise be established and act to flatten any hollow electron pressure profile.

We have shown that the naive application of helium line ratios to determine  $T_e$  must be checked for consistency with TD CRM modeling of the observed emissivities.

# The Directional Injection System for H-1NF

The man who says it cannot be done should not interrupt the man doing it

– *Chinese Proverb*

As discussed in section 2.6, the large gas reservoir surrounding the H-1NF plasma leads to difficulties in achieving the density control required to maximise the plasma temperature. These conditions were unsuitable for our initial goal of studying particle transport in the heliac as a function of magnetic configuration. This led to the decision to design, build and test a directional gas injection system that removed or at least lessened the reliance of the plasma on the thermal diffusion of the static bath for fuelling. This chapter discusses the theory, characterisation and implementation of this system. The chapter begins with a review of fuelling devices and the theory that underpins the generation of directional supersonic flows. The chapter then discusses the mechanical design of the system and presents results of measurements carried out in a test chamber using constant temperature hot wire anemometry. The chapter concludes with a discussion of the interaction between the beam and the plasma using a simple model and then the TD CRM that was introduced in the previous chapter.

## 5.1 Review of current fuelling systems

A simple standard fuelling technique is gas puffing, where gas is injected into the vacuum vessel using a valve (usually a piezo electric valve) and a delivery method such as a tube. This technique is unsuitable for H-1NF (for reducing the background gas inventory) as the delivery system would have to be close to the last closed flux surface, the position of which varies with  $\kappa_H$ . More complex fuelling techniques

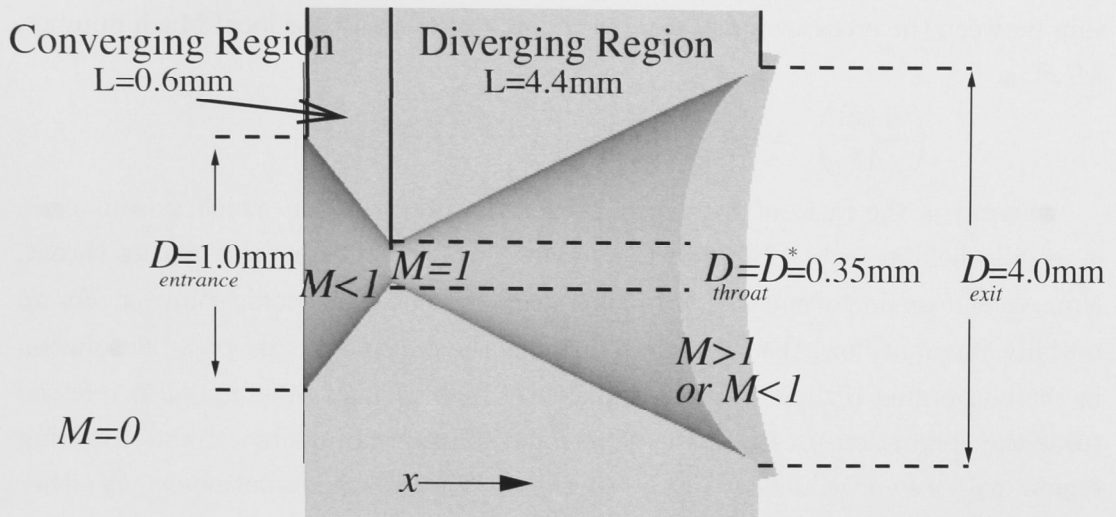


Figure 5.1: Cross section of the double conical nozzle used to generate the supersonic flow

which directly fuel the core of the plasma include Neutral Beam Injection (NBI) (also used for heating) and pellet injection. These techniques are described in detail in [Milora, 1982]. Another developmental technique for the fuelling of plasmas is compact toroid (CT) injection ([Park, 1988] and [Liu et al., 2006]) where a small plasma is accelerated into the plasma. However, due to the modest size and power of the H-1NF plasma, NBI, CT injection and pellet injection are not feasible fuelling options. A more appropriate solution is to use Supersonic Molecular Beam Injection (SMBI). The supersonic flow can be generated using a variety of means. On HL-1M [Yao et al., 1998] a nozzle and skimmer arrangement is used to obtain a well collimated beam. For simplicity, our system (section 5.2) uses a double conical nozzle (essentially a non optimised de-Laval nozzle, see pp 177-9 of [Anderson, 1990]) to generate the supersonic flow. This is similar to the system to be installed on the NSTX experiment [Soukhanovskii et al., 2004].

## 5.2 Theory

A directional, supersonic beam can be produced by discharging high pressure (in relation to the pressure at the exit) gas through a double conical nozzle (figure 5.1, see pp 177-9 of [Anderson, 1990]). Such a nozzle produces a flow which is cooled as it is accelerated, thereby decreasing  $\langle v_{\perp} \rangle$  while increasing  $v_{\parallel}$ , where  $\langle v_{\perp} \rangle$  is the average perpendicular component of the beam velocity and  $v_{\parallel}$  is the component of the beam velocity in the direction of the nozzle axis (the x direction in figure 5.1).

Manipulation of the isentropic flow relations [Anderson, 1990] yields a relation-

ship between the cross sectional area,  $A(x)$ , of a nozzle and the local Mach number,  $M(x)$ .

$$\left(\frac{A(x)}{A^*}\right)^2 = \frac{1}{M^2(x)} \left[ \frac{2}{\gamma+1} \left( 1 + \frac{\gamma-1}{2} M^2(x) \right) \right]^{\gamma+1/\gamma-1} \quad (5.1)$$

where  $\gamma$  is the ratio of specific heats for the injected gas, which, in our case, is usually helium ( $\gamma = 1.67$ ) and the superscript \* denotes a value at the throat. Numerical inversion of equation 5.1 yields a supersonic and subsonic solution. For an initially stagnant flow, the subsonic solution is the only physically possible solution in the converging region. Given a sufficiently high plenum pressure (also referred to as the stagnation pressure) the supersonic solution is possible in the diverging region, with a sonic value ( $M = 1$ ) at the throat. The subsonic solution occurs either when the exit pressure is lower than the pressure of the gas into which the nozzle exhausts, or when expansion waves in the diverging region re-inforce to produce a standing shock wave.

The isentropic flow relations can be used to estimate the rate at which particles are exhausted from the nozzle. The equations give

$$\frac{P(x)}{P_0} = \left( 1 + \frac{\gamma-1}{2} M^2(x) \right)^{-\gamma/\gamma-1} \quad (5.2)$$

$$\frac{T(x)}{T_0} = \left( 1 + \frac{\gamma-1}{2} M^2(x) \right)^{-1} \quad (5.3)$$

where  $P_0$  and  $T_0$  are the plenum temperature and pressure. At the throat of the nozzle, where  $M=1$ , we obtain  $P^*/P_0 = 0.48$  and  $T^*/T_0 = 0.75$ . Combining these with  $P = nkT$  and using the sonic speed  $v^* = \sqrt{\gamma RT^*}$ , where  $R$  is the ideal gas constant and  $k$  is Boltzmann's constant, gives the particle injection rate ( $N_p$ ) from the nozzle for helium as

$$N_p = n^* v^* A^* = A^* \frac{0.58 P_0}{k T_0} \sqrt{R T_0} \quad (5.4)$$

This linear relation between mass flow and plenum pressure allows a nozzle to be designed that gives the desired range of particle injection rates at the pressures we wish to use. Figure 5.3 shows the calculated particle injection rates for helium for a variety of nozzle diameters and plenum pressures. Based on this, a nozzle with a throat diameter ( $D^*$ ) of 0.35mm (figure 5.1), was selected to meet the particle injection rates (that is equivalent to a particle confinement loss rate of  $5 \times 10^{20} \text{s}^{-1}$  for a density of  $1 \times 10^{18} \text{m}^{-3}$  and confinement time of 2ms derived in section 2.6) required for the H-1NF device.

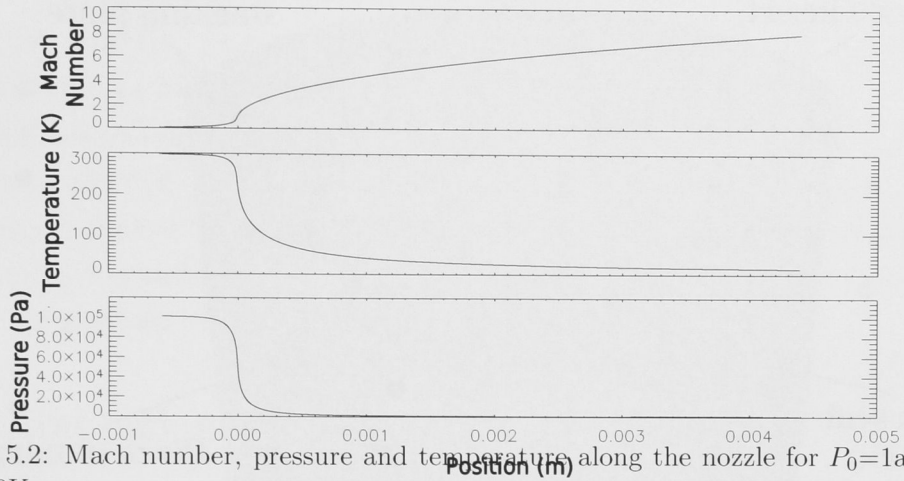


Figure 5.2: Mach number, pressure and temperature along the nozzle for  $P_0=1\text{atm}$  and  $T_0=300\text{K}$

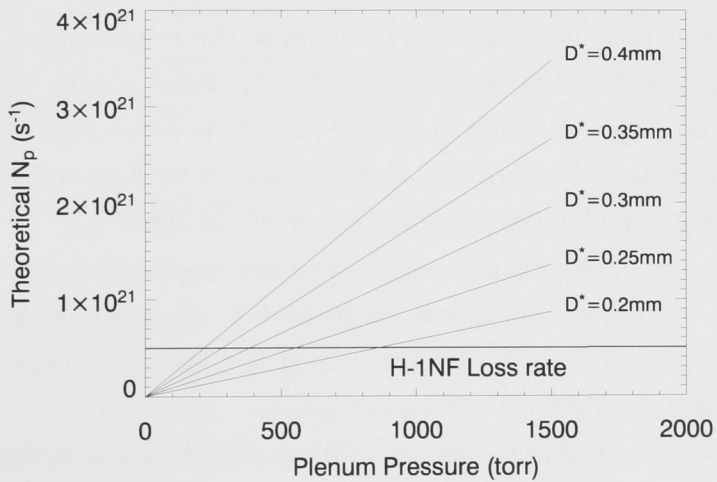


Figure 5.3: Variation of the particle injection rate showing a linear dependence on both plenum pressure ( $P_0$ ) and throat diameter ( $D^*$ ). A typical particle confinement loss rate is over-plotted.

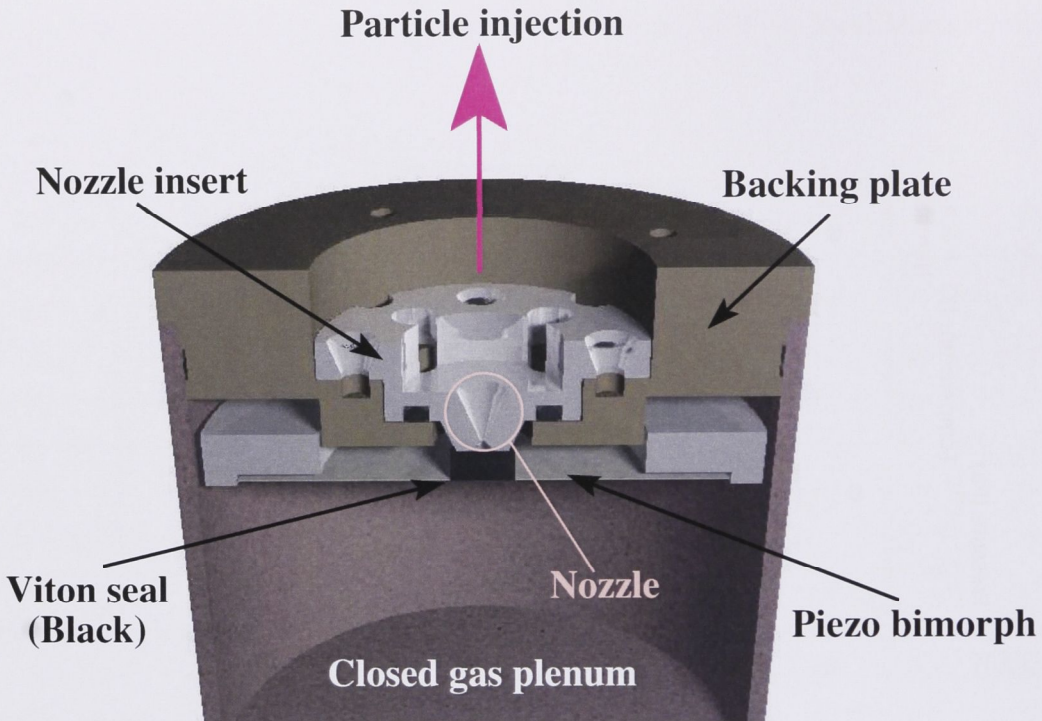


Figure 5.4: The valve assembly attached to the closed plenum system. The nozzle insert can be changed with a minor vacuum opening allowing different nozzles to be fitted as needs change.

The method of characteristics could be used to design a nozzle with an optimised shape (for a fixed pressure) that would minimise the reinforcement of expansion waves, which can lead to the development of such lateral shocks which can choke the flow. However, since we desire to operate the nozzle over a wide range of plenum pressures and therefore a wide range of exit pressures we have opted for a simpler approach of using a double conical nozzle as shown in figure 5.1.

The nozzle was machined into a stainless steel insert which was placed into a modified Veeco valve assembly (shown in figure 5.4) consisting of a backing plate, a viton seal and piezo bimorph. When a voltage is applied, the bimorph flexes and breaks the viton seal with the nozzle entrance.

The valve typically begins to open at 120V and is fully open at 180V. By varying the voltage between fully open and closed we are able to choke the flow to allow modulation of  $N_p$ .

The valve assembly shown in figure 5.4 is fixed to a closed plenum of volume 177ml. Filling of the plenum is controlled by a pneumatic valve while the pressure is monitored by a capacitance manometer. By measuring the drop in plenum pressure during gas injection it is possible to determine the total number of particles delivered

to the plasma. In contrast to injectors that use a nozzle skimmer arrangement this allows quantitative investigations of plasma fuelling.

The filling of the plenum and monitoring of the plenum pressure was achieved using a National Instruments DAQ card controlled via a PC running a custom LabVIEW program. The system controlled parameters and acquired signals which were stored in an MDSPlus database.

Prior to a plasma discharge, the plenum fill valve is opened until a programmed pressure is reached. When an appropriate trigger is received, a pre-programmed waveform is applied to an amplifier which drives the piezo-valve, while signals from the anemometer and plenum pressure gauges are acquired and then archived in the MDSPlus database for future analysis.

### 5.3 Test tank measurements

Before installation on the H-1NF device it was necessary to properly characterise the beam properties. For example, due to the non-optimised shape of our nozzle, it is likely that the isentropic flow condition may be violated via energy exchange between the flow and the nozzle or there may be shocks which disturb the flow. To investigate the flow the valve and plenum assembly were installed in a small vacuum test tank. A frame holding four diagnostic constant temperature anemometry (CTA) wires was mounted in front of, but at variable distance from the nozzle. The wires were 12mm in length and separated by 8mm. Various images and graphics of the test system are presented in figure C.4 in appendix C.

#### 5.3.1 Gas flux measurements

The CTA system, which is based on the system described in [Gross & Melissinos, 1975], involves immersing a tungsten wire, held at constant temperature by a feedback circuit (shown in figure 5.6) into the flow. A constant temperature system is used as energy lost by the wire through radiation varies as  $\sigma T^4$  where  $\sigma$  is the Stefan Boltzmann constant. Since this is highly non-linear a knowledge of the exact temperature as a function of time (during the exhaust of the gas) would need to be known. As particles strike the wire, energy is removed from the wire which in turn increases the current required to maintain the temperature of the wire (compared to the current required in vacuum). The change in current, denoted by  $S(t)$ , is proportional to the total number of particles striking the wire per unit time from both directed fluxes from the nozzle,  $\Gamma_{beam}(t)$ , and thermal background fluxes,  $\Gamma_{th}(t)$ .

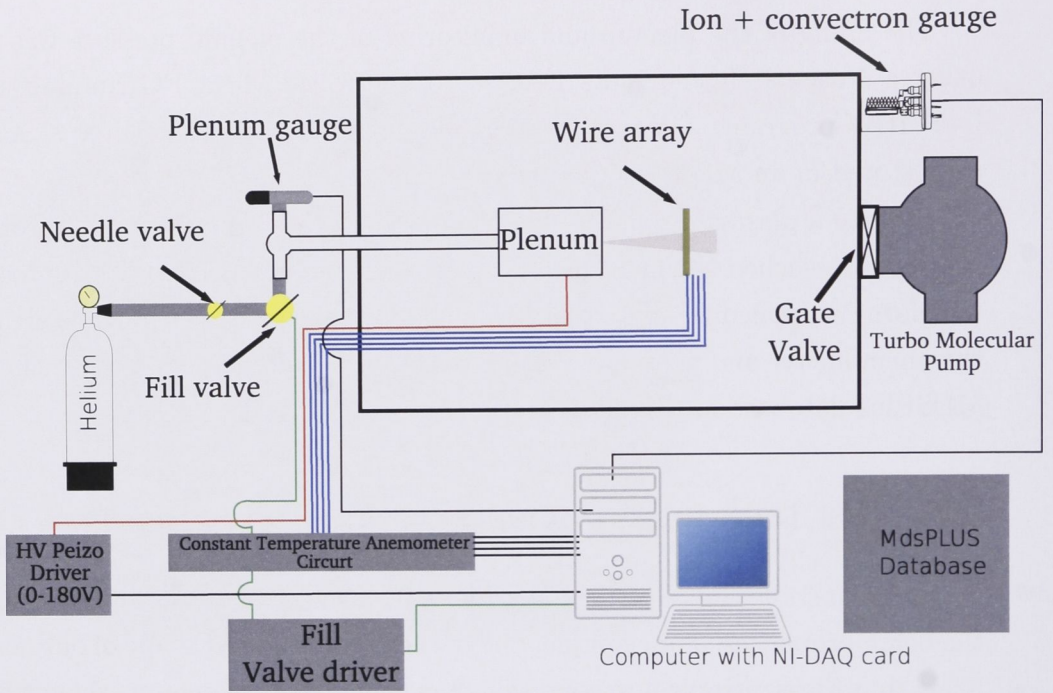


Figure 5.5: The layout of the DISH control systems and test tank.

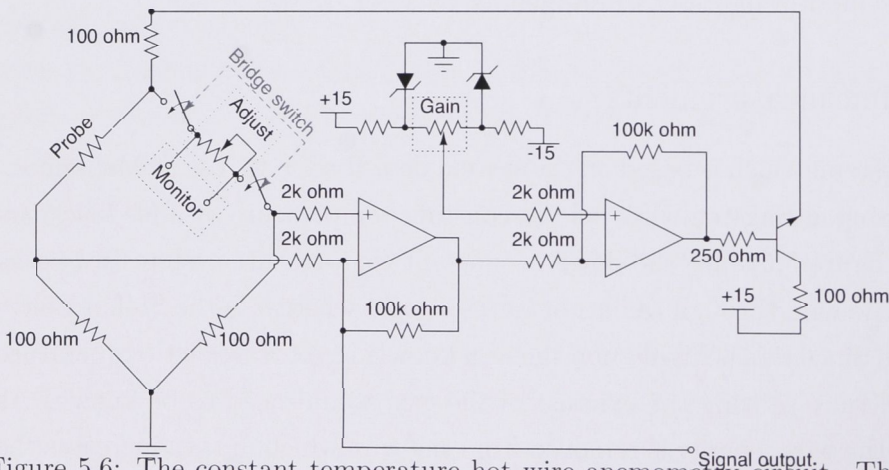


Figure 5.6: The constant temperature hot wire anemometry circuit. The wire (marked probe) is kept at a constant temperature by the injection of current from the +15V source via a transistor when the bridge is out of balance. The system is in balance when the resistance of the probe equals that of the adjustable resistor. Changing the resistance of the adjustable resistor changes the equilibrium temperature of the probe.

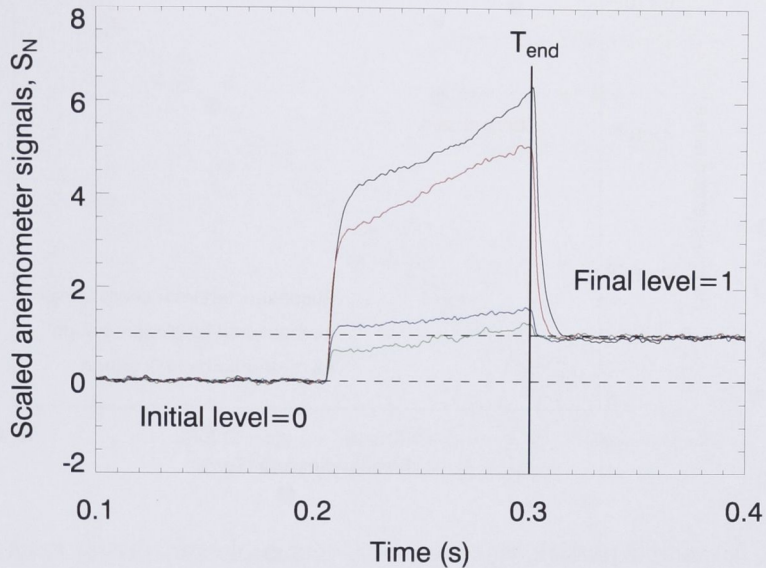


Figure 5.7: A sample shot showing four channels of anemometry data

$$S(t) = \beta(\Gamma_{th}(t)\pi + \Gamma_{beam}(t)) \quad (5.5)$$

In equation 5.5, we have combined several physical constants (including the energy transferred from the wire per incident particle, the resistivity of the wire and its projected area) into a single constant  $\beta$ . Equation 5.5 is only valid if the same amount of energy is transferred during a collision (between a particle and the wire) for the two components (directed and background). Since the transfer of energy is proportional to the temperature difference between the wire and the incident particle, this condition is only satisfied if the difference in temperature between the two gas components is much less than the difference between their mean temperature and the temperature of the wire. The background gas is in thermal equilibrium with the vacuum vessel so can be assumed to be at room temperature while the theoretical beam temperature at the nozzle exit is around 30K. Both the beam and background temperatures, as well as their difference, are substantially lower than the wire temperature of  $\sim 1300\text{K}$ .

To eliminate the unknown constant  $\beta$  we use the relation  $S(t_\infty) = \pi\beta\Gamma_{th}$  between the post-pulse signal and the thermal flux at time  $t_\infty$ . The thermal flux is given by  $(P_\infty/kT_{room})\langle v\rangle/4$  where  $P_\infty$  is the post pulse tank pressure and  $\langle v\rangle$  is the mean background particle thermal speed. For the signal at the end of the pulse we can

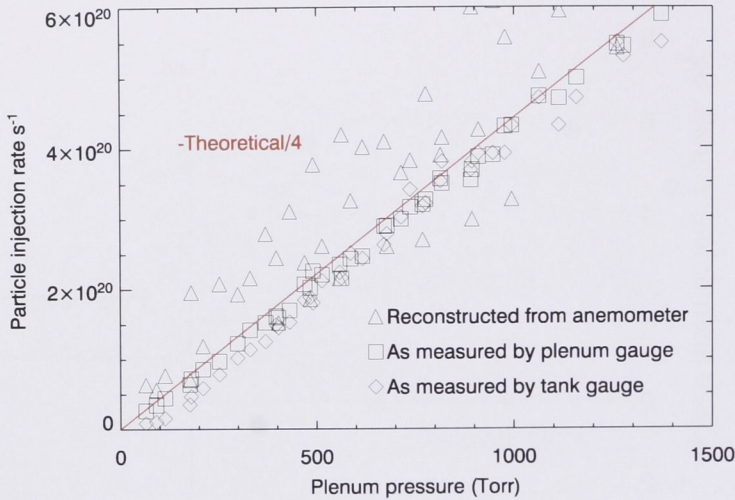


Figure 5.8: Measured particle injection rate versus plenum pressure. A line showing a quarter of the theoretical injection rate is over-plotted showing a deficit in the number of particles injected due to the deviation in behaviour from ideal isentropic flow

then write the beam flux as

$$\Gamma_{beam}(t_{end}) = \frac{\pi P_{\infty} \langle v \rangle}{4k_B T_{room}} \left( \frac{S(t_{end})}{S(t_{\infty})} - 1 \right) \quad (5.6)$$

where  $k_B$  is Boltzmann's constant. The signal shown in figure 5.7 is the normalised signal  $S_N(t) = S(t)/S(t_{\infty})$ , which is proportional to the total flux to the wire. The above expression allows the system to be calibrated on a pulse by pulse basis against the thermal signal arising from the (measured) background pressure,  $S(t_{\infty})$ .

### 5.3.2 Particle injection rate calibration

Following a gas pulse, the total gas efflux is obtained by independent measurements of the pressure changes in the plenum and in the test tank (monitored by a Convectron gauge). The variation of helium particle injection rate with plenum pressure for the 0.35mm nozzle is shown in figure 5.8.

The figure shows that the nozzle can achieve particle injection rates up to  $6 \times 10^{20} \text{s}^{-1}$  at a plenum pressure of 1500 torr. There is, however, a systematic discrepancy between the measured values and the theoretical values presented in section 5.2 of a factor of 4. This may be due to lateral shocks present in the flow field in the expansion region of the nozzle or due to the complex nature of the flow of the gas past the valve seal as it enters the nozzle.

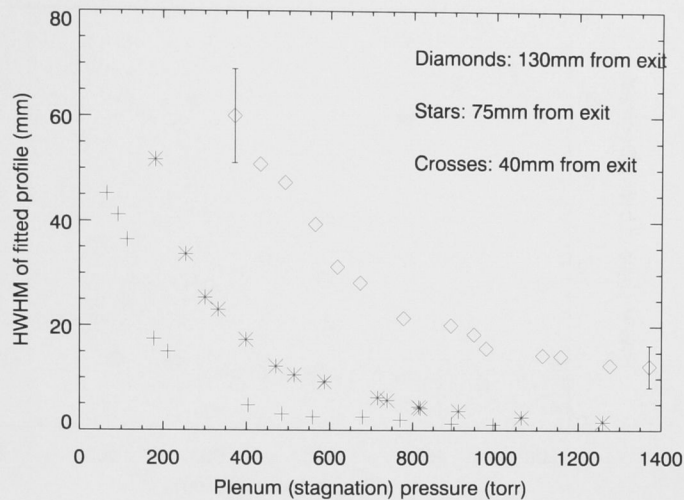


Figure 5.9: The Half Width at Half Maximum of the fitted Lorentzian to the scaled data as a function of plenum pressure. Typical error bars are shown.

### 5.3.3 Profile measurements

A primary design objective for the injection system is to maximise the fraction of particles that cross the LCFS, thereby minimising spillage into the rest of the vacuum vessel. To confirm that this is the case we have measured the width of the beam as it expands into vacuum using the CTA wire array. Figure 5.9 shows the half width at half maximum (HWHM) of the best fit Lorentzian as a function of plenum pressure and distance from the nozzle exit. At higher plenum pressures, and therefore smaller beam widths, the beam is spatially under-sampled, as can be seen by the convergence of the 75 and 40mm sets of data at higher plenum pressures to 0.4cm which is approximately half the inter-channel. Using interpolated results from figure 5.9 we calculated the angle of the HWHM of the beam. Figure 5.10 shows an almost linear dependence of HWHM angle on plenum pressure between 250 and 1000 torr.

To obtain an indication of  $N_p$  from the anemometer results we integrated a triangular profile with the same peak and HWHM as our Lorentzian fits. The results are over-plotted on figure 5.8 and, although exhibiting a larger scatter, show good agreement with the gauge results.

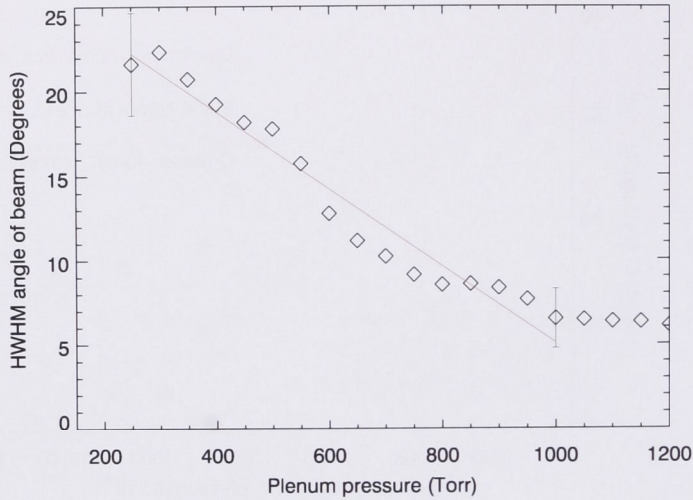


Figure 5.10: The observed half width at half maximum angle of the beam showing a linear dependence on the plenum pressure between 300 and 1000 torr. Typical error bars are shown.

### 5.3.4 Velocity measurements

The beam velocity was measured by applying a small sinusoidal modulation to the flux from the nozzle and measuring the phase of the modulation as a function of distance from the source. This is a difficult measurement as the response time of the piezo valve and drive electronics ( $\sim 5$ ms) sets an upper limit on the modulation frequencies which can be used. To improve the accuracy of the measured phase lag we have taken the average of 15 independent phase measurements at each nozzle-anemometer separation. However, meaningful results were only achieved at relatively high plenum pressures (greater than 1000 torr). The anemometer signals,  $S(t)$ , were filtered to isolate the modulation frequency and the instantaneous phase was extracted using

$$\phi(t) = \arg(s_a(t)) \quad (5.7)$$

where  $s_a(t)$  is the analytic signal of  $S(t)$  and is given by

$$s_a(t) = S(t) + i\hat{s}(t) \quad (5.8)$$

where  $i = \sqrt{-1}$  and  $\hat{s}(t)$  is the Hilbert transform of  $S(t)$ . The instantaneous phase of the modulated valve drive signal is then subtracted and then averaged over the pulse to return the mean phase difference between the anemometer and driver modulation. Figure 5.11 shows the phase difference between the valve drive voltage and the observed flux perturbation (measured by the CTA) as a function of distance from

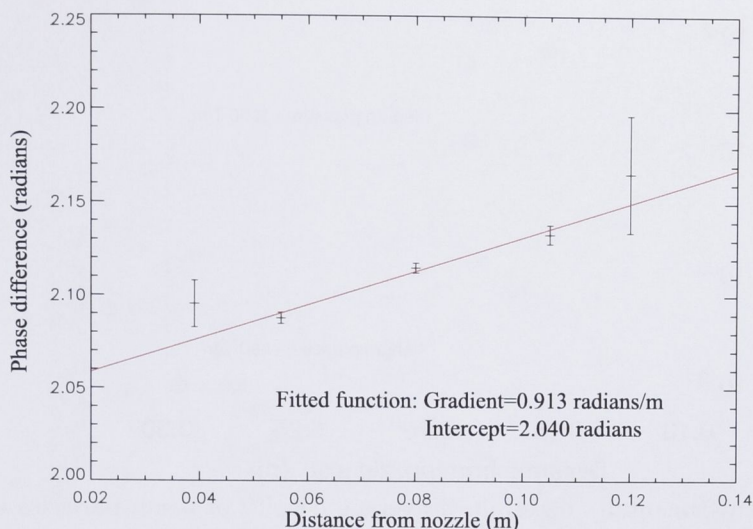


Figure 5.11: The phase difference between the modulation on the valve drive voltage and the observed modulation on the anemometer signals as a function of distance from the nozzle

the nozzle throat at 1000 torr plenum pressure. By treating the perturbation as a travelling wave the phase,  $\phi(x)$ , observed by the CTA as a function of distance,  $x$  is given by

$$\phi(x) = \frac{2\pi x}{v_{beam}} f_{mod} \quad (5.9)$$

where  $f_{mod}$  is the modulation frequency of flow and  $v_{beam}$  is the beam velocity. By fitting a line to the data in figure 5.11 we estimate the beam velocity as  $690 \pm 75$  m/s. This is lower than the theoretical value for the exit velocity of 1720 m/s but is consistent with a lower injection rate. The theoretical exit temperature of the flow (30K) gives an estimate of the local sound speed at the nozzle exit of 321 m/s which gives an inferred flow Mach number is  $2.1 \pm 0.23$ . Finally, by using the HWHM angle of the beam from figure 5.10 and the particle injection rates and velocity (figure 5.8 and figure 5.11) it is possible to calculate the average particle density as shown in figure 5.12.

Using the measured beam velocity and the estimated thermal velocity (at 30K) perpendicular to the beam gives a rough estimate of the thermal expansion half angle of  $\sim 20$  degrees, which is greater than our measured HWHM as shown in figure 5.10. This is not an unreasonable estimate given the uncertainties involved.

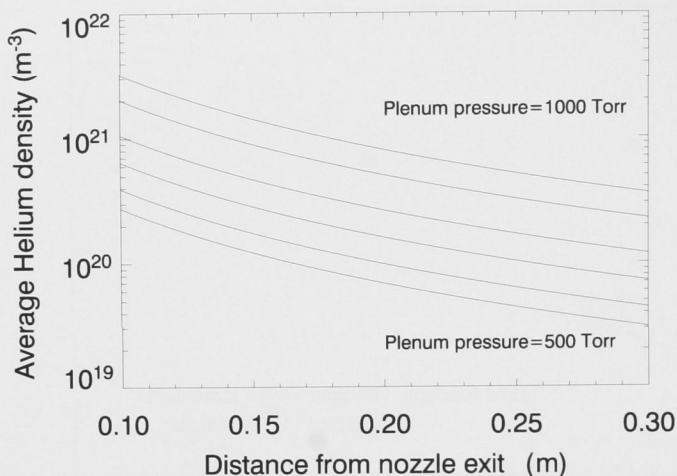


Figure 5.12: Experimentally determined average density of beam particles as a function of distance from the nozzle and plenum pressure. Lines are plotted in 100 torr increments.

## 5.4 Interaction with the plasma

There are two related but distinct mean free paths relevant to the interaction of the beam with the plasma: the penetration of electrons transverse to the beam (parallel to the magnetic field, figure 5.13) and the penetration of helium atoms through the plasma (figure 5.14).

Using the ionisation cross sections for helium obtained from [Kim & Rudd, 1994] we have calculated the mean free path of plasma electrons through the gas jet for a variety of electron energies. As can be seen in figure 5.13 the smallest electron mean free paths, which are of the order of the width of the gas jet in the plasma, occur at electron energies of around  $\sim 75$  eV (H-1NF core  $T_e \approx 100$ -150eV). Therefore the helium beam should be ionised uniformly in the direction transverse to its path and will not be subject to the shielding effects described in [Song et al., 2000].

The electron impact ionisation frequency and the velocity of the beam atoms can be used to estimate the mean free path ( $\lambda_b$ ) of supersonic helium atoms across the plasma slab. The mean free path is given by

$$\lambda_b = \frac{v_b}{n_e \langle \sigma_{iz} v \rangle_e} \quad (5.10)$$

where  $n_e$  is the electron density,  $v_b$  is the directed velocity of the beam and  $\langle \sigma_{iz} v \rangle_e$  is the rate coefficient for impact ionisation given by

$$\langle \sigma_{iz} v \rangle_e = \int \sigma_{iz}(v) v f_e(v) dv \quad (5.11)$$

where  $f_e(v)$  is the normalised isotropic Maxwellian velocity distribution function for the electrons.

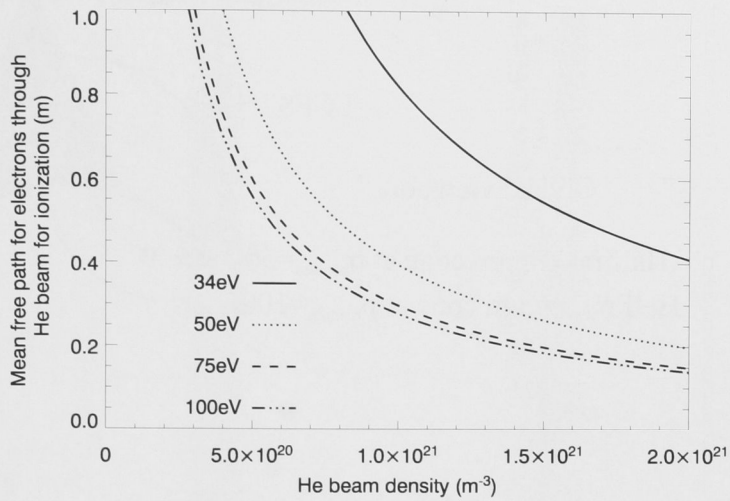


Figure 5.13: Mean free path of mono-energetic electrons for ionising collisions in the helium beam for a variety of electron energies

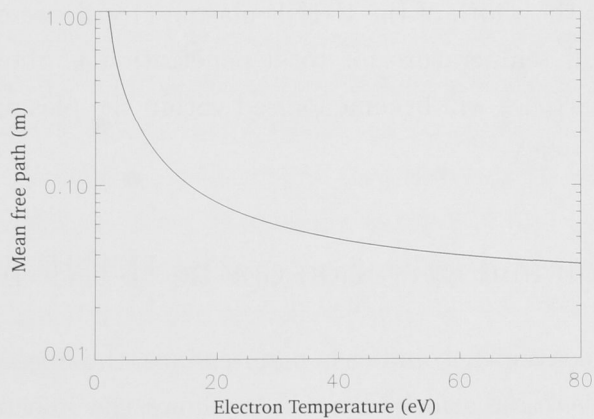


Figure 5.14: Mean free path ( $\lambda_b$ ) for supersonic helium neutral particles travelling at a velocity of 690m/s through a plasma slab of density  $1 \times 10^{18} m^{-3}$

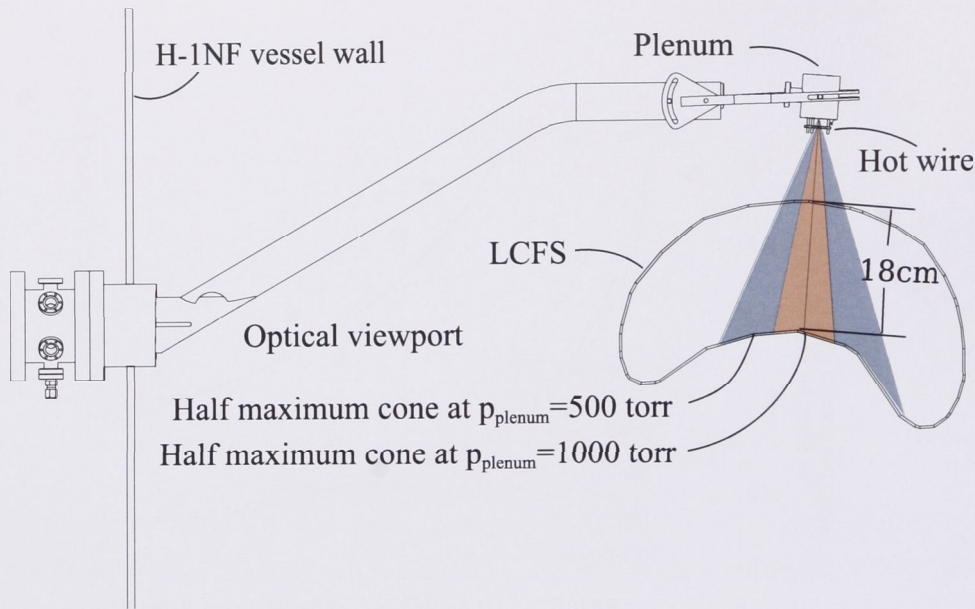


Figure 5.15: The re-entrant arm used to mount the injection system in the H-1NF vessel. The mount includes a optical view port where diagnostics get a clear view of where the supersonic beam intersects the plasma

This is plotted in figure 5.14, using the measured beam velocity,  $v_b$  (obtained in section 5.3.4 as 690m/s), and  $n_e=1 \times 10^{18}m^{-3}$ . Where the electron temperature is below the ionisation energy the bulk of the electrons pass through the helium beam without making an ionising collision. As a result the penetration depth of the supersonic beam increases rapidly when the electron temperature falls below 20eV. Taking into account the width of the H-1NF plasma (18cm) we can see from figure 5.14 that the critical temperature for total penetration is about 9eV. Therefore most of the beam particles will become ionised within the plasma for bulk electron temperatures above  $\sim 9eV$ .

## 5.5 Installation and operation on the H-1NF heliac

For operational convenience and easy maintenance, the injection system is fixed at the end of a re-entrant arm. Figure 5.15 shows the injector installed inside the H-1NF vacuum vessel in relation to a representative magnetic flux surface. The range of injection angles shown in figure 5.10 is overlaid on the plasma cross-section. Even at low plenum pressures most of the beam flux intersects the last closed flux surface. First experiments using the supersonic injection system were carried out using a target plasma which was produced using a low static fill of  $0.17 \times 10^{18}m^{-3}$

helium and  $0.28 \times 10^{18} \text{m}^{-3}$  hydrogen (atoms). The magnetic configuration used had an on-axis rotational transform of 1.12 and a magnetic field of 0.5 Tesla. To generate

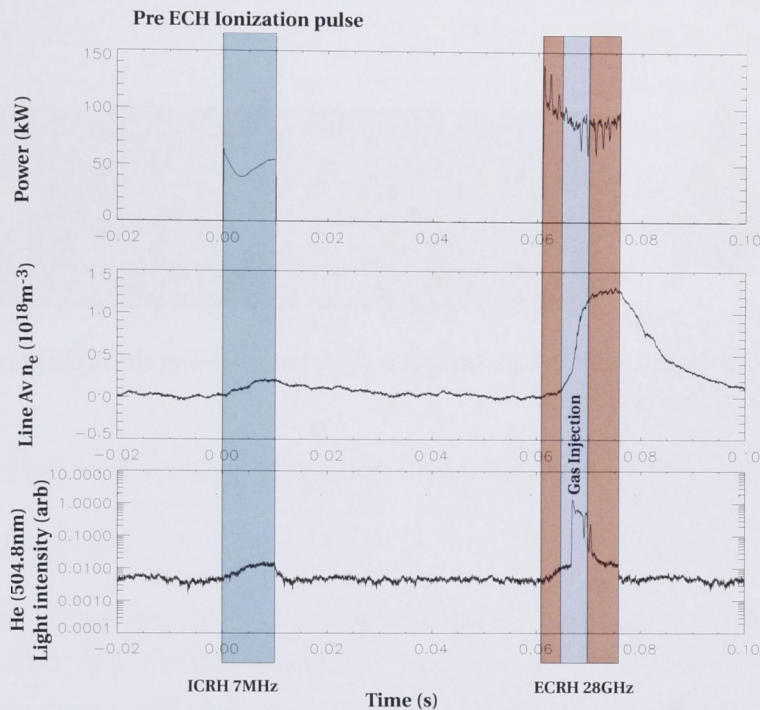


Figure 5.16: Traces of the heating power, electron density and helium light emission from a resonantly heated plasma in the H-1NF vessel at 0.5 Tesla

sufficient background electrons for the 28GHz 2nd harmonic Electron Cyclotron Heating (ECH) discharge breakdown a pre-pulse low density plasma is generated using 50kW of radio frequency power at the fundamental ion cyclotron frequency of 7MHz. Forty milliseconds later the  $\sim 100$  kW single pass ECH is initiated as shown in figure 5.16 and 2 milliseconds after that a trigger pulse is sent to the injection system. After a mechanical delay of 3ms, gas is injected into the plasma at a rate of  $1 \times 10^{20} \text{s}^{-1}$ . The third panel in figure 5.16 shows the time resolved line-of-sight integrated emission from the helium 504.8nm ( $5^1\text{S} \rightarrow 2^1\text{P}$ ) line. The sudden brightness increase appears as the helium gas enters the plasma and is excited by the initially hot electrons (estimated to be 80eV [Michael & Howard, 2004]). Figure 5.17 shows the two dimensional line integrated raw light images obtained using a Hamamatsu framing streak camera [Hamamatsu, 1999] through the optical view port shown in figure 5.15 for a similar discharge. The first frame shows the geometry of the injection with respect to the magnetic (or plasma) axis. The following frames show the emission (corrected for vignetting) as the injected gas enters the plasma.



Figure 5.17: Raw light images, corrected for vignetting, taken through the optical view port as the injection was initiated.

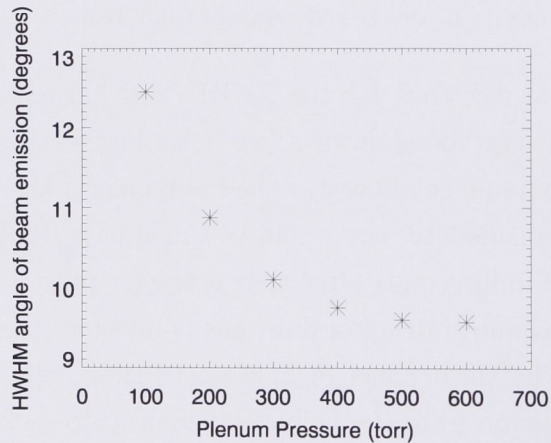


Figure 5.18: The variation of the width of the observed intensity increase versus the plenum pressure in the injection system

Figure 5.18 shows the full width at half maximum angle of the intensity profile. The intensity profile is a non linear function of the electron density and temperature (both of which vary across the profile) as well as the helium beam properties so is not a direct measure of the beam profile. Figure 5.18 does, however, show a decrease in angle with an increase in pressure. Estimation of the perturbative effect of gas injection on the plasma requires further experimental data. Initial results obtained using helium line ratio techniques indicate that the injection at more than  $1 \times 10^{20} \text{s}^{-1}$  causes the electron temperature to rapidly drop. However, as the mean free path of the beam increases with decreasing temperature (figure 5.14), once the temperature drops the plasma becomes increasingly transparent to the beam, limiting the effect on the plasma density. This subject has not yet been studied in detail.

## 5.6 Predicted fuelling using a time dependent CRM

### 5.6.1 Slab model

In section 4.6 we showed that modelled helium brightness obtained using time dependent CRM (TD CRM) agreed very well with experimentally determined results. We can use the TD CRM, along with experimentally determined  $n_e$  (using ELSI, section 2.1.2) and  $T_e$  (using the HLR/HBD system) profiles, to predict the populations of the states of helium in the DISH beam as it propagates through the plasma. And from the rate of ionisation from all states,  $S(i)$ , in figure 3.1 we can determine the rate of ionisation of the beam.

To examine the effect that multi step ionisation has on the validity of the simple penetration depths predicted in figure 5.14 we used the TD CRM to propagate a collimated beam (ignoring the expansion of the beam) through a slab plasma (temperature and density do not vary as a function of distance into the slab). The model was run for a range of  $T_e$  at a constant  $n_e$  of  $1 \times 10^{18} \text{m}^{-3}$ .

Figure 5.19 shows the density of all neutral states (calculated as  $n_a(x) = n_{1s}(0) - n_i(x)$  where  $n_{1s}(0)$  is the density of the ground state and at  $x = 0$  and  $n_i(x)$  is the ion density) as a function of distance into the slab. The density of the beam shows an exponential decay with the decay length,  $l_d$  decreasing with increasing  $T_e$ . By fitting an exponential curve to the individual density profiles we can determine  $l_d$  which gives a measure of the mean free path for ionisation of the neutral states of helium into the plasma. Figure 5.20 shows  $l_d$  as a function of  $T_e$  (points) plotted over the previously determined simple penetration depth for helium neutrals (from figure 5.14).

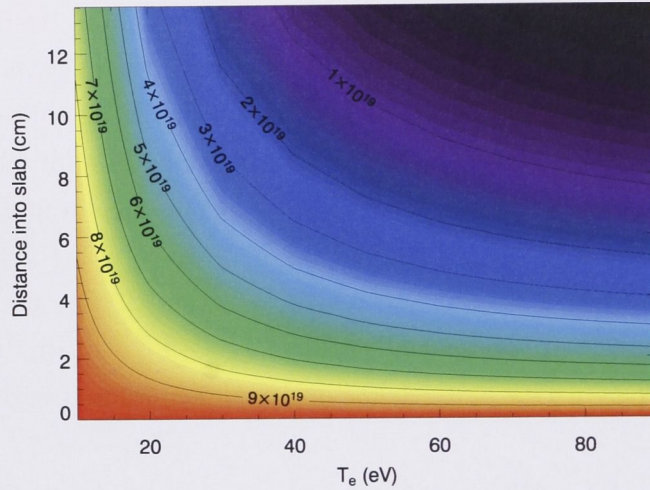


Figure 5.19: Density of all neutral states of helium (contour intervals in  $m^{-3}$ ) calculated using the TD CRM as a function of  $T_e$  and distance into the slab at a constant density of  $n_e = 1 \times 10^{18} m^{-3}$

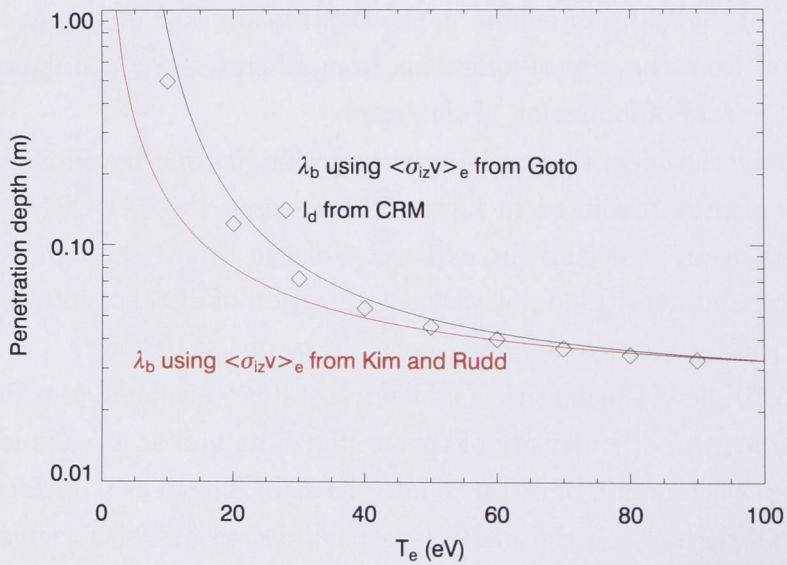


Figure 5.20: Decay length,  $l_d$ , of the combined populations of neutral helium as a function of slab electron temperature ( $n_e = 1 \times 10^{18} m^{-3}$ ) compared with mean free paths calculated using equation 5.10

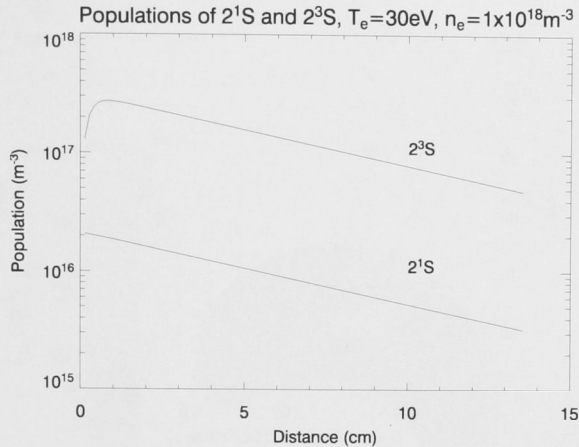


Figure 5.21: Densities of the helium metastable states  $2^1S$  and  $2^3S$  as a function of distance into the slab for an injection density of  $n_0 = 1 \times 10^{20} \text{m}^{-3}$ .

Figure 5.20 shows a longer penetration depth at lower  $T_e$  for the CRM than the result of equation 5.10 (shown in red). The black curve is based on equation 5.10 but with the rate coefficients for ionisation used in the TD CRM. Across the range of  $T_e$  there is only a small difference between the single step ionisation model and the multi step as modelled by the TD CRM. The collision rate for a beam particle as it traverses the plasma can be derived from equation 5.10 as

$$\nu = n_e \langle \sigma v \rangle \quad (5.12)$$

where the angular brackets indicate an average over the distribution function and  $\sigma$  is the cross section of the interaction we are studying (eg electron impact ionisation or excitation). This can be approximated as

$$\nu \approx n_e \sigma v_{th} \quad (5.13)$$

where  $v_{th}$  is the average electron thermal velocity. Most cross sections have a maximum value in the range  $0.1 \rightarrow 0.3 \text{\AA}^2$  which gives a collision frequency of  $5 \rightarrow 10 \text{kHz}$  or a time between collisions of  $60 \rightarrow 180 \mu\text{s}$ . This is far longer than the lifetime of most excited states of less than  $100 \text{ns}$ . Metastable states (eg  $2^1S$  and  $2^3S$ ) can have lifetimes of many milliseconds [Van Dyck et al., 1971]. However, as shown in figure 5.21 their populations are only a very small fraction of the ground state. This is mainly due to the very large ionisation rate coefficient for ionisation from the metastable levels. These results show that multi-step ionisation only plays a small part in the plasma beam interaction.

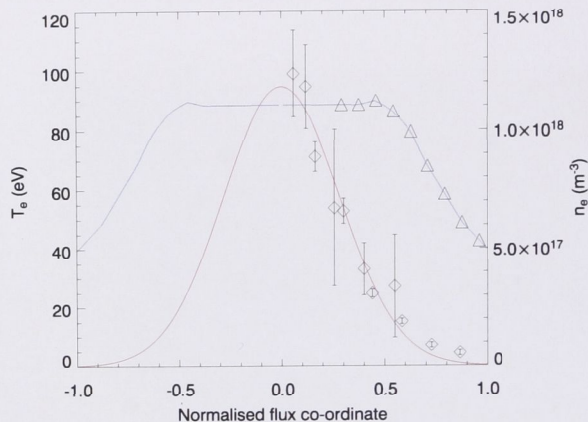


Figure 5.22: The  $T_e$  profile with a Gaussian fit and interpolated  $n_e$  profile that will be used in the modelling of the DISH fuelling profile using the TD CRM

### 5.6.2 Model using experimentally determined $T_e$ and $n_e$ profiles

To understand the interaction between a fuelling molecular beam and the plasma at the DISH cross section we used the TD CRM to propagate a “DISH” like beam into a model plasma. To obtain a functional form for the  $T_e$  profile we fitted a Gaussian curve ( $T_e(r) = A_0 e^{-A_1 r^2}$ ) to typical  $T_e$  data obtained using the HBD. Figure 5.22 shows the temperature profile as well as the best fit curve in normalised flux co-ordinates. The electron density curve was obtained by interpolating the tomographically inverted data from ELSI (section 2.1.2).

Using the technique presented in section 4.3 we then re-mapped the  $T_e$  and  $n_e$  profiles to the cross section of DISH. Figure 5.23 shows the re-mapped density profile in cartesian co-ordinates as well as the axis of injection of the DISH device. The profile shown, which is typical the  $T_e$  profiles measured in chapter 4, shows a hot (100eV) core quickly dropping to a cold ( $T_e < 30\text{eV}$ ) edge. Results presented in this section will be plotted along the co-ordinate axis  $S$  which is the position along the injection axis shown in figure 5.23 with the origin at the point where the axis crosses the plasma boundary (as defined by the LCFS from the Gourdon interpolation code).

The  $T_e$  profile was scaled to a number of different values of  $\langle T_e(S) \rangle$  which is the average electron temperature along the injection axis. These  $T_e$  profiles, along with the  $n_e$  profile shown in figure 5.22, were used as inputs to the TD CRM. The (DISH) beam parameters used were  $n_0 = 1 \times 10^{20} \text{m}^{-3}$  with a beam radius of  $r_b = 4.3 \text{cm}$ . These are characteristic for a beam produced by DISH at a plenum pressure of

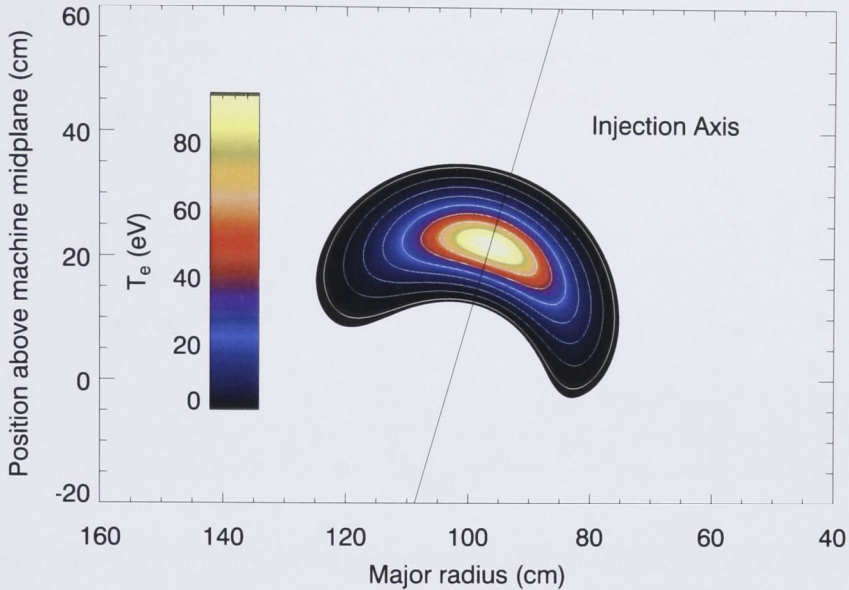


Figure 5.23: Modelled injection geometry showing the  $T_e$  profiles used as an input to the TD CRM code as well as contours (white) at regularly spaced normalised flux co-ordinate

500 torr for the system presented in this chapter. In this simple model, the beam is considered to be one-dimensional. Since particles that propagate above or below the magnetic axis see a reduced  $T_e$  and  $n_e$  profile, the plasma transparency (equation 5.16) will be under estimated.

The TD CRM does not take into account the confining affect of the magnetic field when calculating ion densities generated by impact ionisation of the DISH beam. Rather it assumes that ions propagate along with the injection giving a strictly increasing (recombination is negligible in these conditions) ion density referred to as  $n_i^{(model)}$ . The number of ions generated at a particular  $S$  is the change in  $n_i^{(model)}$ , and using the velocity of the beam,  $v_b$ , and beam radius we can calculate the deposition profile (in  $m^{-1}s^{-1}$ ) as

$$N_{dep}(S) = \pi r_b^2 v_b \frac{dn_i^{(model)}}{dS}. \quad (5.14)$$

An example deposition profile is shown in figure 5.24. Figure 5.25 shows the ion deposition profile as a function of peak  $T_e$  and position along the injection axis ( $S$ ). As the temperature of the plasma increases the peak in the deposition profile moves from the centre (as indicated by the line in the figure) towards the edge of the plasma.

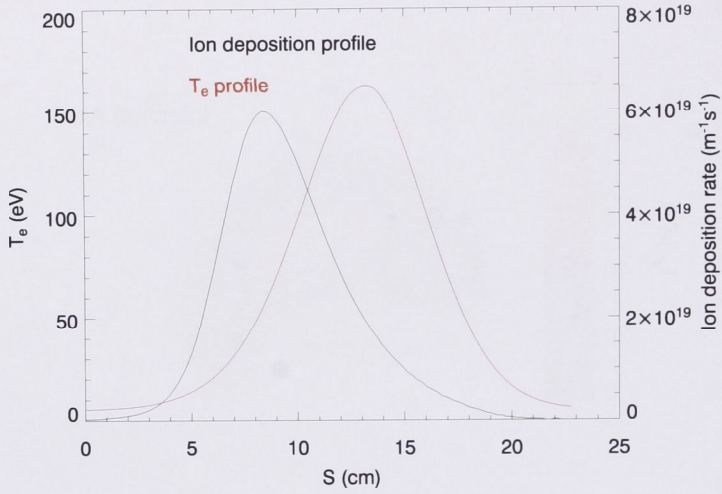


Figure 5.24: Particle deposition profile along the DISH injection axis calculated using a TD CRM.

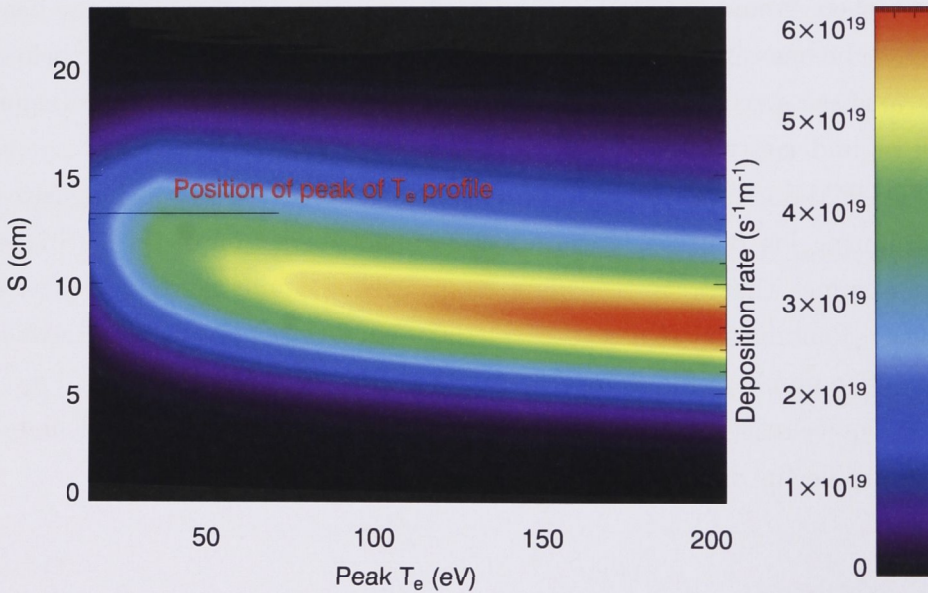


Figure 5.25: Deposition of ions from the DISH beam calculated using a TD CRM. The peak in the profile moves outwards with increasing temperature as the fuelling moves from the core to the edge.

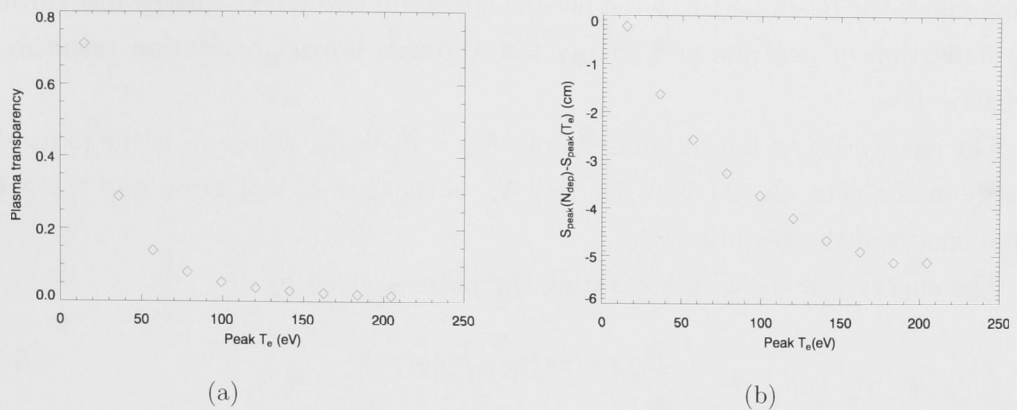


Figure 5.26: (a) The transparency,  $P$ , of the plasma to the DISH beam as a function of average electron temperature across the DISH injection axis. (b) The position of the peak in injection rate,  $N_{dep}$ , relative to the peak in  $T_e$  (which is on the magnetic axis).

One of the goals of the DISH project was to design a device to selectively fuel the plasma. A key parameter we can calculate from the TD CRM output is the transparency of the plasma (ie the fraction of the beam that is ionised). The transparency,  $P$ , is given by

$$P = \frac{N_{dep}}{N_p} \quad (5.15)$$

$$= \left( \int N_{dep}(S) dS \right) / \pi r_b^2 v_b n_0 \quad (5.16)$$

where  $N_p$  is the particle injection rate and  $n_0$  is the beam number density at the plasma edge. Figure 5.26(a) shows  $P$  as a function of  $S$ . Since we take the approximation that the beam is collimated and goes through the centre figure 5.26 represents an upper limit on  $P$ . Figure 5.26(a) shows that as the temperature of the profile increases the transparency decreases. These results show that for mean electron temperatures above 40 eV (which corresponds to a peak  $T_e$  of 100 eV) only a very small portion ( $P < 5\%$ ) of the beam particles pass all the way through the plasma. Figure 5.26(b) shows the difference between the positions of the peak in the  $T_e$  and particle deposition rate,  $N_{dep}$ , profiles as a function of average electron temperature. The figure shows that as the temperature of the profile increases the peak in the deposition profile shifts from being in the centre of the plasma to being on the outboard (closest to the injector) edge of the plasma. This shows that as the H-1NF plasma tends towards higher temperatures the system will tend towards an edge fuelling device.

To gauge the potential of DISH as a fuelling tool we also need to gauge the perturbative effect of the beam on the plasma. Aside from the addition of a cold ion

component, the beam perturbs the plasma energy in two ways: Energy lost through the ionisation of neutrals and energy lost through impact excitation resulting in radiative loss.

The energy lost to ionisation is simply  $E_{iz} = E_i N_{iz} t_{pls}$  where  $E_i$  is the ionisation energy of the neutrals (24.58eV for He)  $N_{iz}$  is the rate of ionisation and  $t_{pls}$  is the pulse length of the gas injection.

The energy lost to radiation during the pulse is given by

$$E_{rad} = \pi r_b^2 t_{pls} \int \rho_P(r) dr \quad (5.17)$$

where  $\rho_P(r)$  is the power density radiated through atomic transitions (joules per second per cubic metre) and is given by

$$\rho_P(r) = \sum R_k(r) E_k \quad (5.18)$$

$$= \sum R_k(r) \frac{ch}{\lambda_k} \quad (5.19)$$

where  $c$  is the speed of light,  $\lambda_k$  is the wavelength of the photon emitted by the transition  $k$ ,  $R_k(r)$  is the rate density (events per second per cubic metre) of the transition  $k$  and  $h$  is Plank's constant. We take the sum over 15 different transitions which (typically) have the highest average  $R_k$ . Many of these transitions radiate in the ultra violet region of the electro-magnetic spectrum ( $\lambda_k = 51 \rightarrow 58\text{nm}$ ) and involve a transition to the ground state ( $n^1P \rightarrow 1^1S$  where  $n=1$  to 6). In fact over 70% of the radiative losses occur through these transitions. This is due not only to these transitions having a high  $R_k$  but also due to the high energy of the transition and hence the photon.

Figure 5.27 shows the energy loss from the plasma electrons to ionisation and radiation as a function of peak  $T_e$  for a  $t_{pls} = 5\text{ms}$  pulse from DISH. Also shown is an estimate of the stored energy in the plasma electrons which is given by

$$E_{st} = \frac{3}{2} k_B \int_V n_e(\mathbf{r}) T_e(\mathbf{r}) d\mathbf{r} \quad (5.20)$$

$$= \frac{3}{2} k_B \int n_e(S) T_e(S) \pi l r dr \quad (5.21)$$

where  $r = r(S)$  is the radius of the cylindrical co-ordinate and  $l$  is the length of the plasma which is chosen to give the cylindrical approximation the same volume as the H-1NF plasma ( $1\text{m}^3$ ). The energy lost from the plasma to ionising the beam and radiation through electron impact excitation of neutral helium increases with average temperature but plateaus as the beam becomes fully ionised. It should be

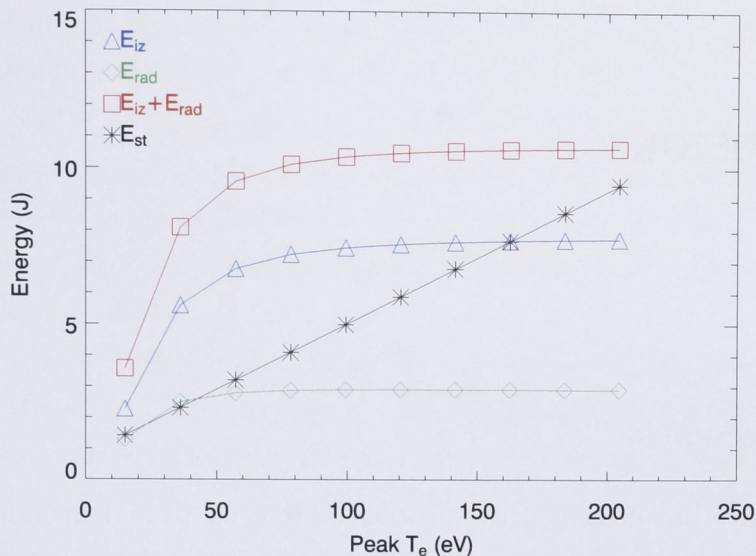


Figure 5.27: The stored electron energy ( $E_{se}$ ), the energy lost by electron impact excitation through radiation ( $E_{rad}$ ) and ionisation ( $E_{iz}$ ) as a function of average electron temperature for beam conditions characteristic of a DISH pulse of 5ms at 500 torr.

noted that there are other channels of energy loss caused by beam injection, notably radiation from  $\text{He}^+$  and, at higher temperature, double ionisation of helium. As discussed in section 4.2 the electron energy confinement time is  $\sim 0.4\text{ms}$  leading to a low stored energy for the input power being used. This means, at current DISH fuelling rates, the beam will strongly perturb the energy balance of the plasma. What is required is a nozzle which will produce a lower flux for injection. As part of his MPhil thesis Ben Powell [Powell, 2006], using some of the techniques developed in this thesis has designed and characterised a nozzle with a diameter of 0.19mm which produces fluxes from  $1$  to  $5 \times 10^{20}\text{s}^{-1}$  (for 250 to 1200 torr plenum pressure) which will be more suited to the H-1NF stored energy requirements.

# Conclusions

## 6.1 Outcomes

This thesis has described the process leading up to and including the development of a directional injection system on the H-1NF heliac for the fuelling of resonantly generated plasmas.

This process began with an interferometric study of the evolution of the electron density profile for resonantly heated plasmas. We discovered that the formation of these plasmas depends strongly on the location of the  $\omega = \omega_{ci}$  layer in the plasma. As the ion-ion hybrid layer ( $\omega_{ii} = \omega$ ) is located outside the plasma boundary we propose that ion minority heating is not the mechanism for plasma generation and heating. Nevertheless there is a strong correspondence between the efficiency of plasma generation and the position of fundamental hydrogen ion cyclotron resonance. It was also found that the presence of low order rational surface at the edge of the plasma suppresses plasma formation. We observed that, during a combined electron and ion resonantly heated plasma, the plasma was being fuelled through thermal diffusion from the background gas inventory. Following this discovery it was decided to design, test and install a directional gas injection system for localised fuelling of the H-1NF plasma.

The interaction between a gas injection device and the H-1NF plasma can only be understood with a knowledge of the temperature profile. Therefore, as part of the work towards designing the device, we installed a diagnostic helium beam which was designed and characterised by Daniel Andruczyk and Brian James at the University of Sydney. An optical system was designed and installed to view the emission of the beam at dual wavelengths, which enabled, using a CRM, the measurement of electron temperature using helium line ratios. Expanding upon Daniel's work we performed a study of the behaviour of the beam using multiple, rapid pulses. We found an optimal set of parameters for multi-pulse operations suited to an ECH

discharge on H-1NF. The combination of a multi-pulse HBD and a well calibrated and aligned set of viewing optics has enabled the first time and radially resolved spectroscopic determination of  $T_e$  on the H-1NF heliac.

Combining the HLR measurement of  $T_e$  with the interferometric measurement of  $n_e$  allowed us to determine the electron pressure profile of a typical ECH plasma and the stored electron energy which, in turn, allowed us to estimate the electron energy confinement time at  $0.4 \pm 0.15$  ms and the electron beta (ratio of plasma to magnetic pressure) at 0.01%.

Using a time dependent CRM we were then able to model the propagation of the HBD into the plasma and compare the simulated emissivity profiles with the measured profiles. Modest perturbation of  $T_e$  from the observed profile indicates a relatively sensitive dependence of the emission brightness on the  $T_e$  profile.

Using the isentropic flow relations we designed the directional injection system for H-1NF (DISH) using a double conical (de-Laval) nozzle with an 0.35mm diameter throat. The system was then installed in a test tank and the particle injection rate was measured as a function of plenum pressure. Using constant temperature anemometry we determined the range of cone angle of the jet produced by the system. After careful characterisation we determined that, for plenum pressures ranging from 500 to 1000 torr the system produces injection rates from  $2 \times 10^{20}$  to  $4 \times 10^{20} \text{s}^{-1}$  and cone angles from 15 to 7 degrees.

By measuring the phase of a sinusoidal perturbation in the gas flow at several positions we were able to determine the velocity of the flow to be  $690 \pm 75$  m/s which gives an inferred flow Mach number of  $2.1 \pm 0.23$ . Using a simple model of beam penetration we determined that for electron temperatures above 20eV the majority of the helium beam will be ionised by the plasma, achieving our goal of predominantly fuelling the plasma and avoiding the fuelling of the background gas inventory. After determining that the TD CRM provides a good model of neutral plasma interaction we used it to propagate a beam similar to the jet of gas produced by DISH into a model plasma based upon the findings of chapter 4. We confirmed the validity of the simple penetration model and showed that multi-step ionisation only plays a small role in the fuelling of the plasma. We then examined the ion deposition profile and calculated the transparency of the plasma to the beam as a function of electron temperature.

We concluded the body of the thesis by using the TD CRM to examine the energy lost from the plasma to electron impact interactions with the beam (both ionisation and excitation). We discovered that, even though the nozzle will meet

n	$\lambda_{ex}$	$\lambda_{fl}$	Suitable E
3	504nm	668nm	$\sim 1000$ V/cm
4	397nm	492nm	$\sim 250$ V/cm
5	362nm	439nm	$\sim 40$ V/cm
6	345nm	414nm	$\sim 10$ V/cm

Table 6.1: A table of candidate transitions for LIF E-field measurements and their suitable E-field ranges

the fuelling requirements for H-1NF, it will significantly perturb the plasma electron energy balance and we recommend that the new, smaller diameter nozzle, designed by Ben Powell, be used for fuelling.

## 6.2 Future Work

As discussed throughout this thesis there are many areas that can be developed into future work and studies. For example a comparison between observed helium emissivities during DISH injection into the plasma and outputs from the TD CRM should be performed to validate the measurements in [Powell, 2006]. One of the difficulties in designing the optics for the HLR system was the registration and calibration of the individual cameras. Using mask at a common focal plane of two lenses a system could be devised to image the beam, in two colours, onto a single two dimensional CCD (charge coupled device) sensor. This has the advantages of higher spatial resolution and easier registration however issues with gas pulse synchronisation would need to be overcome. In the view of the author, however, the direction in which this project should proceed is in the direction originally intended for the HBD: laser induced fluorescent (LIF) measurements of electric fields.

### 6.2.1 Helium metastable populations and LIF E-field measurements

The importance of a measurement of the electric field in a fusion plasma can not be overstated. Through force balance the electric field profile is linked to poloidal rotation which has been linked to confinement properties and a transition to H mode in both tokamaks and stellarators [Punzmann & Shats, 2004].

The LIF E-field measurement first proposed in [Takiyama et al., 1993] involves directly exciting metastable helium (in the  $2^1S$  state) to the  $n^1P$  state where the principle quantum number,  $n$ , is chosen according to table 6.1. The stark mixing between the  $n^1P$  and  $n^1D$  state is dependent on the electric field. As the  $n^1D$  acts as the upper state for the transitions shown in table 6.1 the intensity

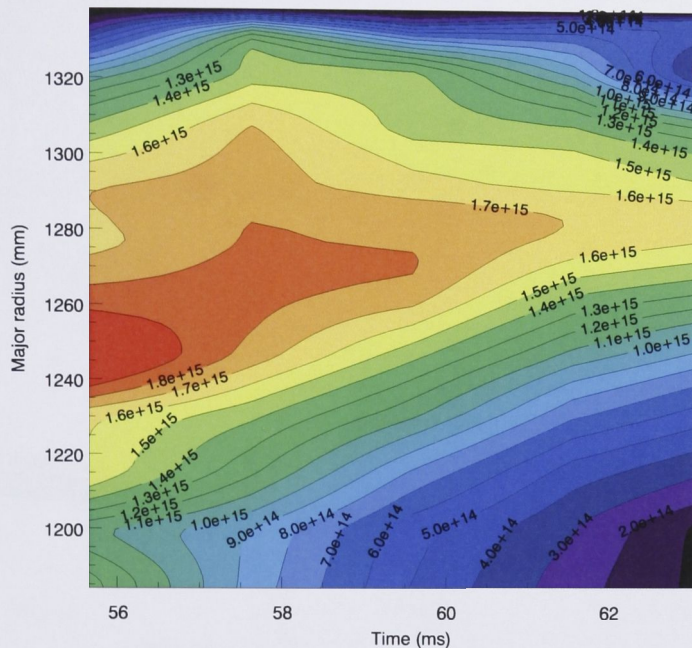


Figure 6.1: Density of the metastable  $2^1S$  state of atomic helium as a function of major radius and time for shot 61031

of the fluorescence will be proportional to the electric field. Figure 6.1 shows the density of the  $2^1S$  metastable state of helium as a function of major radius and time for discharge 61031 as calculated by the TD CRM (see section 4.6). According to [Xian-Ping et al., 2003] a metastable density of  $n_{2^1S} > 1 \times 10^{16} \text{m}^{-3}$  is required in order to detect the electric field. The maximum metastable densities of  $n_{2^1S} > 1.7 \times 10^{15} \text{m}^{-3}$  are already approaching the required levels even during a very conservative gas pulse designed to allow multi-pulse HLR measurements. By increasing the source pressure or decreasing the skimmer nozzle distance it should be possible to attain metastable densities sufficient for LIF measurements on H-1NF. Figure 6.2 shows the simplest set up for a LIF measurement. The geometry of the beam and viewing optics will remain the same and a YAG pumped dye laser will be reflected off a series of internal mirrors inside the H-1NF vessel and a final mirror will reflect the beam off the helical winding across the field of view of the optics. This set up would be suitable for the intensity based LIF measurement discussed in Takiyama's paper. However, as the emitted light is polarised perpendicular to the electric field  $\mathbf{E}$ , and the direction of  $\mathbf{E}$  is expected to be radial, a new viewing and injection system will need to be designed to exploit the polarisation to determine the strength of the electric field.

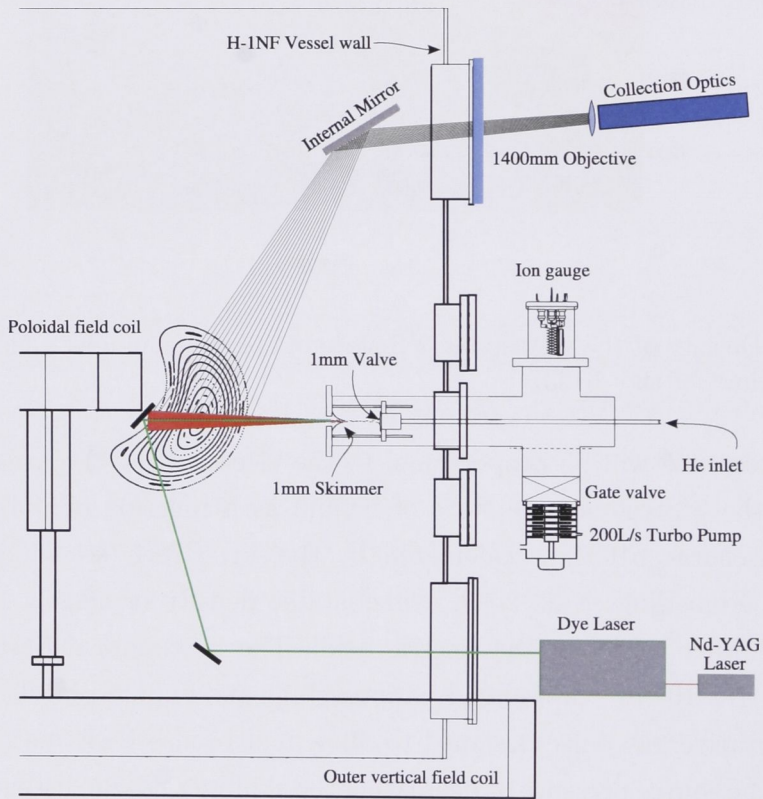


Figure 6.2: Proposed modification of the HLR system to enable the measurement of E-Fields using LIF

# Coherence imaging of helium ion temperatures

While quasi neutrality ( $n_e \approx$  the ion density,  $n_i$ ) means that a measurement of the electron density gives us a good approximation of  $n_i$  the same can not be said of the relationship between  $T_e$  and  $T_i$ . There are a range of  $T_i$  diagnostics in use at fusion facilities around the world. The bulk ion temperature can be measured using the energy spread of neutral (charge exchanged) particles hitting the vessel wall while the ion temperature spatial distribution can be imaged by active techniques such as charge exchange recombination spectroscopy using heavy ion beam probes or neutral beams.

Due to the relatively low electron temperature ( $>300\text{eV}$ ) in the H-1NF heliac light multi-electron atoms like helium do not become stripped of all their electrons so excitations of the remaining electron are still possible. When these excited electrons undergo a spontaneous transition to a lower state a photon is emitted. Given a collection of particles with a distribution of velocities photons collected by an imaging diagnostic will have a distribution of Doppler shifts. This means that, ignoring line integral effects and when  $\Delta\nu \ll \nu$ , the profile of emission line for an ion of mass  $m_i$  and temperature  $T_i$  would be broadened to a width  $\Delta\nu$  given by,

$$\Delta\nu = \nu_0 \sqrt{\frac{kT_i}{m_i c^2}} \quad (\text{A.1})$$

where  $k$  is Boltzmann's constant,  $\nu_0$  is the centre frequency and  $c$  is the speed of light. However we must take into account that the ion temperature is a profile across the plasma.

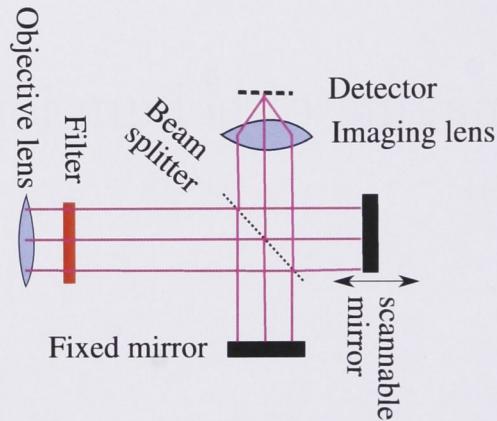


Figure A.1: Optical layout for a Michelson FTS.

## A.1 Coherence imaging

There are two techniques for the imaging of spectral line widths: using a grating spectrometer to disperse the light onto a two dimensional CCD array or using a Fourier transform spectrometer (FTS) to multiplex the coherence (line-shape) information into the temporal domain. Using a grating spectrometer involves the use of a slit on the input side to provide spectral resolution, this in turn reduces the light throughput of the system reducing the signal-to-noise and the accuracy of any measurement. Figure A.1 shows the optical layout for a simple FTS, a Michelson interferometer. Light is collimated by an objective lens and split into two arms, reflected off two mirrors and recombined on the splitter and focused by an imaging lens down onto a detector (or detector array). Essentially this optical arrangement interferes light with its self. For a monochromatic light source (that is perfectly coherent light source) the instrument can be scanned through either constructive or destructive interference by scanning one of the mirrors. When the light is made up of a range of frequencies distributed around a central frequency (quasi coherent light) such as an atomic (or ionic) emission line the instantaneous phase varies at different rates.

A good introduction to the basics of coherence theory can be found on page 563 of [Hecht, 1998] while the following description is taken largely from [Howard et al., 2003]

and presented for completeness. The intensity of the transmitted or reflected wave at the beam splitter due to a wave with a scalar component  $E(t)$  and a complex (self) coherence  $\tilde{\gamma} = \langle E(t+\tau)E^*(t) \rangle_T / I_0$ , where  $I_0 = \langle E(t)E^*(t) \rangle_T$  is the spectrally integrated irradiance, is given by

$$S_{\pm}(\phi) = \frac{I_0}{2} \{1 \pm \Re[\tilde{\gamma}(\phi)]\} \quad (\text{A.2})$$

as a function of the phase delay  $\phi = 2\pi\nu\tau$ . As the light is only quasi coherent the relationship between  $\phi$  and  $\nu$  is expressed as  $\phi = 2\pi\nu\tau(\nu) \approx \phi_0 + \kappa\phi_0\xi = \phi_0 + \check{\phi}_0\xi$  where we have substituted  $\nu = \nu_0(1+\xi)$  and where  $\xi = (\nu - \nu_0)/\nu_0$  is the normalised frequency difference coordinate and where  $\kappa$  is given by

$$\kappa = 1 + \left. \frac{\nu_0}{\tau_0} \frac{\partial \tau}{\partial \nu} \right|_{\nu_0} \quad (\text{A.3})$$

and accounts for any optical frequency dispersion through the system. Using the Wiener-Khinchine theorem the self coherence can be written as

$$\gamma(\phi) = \frac{1}{I_0} \int_{-\infty}^{\infty} I(\xi) \exp(i\phi\xi) d\xi \quad (\text{A.4})$$

which essentially relates the self coherence of the wave to the Fourier transform of the line-shape  $I(\xi)$ . Given a line with a frequency offset  $\xi_D = \nu_D/\nu_0$  and a line-width of  $\sigma = \Delta\nu/\nu_0$  and a functional line-shape  $g$

$$I(\nu) = I_0 g\left(\frac{\xi - \xi_d}{\sigma}\right) \quad (\text{A.5})$$

and combining equations A.2 and A.4 yields an interferogram given by

$$S = \frac{I_0}{2} [1 + \zeta \cos(\phi_0 + \phi_D)] \quad (\text{A.6})$$

where, for a line-shape  $g$  of even symmetry the envelope  $\zeta \equiv |\gamma|$  which is the fringe visibility (or contrast) and the phase shift ( $\phi_D$ ) are given by

$$\zeta = G(\sigma\check{\phi}_0) \quad (\text{A.7})$$

$$\phi_D = \check{\phi}_0\xi_D \quad (\text{A.8})$$

where  $G$  is the Fourier transform of the line-shape  $g$ . Varying the mirror position (in figure A.1) has the effect of varying  $\phi_0$ , that is, the position at which the interferogram is sampled. The coherence of the interferogram can be determined by sampling  $S$  at a variety of different values of  $\phi_0$  which, in turn allows the line width to be determined.

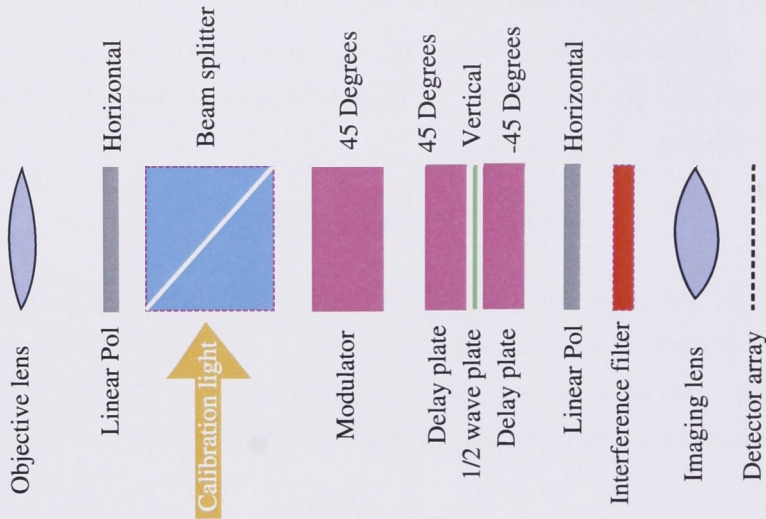


Figure A.2: Optical elements of the coherence imaging camera

One problem with a mechanically modulated Michelson FTS is that, at the high modulation frequencies needed to obtain good time resolution, the motion of the mirror excites vibrations through the system that can lead to tilts and phase offsets. This problem is enhanced due to the small wavelengths being dealt with.

An alternative technique of obtaining a path length difference for self-interference is to use a birefringent crystal. Polarised light entering a birefringent material is split into an ordinary (O) wave polarised parallel to the optic axis and an extraordinary (E) wave polarised perpendicular to the optic axis. The two waves experience a different refractive index denoted  $n_O$  and  $n_E$  (not to be confused with the electron density  $n_e$ ) and the birefringence is the difference  $B = n_E - n_O$ . Radiation with a wavenumber  $k_0 = 2\pi\nu_0/c$  travelling through a birefringent crystal of length  $L$  will emerge at the end of the crystal as an E and O wave with a phase difference of  $\phi_0 = k_0BL$  thus providing a delay offset. Furthermore, by using a crystal that is also electro-optical the birefringence can be modulated (through the application of an electric field) allowing the interferogram (equation A.6) to be sampled in a similar fashion to the scanning of the mirror in figure A.1.

## A.2 Doppler imaging diagnostic

Figure A.2 shows the optical elements of a coherence imaging camera based on the electro-optic effect. This device (known as the modulated optical solid state spectrometer or MOSS) collimates the light using an objective lens. Light is then

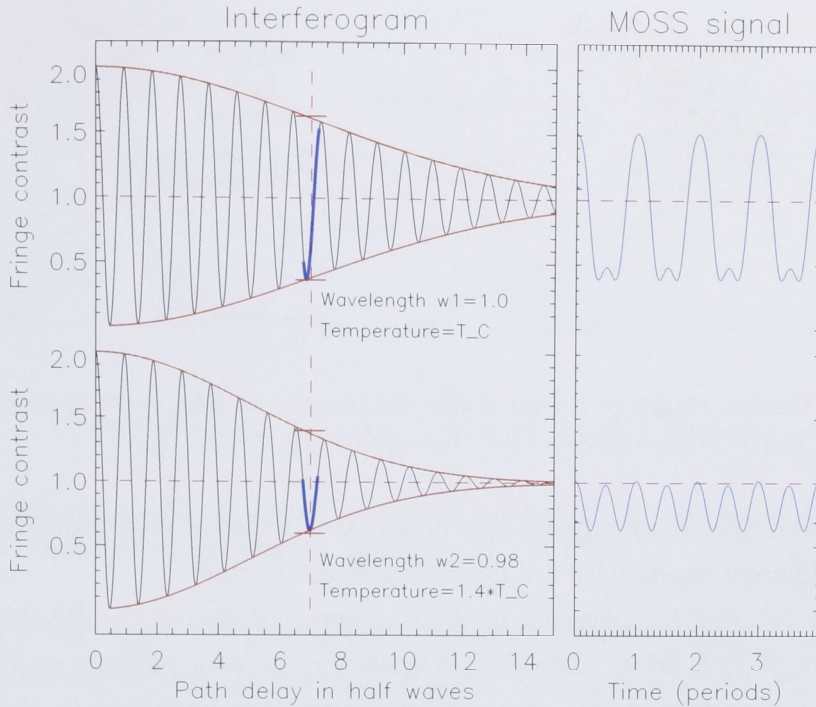


Figure A.3: An illustration how the drive voltage on the electro-optical crystal is used to get a 2nd harmonic carrier by modulating over a fringe in the interferogram (figure courtesy John Howard).

passed through a polariser which polarises the light such that it is at  $45^\circ$  to the optic axis of the modulator (hence giving roughly equal O and E components). The modulator is an electro-optic crystal, in this case lithium niobate ( $\text{LiNbO}_4$ ) which as a sinusoidally varying electric field applied to vary  $B$  and hence  $\phi_0(t)$ . The light then passes through two delay plates which gives a DC offset to  $\phi_0$  which allows the instrument to sample  $S$  in a region which is more sensitive to variations in  $\zeta$ . To reduce path length effects (different angles seeing different path lengths and hence different  $\phi_0$  reducing the instrument contrast) the system uses two delay plates with orthogonal axes with a  $1/2$  wave plate between them. For a discussion of how this works see page 80 of [Michael, 2003]. The E and O components are then combined on an analyser and passed through an interference filter to isolate the transition line of interest. Finally the light is then detected using a 16 channel PMT array (A Hamamatsu R5900U-04-L16).

The drive voltage,  $V(t)$ , for the electro-optic crystal is chosen such that it modulates over the top of a fringe, producing a signal that has a dominant second harmonic component (compared to  $V(t)$ ), this is show illustratively in figure A.3. This means, as the interferogram is shifted due to  $\phi_D$ , which is due to an offset

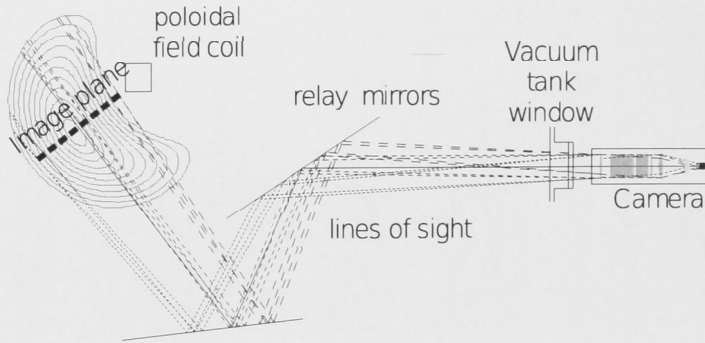


Figure A.4: Viewing chords of the ion coherence imaging camera overlaid on a representation of the H-1NF flux surfaces. Taken from [Michael, 2003]

in the emission line, the modulation is moved to a different region of  $S$  which will produce a different signal with a different harmonic content.

Figure A.4 shows the coherence imaging camera installed at the 315 degree cross section of the H-1NF heliac. The ray paths shown are for a 1400mm objective and an 85mm Nikkor imaging lens, for some measurements presented in the thesis a 105mm imaging lens was used giving a narrower view of the plasma.

Signals are digitised at a harmonic of the modulation frequency and stored in the MDSPlus database for post-shot demodulation. This means that the interferogram is cyclically sampled at given values of  $\phi_0$  allowing averaging over modulation cycles to improve the accuracy of measurements at the cost of temporal resolution.

The coherence camera returns a measure of the brightness weighted line integral ion temperature from which, using techniques discussed in section 2.2, the ion temperature profile can be extracted.

### A.3 Calibration

As shown in figure A.2 the coherence camera uses a beam splitter to allow the input of a calibration light source. By using a laser with a wavelength close to that of the transition of interest (within the interference filter's passband) coupled to a light sphere (thus producing uniform illumination) the instrument contrast can be determined. That is, the contrast degradation caused by effects such as crystal non-uniformities and the variation of crystal path length.

Different spectral lines will behave differently to changing  $T_e$  and  $n_e$ . Therefore, if a contaminant spectral line passed through the interference filter the changing ratio of the contaminant to ion line would present its self as a shift in the centre of mass of the line shape or a change in  $\phi_D$  (and  $\zeta$ ) in equation A.6.

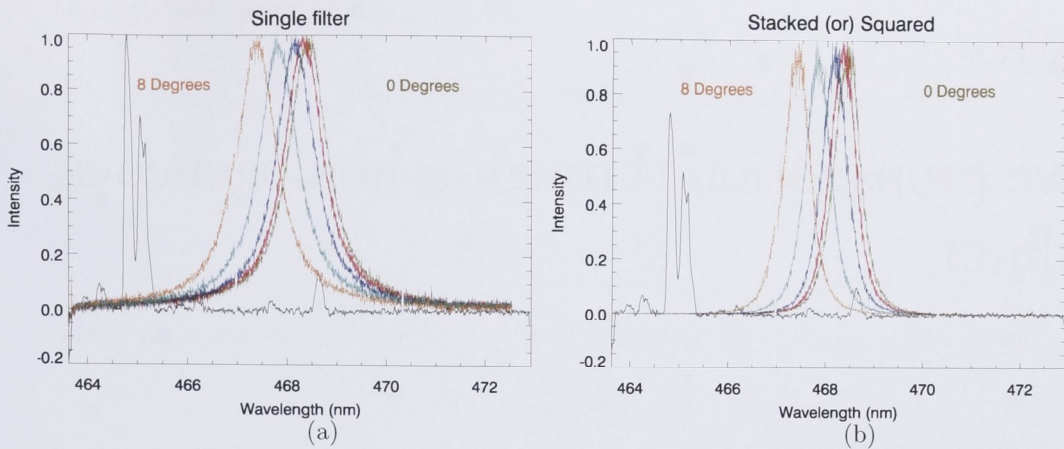


Figure A.5: Passbands for single and stacked (simulated by squaring the single response) 468nm filters overlaid on an emission spectrum.

Figure A.5(a) shows the passband of the 468nm helium ion filter as a function of tilt angle overlaid on a spectrum taken during an ECH initiated and heated plasma. The maximum angle for the 85mm lens imaging onto a 16mm detector array (from equation 3.6) is 5 Degrees. The cluster of lines around 465nm is from CIII and as is evidenced by the plot will be partially transmitted by the filter. To simulate the effect of using a stacked filter pair in figure A.5(b) the passband was squared and re-normalised. As can be seen this significantly reduces the width of the passband, more effectively excluding the impurity lines at the cost of light flux and hence signal-to-noise.

# Wave propagation through a homogeneous medium

Electromagnetic radiation strongly interacts with matter in the plasma state due to the mobility of charge carriers. The refractive index of a plasma is given by the Appleton-Hartree formula which is derived from the dielectric tensor.

$$N^2 = 1 - \frac{X(1 - X)}{1 - X - \frac{1}{2}Y^2 \sin^2\theta \pm [(\frac{1}{2}Y^2 \sin^2\theta)^2 + (1 - X)^2 Y^2 \cos^2\theta]^{\frac{1}{2}}} \quad (\text{B.1})$$

where X and Y are dimensionless quantities given by

$$X = \omega_p^2/\omega^2, \quad Y = \Omega/\omega \quad (\text{B.2})$$

where  $\omega_p$  is the plasma frequency,  $\Omega$  is the electron gyro-frequency and  $\omega$  is the frequency of the propagating electromagnetic radiation. Fortunately, for the case where  $\omega \gg \Omega$  equation B.1 reduces to

$$N^2 = 1 - X = 1 - \omega_p^2/\omega^2 \quad (\text{B.3})$$

When the probe frequency is much greater than the plasma frequency the refractive index is unity and as the probe frequency approaches the plasma frequency refraction becomes stronger until at  $\omega_p = \omega$  where the probe wave becomes evanescent.

As the wave travels through the plasma, along a path  $\ell$ , it undergoes a phase shift  $\phi$  given by

$$\phi = \int_{\ell} k dl = \int_{\ell} N \frac{\omega}{c} dl \quad (\text{B.4})$$

Due to many unknowns in the system (path lengths, phase shifts due to optics)  $\phi$  is a difficult quantity to measure. A more accessible quantity is the difference in phase shift between an beam that travels through the plasma and one that travels

through free space, this is given by

$$\Delta\phi = \int_{\ell} (k_{plasma} - k_0) dl = \int_{\ell} (N - 1) \frac{\omega}{c} dl \quad (\text{B.5})$$

Now equation B.3 can be expressed as

$$N^2 = 1 - \frac{n_e}{n_c} \quad (\text{B.6})$$

where  $n_c$  is the density where the electromagnetic wave becomes evanescent

$$n_c = \omega^2 m \epsilon_0 / e^2 \quad (\text{B.7})$$

For densities less than the cut off density combining eqs B.5 and B.7 yields

$$\Delta\phi = \frac{\omega}{c} \int_{\ell} \left[ \left( 1 - \frac{n_e}{n_c} \right)^{\frac{1}{2}} - 1 \right] dl \quad (\text{B.8})$$

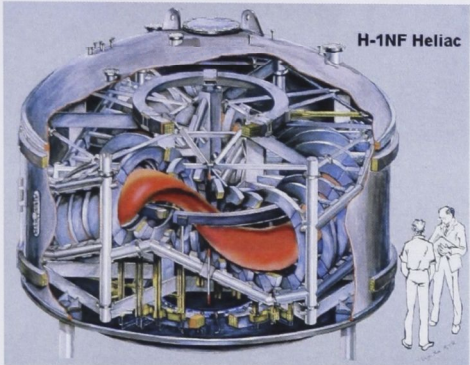
By taking a binomial expansion, for densities much less than the cut of density, equation B.8 reduces to

$$\Delta\phi = \frac{-\omega}{2cn_c} \int_{\ell} n_e dl \quad (\text{B.9})$$

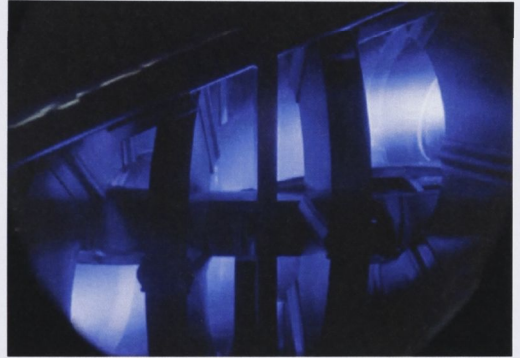
So the phase difference between a probe and an equal length reference arm of an interferometer is directly proportional to the chord averaged electron density.

APPENDIX C

# Photographs of equipment and layouts



A

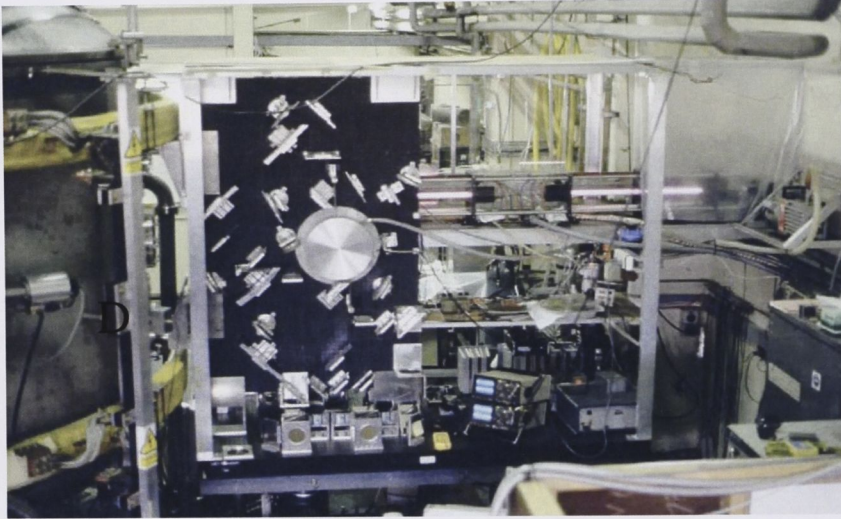


B

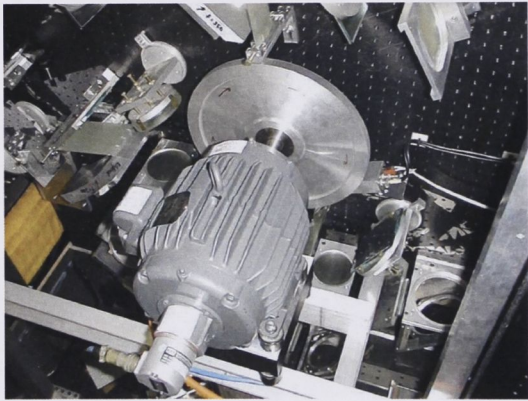


C

Figure C.1: A: Artists impression of the H-1NF device showing the vacuum vessel , coil set and an approximation of the confined plasma. (D.F. Zhou) B: A photograph of an Argon plasma in H-1NF. (ANU Photographics) C: A wide angle shot of the H-1NF experimental cell. (Tim Wetherell)



A



B



C

Figure C.2: A: The scanning FIR interferometer. The pink glow is the CO<sub>2</sub> laser used to pump the formic acid FIR laser. The old air turbine driven wheel is shown (this image predates this project and is from [Warr, 1998]). B: The electric motor and the continuous grating wheel which replaced the air turbine drive. C: The backward wave oscillator which, by scanning the frequency of the emitted radiation, removed the need for a moving grating allowing the whole system to be scanned electronically.

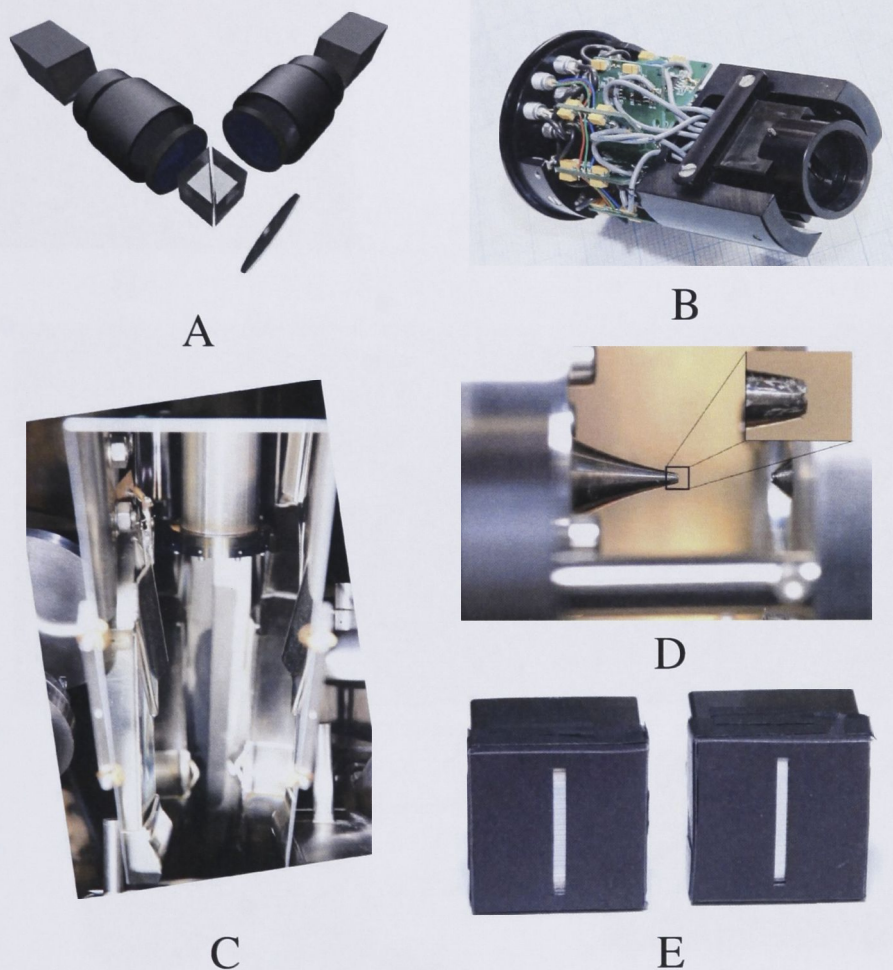


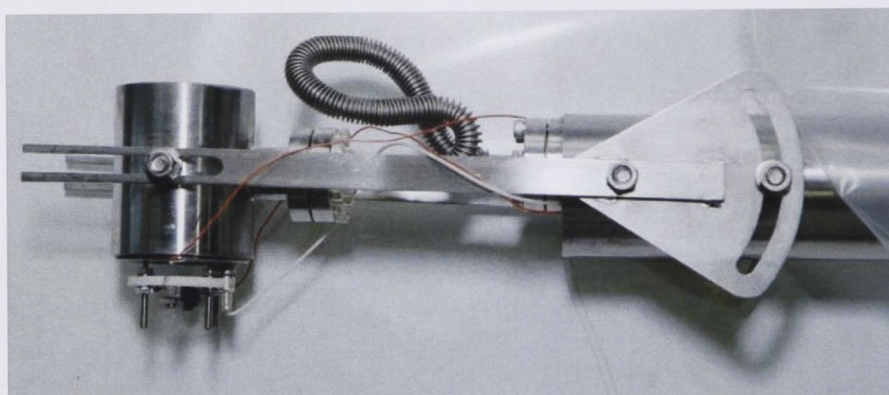
Figure C.3: A: A POVRAY raytrace of the HLR viewing optics showing the objective lens, beam splitter, two filters, two lenses and two PMT arrays. B: The HLR camera, a 16 channel PMT array, 16 transimpedance amplifiers and a slit assembly all in one unit. C: A photograph of through a H-1NF port at the HLR cross section, the end of the HBD can be seen at the top of the image. D: The nozzle (right) skimmer (left) assembly. E: The 16 channel PMT arrays. Note that these were not the slit assemblies used to obtain the data in this thesis which is shown in sub figure B



A



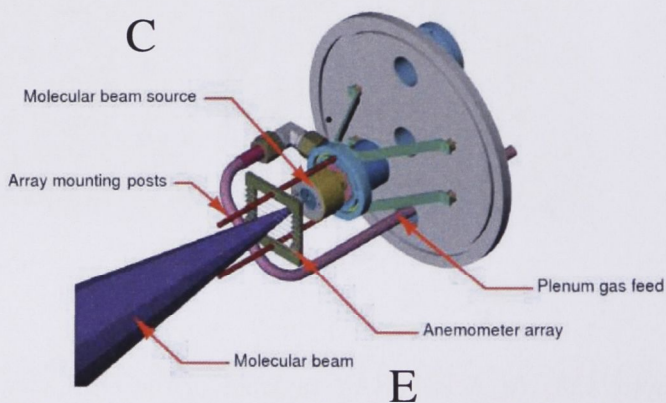
B



C



D



E

Figure C.4: A: Wire holding grid with a single  $10\mu\text{m}$  tungsten wire illuminated using a He-Ne laser. B: Tungsten CTA wires glowing during operation. C: DISH device installed on the end of the re-entrant arm. D: Nozzle insert in valve assembly. E: CAD drawing of DISH system as installed in the test tank. Image courtesy John Wach and Ben Powell.

## Table of acronyms

ANU	Australian National University
BWO	Backwards wave oscillator
CRM	Collisional radiative model
CT	Compact toroid
CTA	Constant temperature anemometry
DISH	Directional injection system for H-1NF
ECE	Electron cyclotron emission
ECH	Electron cyclotron heating
ELSI	Electronically swept interferometer
FIR	Far infra-red
FW	Fast wave
FWHM	Full width at half maximum
HBD	Helium beam diagnostic
HFC	Helical field coil
HLR	Helium line ratio
HWHM	Half width at half maximum
ICH	Ion cyclotron heating
LCFS	Last closed flux surface
MDSPlus	MIT data system plus
NBI	Neutral beam injection
PFC	Poloidal field coil
PMT	Photomultiplier tube
RF	Radio frequency
RMS	Root mean squared
RPM	Revolutions per minute
SMBI	Supersonic molecular beam
SNR	Signal-to-noise ratio
TD CRM	Time dependent collisional radiative model
TFC	Toroidal field coil

## Table of symbols

$n_e$	The electron density
$n_i$	The ion density
$T_e$	The electron temperature
$T_i$	The ion temperature
$P_e$	The electron pressure
$V_p$	Volume of the plasma
$A_p$	Surface area of the plasma
$n_0$	Beam density at the plasma edge OR Refractive index of air
$n_{sf}$	Density of the static fill
$n_{eff}$	Effective refractive index of an interference filter
$\tau_{ec}$	Electron particle confinement time
$\tau_{Ee}$	Electron energy confinement time
$E_{st}$	Stored electron energy
$k$	Wavenumber OR constant of proportionality between photon counts and voltage signal
$\omega_{ci}$	The ion cyclotron angular frequency
$\omega_{ii}$	The ion ion hybrid angular frequency
$\beta$	Angle of diffraction OR constant of proportionality between flux and CTA signal
$\alpha$	Angle of incidence onto a grating
$d$	Groove spacing
$\iota$	Rotational transform
$r, \theta, \Phi$	radial, poloidal and toroidal co-ordinate
$\phi, \Delta\phi$	Phase and phase shift
$n_c$	Cut off density
$\mu^{(n)}$	The $n$ th moment of the phase projection
$P_i$	Phase projection
$\mathbf{P}$	Array of $P_i$
$I(\mathbf{r})$	Object
$f_k$	The $k$ th basis function
$w_k$	The $k$ th weight

$\mathbf{w}$	Array of $w_k$
$R_{kj}$	Line integral along the $j$ th chord of the $k$ th basis function
$\mathbf{R}$	The matrix of $R_{kj}$
$R_k$	The rate density of a transition $k$
$R$	Ratio
$\kappa_h$	Helical ratio
$I_{sec}, I_{main}$	The currents supplied from the main and secondary power supplies
$C(i, j)$	Collisional rate coefficient from a state $i$ to a state $j$
$A(i, j)$	Spontaneous transition rate from a state $i$ to a state $j$
$\alpha(i), \beta(i), \beta_d(i)$	Three body, dielectric and radiative recombination rate coefficients to a state $i$
$S(i)$	Ionisation rate coefficient from a state $i$
$S_{Obj}, S_{Det}$	Size of the object and detector
$f_I, f_O$	focal length of the imaging and objective lenses
$M$	Magnification OR Mach number
$d_s, d_p$	distance between the objective to imaging lenses and distance between the objective lens and object (plasma)
$N_p, N_p^{(sf)}$	Particle injection rate and the particle injection rate due to static fill
$v_{th}$	Average thermal velocity
$\Gamma_{sf}$	Thermal flux across the plasma boundary
$P_e$	Electron pressure
$\beta_e$	Ratio of the electron pressure to the magnetic pressure
$k_c$	Coupling constant between the ECH power and the plasma
$P_{ech}$	Estimated ECH power
$p_\lambda, b_\lambda$	Average pulse and baseline signal at wavelength $\lambda$
$I_\lambda$	Emissivity at wavelength $\lambda$
$SNR$	Signal-to-noise ratio
$t_0$	Time of the beginning of the discharge OR time of the HBD trigger pulse
$t_w$	Width of the HBD averaging window
$t_s$	Difference in time between the HBD trigger pulse and the time of maximum light signal
$S$	Distance along the injection axis
$S(t)$	Time varying signal
$s_a(t)$	The analytic signal

# List of Figures

1.1	CO <sub>2</sub> Levels from the Mauna Loa clean air observatory in the pacific	3
1.2	Co-ordinates used when describing toroidal geometries . . . . .	5
1.3	The Large Helical Device (LHD) in Japan, which uses helical windings to introduce twist, and the Wendelstein 7-X (W7-X) device in Germany which uses warped modular coils (both shown in dark blue). The red helical structure on W7-X device is a divertor plate. . . . .	7
1.4	The H-1NF flexible heliac . . . . .	8
1.5	Magnetic configuration as a function of the helical coil current ratio, $\kappa_h$ . Panels show Poincaré plots of the flux surfaces at $\Phi=0$ degrees. Image courtesy of David Pretty. . . . .	8
1.6	Location of RF (7MHz) antenna . . . . .	10
1.7	A top view of the H-1NF heliac showing the location of major diagnostics . . . . .	11
1.8	A diagram of ITER showing a human as scale. One of the reasons for the massive size of the ITER plasma is to ensure that energetic alpha particles (from the reaction shown in equation 1.2) have enough time to collisionally transfer energy to the bulk plasma. . . . .	12
2.1	Launch geometry for the 2mm Michelson heterodyne density interferometer used to routinely measure the line-averaged electron density in H-1NF. The internal support structure for the scanning interferometers, which is toroidally displaced by one field coil, is also shown.	17
2.2	A Gaussian ray trace of the swept FIR interferometer showing the static optics and the rotating grating wheel at the centre of the device which is used to both provide a frequency shift for heterodyne detection and effect a spatial sweep of the plasma. The figure is effectively a long time exposure, at any one instant in time only a single chord in each of the views is active . . . . .	18

2.3	Sample data (projections) measured during a combined ion/electron resonantly heated discharge. . . . .	19
2.4	Variation with the magnetic configuration (left to right) of the plasma coverage of the top diagonal view (top), projections shown as crosses and the best fit as a solid line (centre), and reconstructions of the density profile (bottom). . . . .	20
2.5	Layout of the electronically scanned interferometer. The blue path is the path taken by the radiation at the high frequency side of the scan while the red path is the path taken at the low frequency side of the scan. (from [Howard & Oliver, 2006]) . . . . .	21
2.6	A Gaussian ray trace of the three view ELSI launch optics and paths in the plasma. The beam width in the centre of the plasma is 2cm (from [Oliver et al., 2006]) . . . . .	22
2.7	Plasma induced phase shift as a function of time and scan position (0=plasma edge 1=plasma centre) measured using ELSI . . . . .	23
2.8	The left panel shows the end of the ECH waveguide with the approximate beam width of the directly launched 28GHz X-mode radiation while the right panel shows a photograph of the double saddle antenna used to launch the 7MHz ICH wave into the plasma. Both images are overlaid with a Poincaré plot for flux surfaces in standard configuration ( $\kappa_H = 0$ ). . . . .	25
2.9	Raw demodulated data from the H-1NF scanning interferometer showing the projection of the electron density profile as a function of the on-axis rotational transform . . . . .	27
2.10	Reconstructed density profile as a function of rotational transform and associated errors in the reconstruction . . . . .	28
2.11	The zeroth moment ( $\mu^{(0)}$ ) of the projection of the density profile, which gives a measure of the average electron density, and the second central moment ( $\mu^{(2)}$ ), which gives a measure of the profile width . . . . .	29
2.12	Poincaré plots of flux surfaces of the standard configuration ( $\iota_{ax} = 1.12$ ) with contour lines where $\omega_{ic} = \omega$ and $\omega_{ii} = \omega$ . . . . .	29
2.13	The top panel shows a line and contour plot of the evolution of the local electron density as well as the approximate heating power applied during discharge 44508. The bottom panel shows profiles, taken through the centre of the plasma, of the rate of rise of the electron density. . . . .	31

3.1	The rate equation for the population (number density) of a state $i$ . . . . .	34
3.2	Energy levels for the neutral helium atom. Principal quantum number is shown on the left. Energy values where the collisional radiative model groups states are shown in white . . . . .	35
3.3	The CRM calculated rate of the 471.3nm ( $4^3S \rightarrow 2^3P$ ) and 504.8nm ( $4^1S \rightarrow 2^1P$ ) transitions as a function of electron temperature and density . . . . .	35
3.4	Ratio of the 504.8nm ( $4^1S \rightarrow 2^1P$ ) transition rate to the 471.3nm ( $4^3S \rightarrow 2^3P$ ) as a function of electron density and temperature . . . . .	36
3.5	Collection optics for the helium line ratio diagnostic. . . . .	37
3.6	An optical diagram for a telescope imaging an object located at the objective focal length. . . . .	37
3.7	Schematic of the 16 channel PMT array . . . . .	38
3.8	Spatial calibration of the HLR optics showing good registration and focus. . . . .	39
3.9	Passbands of the 471.3nm and 504.8nm filters measured using a high resolution spectrometer and a 2048 channel 1D CCD array. The emission wavelengths of the transitions of interest are indicated by a vertical line. . . . .	40
3.10	Angular response of the 471.3nm interference filter . . . . .	41
3.11	transmission through the 504 and 471nm filters as a function of channel number and the ratio of the two transmissions. A direct measurement of the transmission through the 504nm filter is over-plotted (diamonds). . . . .	42
3.12	The spectrum of the light emitted by the calibration lamp (reflected off the white card) as recorded by the SM-232 spectrometer, and corrected for the spectrometer response. The centre wavelengths of the passbands of the filters used have been highlighted. . . . .	42
3.13	Response of the two cameras to uniform illumination, corrected for the spectrum of the source. Even though the same model of detector was used in both the cameras, camera 2 is less sensitive than camera 1. This is because camera 2 is closer to the vertical field coil of the H-1NF device and is strongly affected by the magnetic field (despite attempts to shield it). . . . .	43

3.14	Emission spectra from the H-1NF plasma in the region of the 504.8nm He line showing various impurity lines falling within the interference filter passband . . . . .	44
3.15	A diagram of the HLR $T_e$ diagnostic system showing a Poincaré plot (at standard configuration) of the H-1NF flux surfaces with the viewing geometry of the optical system and launch geometry of the helium beam . . . . .	45
3.16	Light signals for the central channel of the toroidal imaging array during multi-pulse helium beam injection into an ECH heated plasma (discharge 61031). The time series highlights the components of the measured emission due to the prompt (blue), effusive (yellow) and background (red) components of the injection. . . . .	47
3.17	(a) Contour plots of the light collected by the toroidal imaging array as a function of time (relative to the pulse trigger) and position. (b) Profile data with fitted Lorentzians . . . . .	48
3.18	Intensity, spatial and temporal width of the light pulses produced using the HDB as a function of source pressure, pulse length and pulse number . . . . .	49
3.19	(a) Position of the fitted Lorentzian as a function of the angle of the rail. (b) Ratio between the pulse amplitude (minus the background) and the background level. . . . .	50
3.20	Raw light signals collected through the 504nm filter during HBD injection into an ECH heated plasma (discharge 61031). . . . .	52
3.21	An isolated HBD pulse showing the averaging window . . . . .	53
3.22	A flowchart showing the procedure for the extraction of helium emissivities and the calculation of $T_e$ using helium line ratios . . . . .	54
3.23	(a) Extracted emissivity profiles, note the attenuation due to ionisation. (b) The calculated temperature profile. This data is for discharge 61031. . . . .	56
4.1	Time series for H-1NF discharge 61031 showing the evolution of the line-averaged electron density (as measured by the 2mm interferometer), diamagnetic signal and emission as viewed through the 471nm spectral filter. . . . .	59

4.2	Spatially resolved plots of the electron density and temperature for shot 61031. The last panel shows the diamagnetic signal with the volume averaged electron pressure overplotted using an independent axis. It should be noted that although the use of contour plot presents the illusion of continuous data the plot of electron density consists of only 13 sweeps of the ELSI device and the electron temperature plot only consists of 7 profiles. The electron density profile was remapped to the electron temperature timebase to calculate the average $P_e$ in the bottom panel. . . . .	60
4.3	The rate of rise of the plasma electron inventory and the approximate (assuming a torus shaped plasma) particle injection rate from the static fill, ( $N_s$ ) . . . . .	61
4.4	Transformation between cartesian co-ordinates and flux co-ordinates. The image on the left shows flux surfaces calculated using the HELLIAC code and, overlaid in orange, surfaces of constant $r$ calculated by interpolating the Gourdon code output. The image on the right shows the transformation of the points (crosses) in the left hand figure to a co-ordinate system where flux surfaces are circular. . . . .	63
4.5	Profiles of electron temperate at two different magnetic configurations. (a) In cartesian co-ordinates. (b) Mapped onto normalised flux co-ordinates ( $r$ ) . . . . .	63
4.6	$T_e$ profile in flux co-ordinates as a function of helical ratio. There was no data taken between $\kappa_h = 0.0$ and $0.2$ . The radius of high order rational surfaces is overplotted. . . . .	65
4.7	Time evolution of $T_e$ (points) and $T_i$ (curve) as measured by the central channels of the HLR and ion coherence diagnostics. . . . .	67
4.8	Contours of the emissivity of the 471nm transition as a function of time and major radius. The contour lines are the measured emissivities while the filled contours show the emissivity as calculated for the TD CRM.(a) Using a parabolic density profile. (b) Using reconstructions from the ELSI device. . . . .	68
4.9	Measured emissivity profiles (both scaled by a common constant) and the TD-CRM output. . . . .	69
4.10	Raw data from HLR viewing optics for discharge 62274. . . . .	70
4.11	Emissivity and temperature profiles measured using the HLR diagnostic during an ICH plasma. . . . .	71

4.12	Measured emissivity profiles and TD-CRM output for an ICH heated plasma using the (a) original and (b) corrected $T_e$ profiles. . . . .	71
4.13	Measured emissivity profiles and TD-CRM output for an ICH heated plasma using the corrected $T_e$ profile and a $n_e$ profile from a similar shot. . . . .	72
4.14	Corrected $T_e$ profile in cartesian and flux co-ordinates. The density profile is shown in blue in figure (a) and the pressure profile is shown in red in figure (b). . . . .	72
4.15	$T_e$ profile measured late (56ms) in discharge 62247. . . . .	73
5.1	Cross section of the double conical nozzle used to generate the supersonic flow . . . . .	75
5.2	Mach number, pressure and temperature along the nozzle for $P_0=1\text{atm}$ and $T_0=300\text{K}$ . . . . .	77
5.3	Variation of the particle injection rate showing a linear dependence on both plenum pressure ( $P_0$ ) and throat diameter ( $D^*$ ). A typical particle confinement loss rate is over-plotted. . . . .	77
5.4	The valve assembly attached to the closed plenum system. The nozzle insert can be changed with a minor vacuum opening allowing different nozzles to be fitted as needs change. . . . .	78
5.5	The layout of the DISH control systems and test tank. . . . .	80
5.6	The constant temperature hot wire anemometry circuit. The wire (marked probe) is kept at a constant temperature by the injection of current from the +15V source via a transistor when the bridge is out of balance. The system is in balance when the resistance of the probe equals that of the adjustable resistor. Changing the resistance of the adjustable resistor changes the equilibrium temperature of the probe. . . . .	80
5.7	A sample shot showing four channels of anemometry data . . . . .	81
5.8	Measured particle injection rate versus plenum pressure. A line showing a quarter of the theoretical injection rate is over-plotted showing a deficit in the number of particles injected due to the deviation in behaviour from ideal isentropic flow . . . . .	82
5.9	The Half Width at Half Maximum of the fitted Lorentzian to the scaled data as a function of plenum pressure. Typical error bars are shown. . . . .	83

5.10	The observed half width at half maximum angle of the beam showing a linear dependence on the plenum pressure between 300 and 1000 torr. Typical error bars are shown. . . . .	84
5.11	The phase difference between the modulation on the valve drive voltage and the observed modulation on the anemometer signals as a function of distance from the nozzle . . . . .	85
5.12	Experimentally determined average density of beam particles as a function of distance from the nozzle and plenum pressure. Lines are plotted in 100 torr increments. . . . .	86
5.13	Mean free path of mono-energetic electrons for ionising collisions in the helium beam for a variety of electron energies . . . . .	87
5.14	Mean free path ( $\lambda_b$ ) for supersonic helium neutral particles travelling at a velocity of 690m/s through a plasma slab of density $1 \times 10^{18}m^{-3}$	87
5.15	The re-entrant arm used to mount the injection system in the H-1NF vessel. The mount includes a optical view port where diagnostics get a clear view of where the supersonic beam intersects the plasma . .	88
5.16	Traces of the heating power, electron density and helium light emission from a resonantly heated plasma in the H-1NF vessel at 0.5 Tesla	89
5.17	Raw light images, corrected for vignetting, taken through the optical view port as the injection was initiated. . . . .	90
5.18	The variation of the width of the observed intensity increase versus the plenum pressure in the injection system . . . . .	90
5.19	Density of all neutral states of helium (contour intervals in $m^{-3}$ ) calculated using the TD CRM as a function of $T_e$ and distance into the slab at a constant density of $n_e = 1 \times 10^{18}m^{-3}$ . . . . .	92
5.20	Decay length, $l_d$ , of the combined populations of neutral helium as a function of slab electron temperature ( $n_e = 1 \times 10^{18}m^{-3}$ ) compared with mean free paths calculated using equation 5.10 . . . . .	92
5.21	Densities of the helium metastable states $2^1S$ and $2^3S$ as a function of distance into the slab for an injection density of $n_0 = 1 \times 10^{20}m^{-3}$ .	93
5.22	The $T_e$ profile with a Gaussian fit and interpolated $n_e$ profile that will be used in the modelling of the DISH fuelling profile using the TD CRM . . . . .	94
5.23	Modelled injection geometry showing the $T_e$ profiles used as an input to the TD CRM code as well as contours (white) at regularly spaced normalised flux co-ordinate . . . . .	95

5.24	Particle deposition profile along the DISH injection axis calculated using a TD CRM. . . . .	96
5.25	Deposition of ions from the DISH beam calculated using a TD CRM. The peak in the profile moves outwards with increasing temperature as the fuelling moves from the core to the edge. . . . .	96
5.26	(a)The transparency, $P$ , of the plasma to the DISH beam as a function of average electron temperature across the DISH injection axis. (b)The position of the peak in injection rate, $N_{dep}$ , relative to the peak in $T_e$ (which is on the magnetic axis). . . . .	97
5.27	The stored electron energy ( $E_{se}$ ), the energy lost by electron impact excitation through radiation ( $E_{rad}$ ) and ionisation ( $E_{iz}$ ) as a function of average electron temperature for beam conditions characteristic of a DISH pulse of 5ms at 500 torr. . . . .	99
6.1	Density of the metastable $2^1S$ state of atomic helium as a function of major radius and time for shot 61031 . . . . .	103
6.2	Proposed modification of the HLR system to enable the measurement of E-Fields using LIF . . . . .	104
A.1	Optical layout for a Michelson FTS. . . . .	106
A.2	Optical elements of the coherence imaging camera . . . . .	108
A.3	An illustration how the drive voltage on the electro-optical crystal is used to get a 2nd harmonic carrier by modulating over a fringe in the interferogram (figure courtesy John Howard). . . . .	109
A.4	Viewing chords of the ion coherence imaging camera overlaid on a representation of the H-1NF flux surfaces. Taken from [Michael, 2003]	110
A.5	Passbands for single and stacked (simulated by squaring the single response) 468nm filters overlaid on an emission spectrum. . . . .	111
C.1	A: Artists impression of the H-1NF device showing the vacuum vessel, coil set and an approximation of the confined plasma. (D.F. Zhou) B: A photograph of an Argon plasma in H-1NF. (ANU Photographics) C: A wide angle shot of the H-1NF experimental cell. (Tim Wetherell) . . . . .	115

- C.2 A: The scanning FIR interferometer. The pink glow is the CO<sub>2</sub> laser used to pump the formic acid FIR laser. The old air turbine driven wheel is shown (this image predates this project and is from [Warr, 1998]). B: The electric motor and the continuous grating wheel which replaced the air turbine drive. C: The backward wave oscillator which, by scanning the frequency of the emitted radiation, removed the need for a moving grating allowing the whole system to be scanned electronically. . . . . 116
- C.3 A: A POVRAY raytrace of the HLR viewing optics showing the objective lens, beam splitter, two filters, two lenses and two PMT arrays. B: The HLR camera, a 16 channel PMT array, 16 transimpedance amplifiers and a slit assembly all in one unit. C: A photograph of through a H-1NF port at the HLR cross section, the end of the HBD can be seen at the top of the image. D: The nozzle (right) skimmer (left) assembly. E: The 16 channel PMT arrays. Note that these were not the slit assemblies used to obtain the data in this thesis which is shown in sub figure B . . . . . 117
- C.4 A: Wire holding grid with a single 10 $\mu$ m tungsten wire illuminated using a He-Ne laser. B: Tungsten CTA wires glowing during operation. C: DISH device installed on the end of the re entrant arm. D: Nozzle insert in valve assembly. E: CAD drawing of DISH system as installed in the test tank. Image courtesy John Wach and Ben Powell. 118

# Bibliography

- [Anderson, 1990] Anderson, Ed. (1990). *Modern Compressible Flow, with historical perspective*. Mc Graw-Hill series in Aeronautical and Aerospace Engineering. Mc Graw-Hill.
- [Andruczyk, 2005] Andruczyk, D. (2005). *Development of a supersonic helium beam for plasma diagnostics*. PhD thesis, University of Sydney.
- [Becoulet, 1996] Becoulet, A. (1996). Heating and current drive regimes in the ion cyclotron range of frequencies. *Plasma Phys. Control. Fusion*, 38, A1–11.
- [Beijerinck & Verster, 1981] Beijerinck, H. C. W. & Verster, N. F. (1981). Absolute intensities and perpendicular temperatures of supersonic beams of polyatomic gasses. *Physica A*, 111C, 327–52.
- [Blackwell et al., 2002] Blackwell, B. D., Harris, J., Howard, J., Shats, M., Charles, C., Collis, S., Gardner, H., Glass, F., Hua, X., Michael, C., Pretty, D., Punzmann, H., Solomon, W., & Borg, G. (2002). Overview of the H-1 national facility. In *Proceedings of the 13th International Stellarator Workshop*.
- [Blackwell et al., 2001] Blackwell, B. D., McMillan, B. F., Searle, A. C., & Gardner, H. J. (2001). Algorithms for real time magnetic field tracing and optimization. *Computer Physics Communications*, 142, 243–247.
- [Bornatici et al., 1983] Bornatici, M., Cano, R., Barbieri, O. D., & Engelmann, F. (1983). Electron cyclotron emission and absorption in fusion plasmas. *Nucl. Fusion*, 23(9), 1153–1258.
- [Carraro et al., 2000] Carraro, L., Pol, G. D., Puiatti, M. E., Sattin, F., Scarin, P., & Consorzio, M. V. (2000). Edge temperature and density measurements with a thermal helium beam in the rfx reversed field pinch. *Plasma Phys. Control. Fusion*, 42, 114.

- [Charles et al., 2003] Charles, C., Boswell, R. W., & Lieberman, M. A. (2003). Energy balance in a low pressure capacitive discharge driven by a double-saddle antenna. *Physics of Plasmas*, 10(3), 891–99.
- [D. Andruczyk et al., 2006] D. Andruczyk, S. N., James, B. W., Takiyama, K., & Oda., T. (2006). A short-pulsed, compact supersonic helium beam source for plasma diagnostics. *Plasma Devices & Operation.*, 14(1), 8109.
- [Diez-Rojo et al., 1997] Diez-Rojo, T., Herrero, V. J., & Tafalla, D. (1997). Pulsed supersonic helium beams for plasma edge diagnostics. *Rev. sci. instrum.*, 3(68), 1423–8.
- [Feist, 2003] Feist, J. H. (2003). Status of wendelstein 7-x construction. In *Proceedings of the 14th International Stellarator Workshop*: Max-Planck-Institut fuer Plasmaphysik.
- [Fowler et al., 1964] Fowler, R. G., Holzberlein, T. M., Jacobson, C. H., & Corrigan, S. J. B. (1964). Direct measurements of the lifetime of excited states of neutral helium. *Proc. Phys. Soc.*, 84, 539–44.
- [Fujimoto, 1979] Fujimoto, T. (1979). Collisional-radiative model for neutral helium in plasma. *Journal of quan. spec. rad. transfer*, 21, 439–45.
- [Gardner & Blackwell, 1992] Gardner, H. & Blackwell, D. (1992). Calculation of mercier stability limits of toroidal heliacs. *Nuclear Fusion*, 32(11), 2009–2019.
- [Goniche et al., 2003] Goniche, M., Bremond, S., & Colas, L. (2003). Global analysis of ICRF wave coupling on tore supra. *Nucl. Fusion*, 43, 92–106.
- [Goto, 2003] Goto, M. (2003). Collisional-radiative model for neutral helium in plasma revisited. *Journal of quan. spec. rad. transfer*, 76, 331–44.
- [Gourdon et al., 1971] Gourdon, C., Marty, D., Mashke, E., & Touche, J. (1971). *Nucl. Fusion*, 11, 161.
- [Gross & Melissinos, 1975] Gross, D. & Melissinos, A. (1975). Production of a high density hydrogen gas jet. *Nucl. Instr. and Meth.*, 130, 1–13.
- [Hamamatsu, 1999] Hamamatsu (1999). Hamamatsu framing streak camera. <http://www.ortodoxism.ro/datasheets/hamamatsu/C4187.pdf>.

- [Hamberger et al., 1990] Hamberger, S., Blackwell, B., Sharp, L., & Shenton, D. (1990). *Fusion Technology*, 17, 123–130.
- [Harris et al., 1985] Harris, J. H., Cantrell, J. L., Hender, T. C., Carreras, B. A., & Morris, R. N. (1985). A flexible heliac configuration. *Nucl. Fus.*, 25(5), 623–29.
- [Hecht, 1998] Hecht, E. (1998). *Optics*. Addison-Wesley.
- [Hindmarsh, 2006] Hindmarsh, A. (2006). Serial fortran solvers for ODE initial value problems. Website. <http://www.llnl.gov/CASC/odepack/>.
- [Howard, 1990] Howard, J. (1990). Novel scanning interferometer for two-dimensional plasma density measurements. *Rev. Sci. Instrum.*, 61(3), 1086–1094.
- [Howard et al., 2003] Howard, J., Michael, C., Glass, F., & Danielsson, A. (2003). Time-resolved two-dimensional plasma spectroscopy using coherence-imaging techniques. *Plasma Phys. Contr. Fus.*, (45), 1143–66.
- [Howard & Oliver, 2006] Howard, J. & Oliver, D. (2006). Electronically swept millimetre-wave interferometer for spatially resolved measurement of plasma electron density. *Accepted Journal Appl. Optics*.
- [Hutchinson, 1987] Hutchinson, I. H. (1987). *Principles of plasma diagnostics*. Cambridge university press.
- [J.A.Stillerman, 1997] J.A.Stillerman, e. a. (1997). Mdsplus data acquisition system. *Review of Scientific Instruments*, 68(1), 939–42.
- [Kim & Rudd, 1994] Kim, Y.-K. & Rudd, M. (1994). Binary-encounter-dipole model for electron-impact ionization. *Phys. Rev. A*, 50, 3954–3967.
- [Liu et al., 2006] Liu, D., Xiao, C., Singh, A., & Hirose, A. (2006). Bench test and preliminary results of vertical compact torus injection experiments on the STOR-M tokamak. *Nucl. Fusion*, (46), 104–9.
- [Michael, 2003] Michael, C. A. (2003). *Doppler spectroscopy of argon plasmas in H-1NF using a coherence imaging camera*. PhD thesis, Australian National University.
- [Michael & Howard, 2004] Michael, C. A. & Howard, J. (2004). need to fill in. *Rev. Sci. Instrum.*, (pp. 4008–17).

- [Milora, 1982] Milora, S. (1982). Fuelling of magnetic confinement devices. *J. Vac. Sci. Technol.*, 20(4), 1246–53.
- [Motojima et al., 1999] Motojima, O., Yamada, H., Komori, A., Ohyabu, N., Kawahata, K., Kaneko, O., Masuzaki, S., Ejiri, A., Emoto, M., Funaba, H., Goto, M., Ida, K., Idei, H., Inagaki, S., Inoue, N., Kado, S., Kubo, S., Kumazawa, R., Minami, T., Miyazawa, J., Morisaki, T., Morita, S., Murakami, S., Muto, S., Mutoh, T., Nagayama, Y., Nakamura, Y., Nakanishi, H., Narihara, K., Nishimura, K., Noda, N., Kobuchi, T., Ohdachi, S., Oka, Y., Osakabe, M., Ozaki, T., Peterson, B. J., Sagara, A., Sakakibara, S., Sakamoto, R., Sasao, H., Sasao, M., Sato, K., Sato, M., Seki, T., Shimozuma, T., Shoji, M., Suzuki, H., Takeiri, Y., Tanaka, K., Toi, K., Tokuzawa, T., Tsumori, K., Tsuzuki, K., Yamada, I., Yamaguchi, S., Yokoyama, M., Watanabe, K. Y., Watari, T., Hamada, Y., Matsuoka, K., Murai, K., Ohkubo, K., Ohtake, I., Okamoto, M., Satoh, S., Satow, T., Sudo, S., Tanahashi, S., Yamazaki, K., Fujiwara, M., & Iiyoshi, A. (1999). Initial physics achievements of large helical device experiments. *Physics of Plasmas*, 6(5), 1843–50.
- [Nagasaki et al., 2001] Nagasaki, K., Shats, M. G., Smith, H., & Punzmann, H. (2001). Power absorption calculation for electron cyclotron resonance heating in the h-1 heliac. *Journal of the Phys. Soc. of Japan*, 70(3), 617–20.
- [NOAA, 2006] NOAA (2006). <http://www.mlo.noaa.gov/>. Website.
- [Oliver et al., 2006] Oliver, D., Howard, J., Kumar, T., Pretty, D., & Blackwell, B. (2006). Three view electronically scanned interferometer for plasma electron density measurements in the H-1 heliac. *Rev. Sci. Instrum.*, 77(1).
- [Park, 1988] Park, P. (1988). Refueling tokamaks by injection of compact toroids. *Phys. Rev. Letters*, 61(12), 1364–8.
- [Powell, 2006] Powell, B. (2006). Constant temperature hot wire anemometry applied to the characterisation of a nozzle molecular beam source. Master's thesis, Australian National University.
- [Punzmann, 2000] Punzmann, H. (2000). High power microwave transmission and launching system for ECR heating on H – 1NF. In *Proceedings of the 13th International Stellarator Workshop*: Plasma Research Laboratory, Australian National University.

- [Punzmann & Shats, 2004] Punzmann, H. & Shats, M. G. (2004). Formation and structure of transport barriers during confinement transitions in toroidal plasma. *Physical Review Letters*, 93(12), 125003.
- [Sasaki et al., 1996] Sasaki, S., Takamura, S., Watanabe, S., Masuzaki, S., Kato, T., & Kadota, K. (1996). Helium I line intensity ratios in a plasma for the diagnostics of fusion edge plasmas. *Review of Scientific Instruments*, 67(10), 3521–3529.
- [Shats et al., 1996] Shats, M. G., Rudakov, D. L., Blackwell, B. D., Borg, G. G., Dewar, R. L., Hamberger, S. M., Howard, J., & Sharp, L. E. (1996). Improved particle confinement mode in the H-1 heliac plasma. *Phys. Rev. Letters*.
- [Song et al., 2000] Song, X., Sugie, T., & Yoshino, R. (2000). A simple model of supersonic molecular beam injection. *Journal of Plasma and Fusion Research (Japan)*, (pp. 282–7).
- [Soukhanovskii et al., 2004] Soukhanovskii, V. A., Kugel, H. W., Kaita, R., Majeski, R., & Roquemore, A. L. (2004). Supersonic gas injector for fueling and diagnostic applications on the national spherical torus experiment. *Rev. Sci. Instrum.*, 75, 4320–3.
- [Spitzer, 1958] Spitzer, L. (1958). The stellarator concept. *Jr. Phys. Fluids*, 1, 253.
- [Stix, 1992] Stix, T. H. (1992). *Waves in plasmas*. American Institute of Physics.
- [Takiyama et al., 1993] Takiyama, K., Sakai, H., Yamasaki, M., Oda, T., & Kawasaki, K. (1993). Polarized forbidden-excitations by laser and electric field measurements in plasmas. In *Proc. 6th international symposium on laser-aided plasma diagnostics* (pp. 43–8).
- [Van Dyck et al., 1971] Van Dyck, R. S., Johnson, C. E., & Shugart, H. A. (1971). Radiative lifetime of the  $2^1s_0$  metastable state of helium. *Phys. Rev. A*, 4(4), 1327–1336.
- [Warr & Howard, 2001] Warr, G. & Howard, J. (2001). A three-dimensional gaussian-beam ray-tracing program for designing interferometer/polarimeter plasma diagnostics. *Rev. Sci. Instrum*, 72(5), 2305–9.
- [Warr, 1998] Warr, G. B. (1998). *A multi-view interferometer for electron density tomography on the H-1NF heliac*. PhD thesis, Australian National University.

- [Xian-Ping et al., 2003] Xian-Ping, F., Andruczyk, D., James, B., Takiyama, K., Namba, S., & Oda, T. (2003). Effects of discharge current and voltage on the high density of metastable helium atoms. *Chinese Physics*, 12(5), 495–501.
- [Yao et al., 1998] Yao, L., Tang, N., Cui, Z., Xu, D., Deng, Z., Ding, X., Luo, J., Dong, J., Guo, G., Yang, S., Cui, C., Xiao, Z., Liu, D., Chen, X., Yan, L., Yan, D., Wang, E., & Deng, X. (1998). Plasma behaviour with mbi in hl-1m. *Nuclear Fusion*, 38(4), 631–8.